CZECH TECHNICAL UNIVERSITY IN PRAGUE
FACULTY OF MECHANICAL ENGINEERING

DOCTORAL THESIS

PRAGUE 2021

Jindřich HÁLA

CZECH TECHNICAL UNIVERSITY IN PRAGUE

Faculty of Mechanical Engineering

Department of Fluid Dynamics and Thermodynamics

Compressible Fluid Flow through Narrow Channels

Doctoral Thesis

Study Programme: Mechanical Engineering
Study Field: Thermomechanics and Fluid Mechanics

Supervisor: Prof. Ing. Pavel Šafařík, CSc.
Advisor: Doc. Ing. Martin Luxa, Ph.D.

Ing. Jindřich Hála

Prague 2021

Abstract

Title: Compressible Fluid Flow through Narrow Channels

The turbulence transition in pipe and channel flow represents up to now an important topic, since it is the nature of the flow, which substantially affects the friction and associated losses. With increasing miniaturization and more detailed numerical simulations of the various small flow parts of the turbomachines, the need for experimental data to explore the narrow channel flow phenomena and to validate numerical codes is still there.

This thesis presents the results of the project which aimed to experimentally and numerically explore the compressible viscous flow in narrow channels of the rectangular cross-section of the high aspect ratio. Main objectives of this work were to explore the nature of the flow in such channels using a number of experimental methods including hot-film probe, explore the influence of two types of surface roughness and discuss the effects associated with the phenomenon of aerodynamic choking due to friction. Apart from the narrow channel measurements, the thesis contains also the detailed description of the calibration process of the hot-film probe and accompanying numerical study.

It was observed that despite the channel length to channel height ratio ranging from 50 to 200, the flow was mostly transitional except the flow in the smallest channel of the height $h = 0.5\,\mathrm{mm}$. The effects of the surface roughness were explored using both qualitative and quantitative measurements by means of hot-film probe. The later provided distribution of the wall shear stress at five locations along the channel for two chosen regimes. Further, the analysis revealed inapplicability of the one-dimensional theory for the estimation of the friction factor. The theoretical analysis of the flow choking supported by numerical simulations shows that due to frictional losses, the actual choking is shifted towards the lower back pressure ratios. These findings were summarized in charts, which comprehensively illustrate derived relations.

Keywords

narrow channel flow, minichannel, compressible flow, wall shear stress, hot-film anemometry

Anotace

Název: Proudění vazké stlačitelné tekutiny úzkými kanály

Přechod do turbulence v trubkách a kanálech nekruhových průřezů stále představuje aktuální problém dynamiky tekutin, jelikož je to právě režim proudění, který zásadně ovlivňuje tření a s ním spojené ztráty. S pokračující miniaturizací a stále detailnějšími numerickými simulacemi i malých průtočných částí turbostrojů vyvstává potřeba prozkoumat jevy, ke kterým dochází při proudění v takto úzkých kanálech a získat data, na jejichž základě by bylo možné validovat numerické modely.

Tato práce představuje výsledky doktorandského projektu, který měl za cíl pomocí experimentů a numerické simulace prozkoumat proudění vazké stlačitelné tekutiny úzkými kanály obdélníkového průřezu s vysokým poměrem šířky a výšky. Mezi hlavní cíle patřilo prozkoumání režimu proudění pomocí různých metod včetně použití sondy se žhaveným filmem, dále prozkoumání vlivu dvou typů drsností stěn kanálku a objasnění některých jevů spojených s aerodynamickým ucpáním vlivem tření. Kromě samotného popisu a rozborů experimentu práce obsahuje také detailní popis kalibrace sondy se žhaveným filmem a doprovodných numerických výpočtů.

Bylo pozorováno, že i při značném poměru délky a výšky kanálku, který se pohyboval v rozmezí 50 až 200, bylo proudění ve většině měřených režimů, kromě případu s výškou kanálku $h = 0.5\,\mathrm{mm}$, přechodové. Efekt různě drsných stěn byl zkoumán pomocí kvalitativních i kvantitativních měření pomocí sondy se žhaveným filmem, přičemž kvantitativní měření poskytlo data o smykovém tření v pěti bodech podél kanálku pro dva vybrané režimy proudění. Další analýzy prokázaly, že ve zkoumaných kanálech není možné použít jednorozměrný model proudění pro věrohodné určení smykového tření. Teoretické rozbory a numerické simulace ukázaly, že k aerodynmickému ucpání dochází vlivem ztrát při nižším protitlaku, než odpovídá ideálnímu případu. Výsledky těchto rozborů a z nich odvozených vztahů jsou přehledně zobrazeny do grafů.

Klíčová slova

úzké kanály, minikanál, stlačitelné proudění, smykové napětí, žhavený film

DECLARATION

I declare that I accomplished my doctoral thesis by myself and I named all the sources I used in accordance with the guideline about the ethical rules during preparation of University final theses.

In Prague (date) .....

.....

Author's signature

ACKNOWLEDGEMENT

I wish to acknowledge and thank Prof. Ing. Pavel Šafařík, CSc. and Doc. Ing. Martin Luxa, Ph.D., my thesis supervisors, for their guidance and encouragement during the whole PhD study. I would also like to extend my thanks to the colleagues of the Department of Fluid Dynamics of the Institute of Thermomechanics AS CR, v.v.i. and especially those of the technical staff of Nový Knín laboratory for their support during the designing of the experiments and for their help with the measurements.

Finally, I wish to thank my family and whom I adore and cherish the most, Anna, Štěpán and Adam.

Table of Contents

1 Introduction

Due to its engineering importance, the flow in pipes and channels or ducts has been studied since the dawn of the modern aerodynamics in the 18th century. The milestone works of Daniel Bernoulli were later extended by the research of Osborne Reynolds, [1] probably the first one in the late 19th century to observe the transition to turbulence in pipe. Reynolds introduced the dimensionless parameter expressing the ratio of inertial forces to viscous forces which seems to govern whether the flow is *direct* or *sinuous* as he termed laminar and turbulent flow respectively. This parameter was later named after him and is now known as Reynolds number Re, which is defined as

$$Re = \frac{uD}{\nu}, \tag{1}$$

where u is the flow mean velocity, D the characteristic dimension and ν the kinematic viscosity. Further, at the beginning of the 20th century, the research of Hermann Schlichting, Johann Nikuradse, Cyril Frank Colebrook with Cedric Masey White, Henry Darcy and Julius Weisbach and others on the friction the flow exerts on the channel walls provided experimental data and number of empirical rules. In 1944 Lewis Ferry Moody put available experimental data to one single diagram forming the well known *Moody Chart* which relates the Darcy friction factor to Reynolds number for various relative roughness. The Moody chart and all empirical rules upon which it is based are still widely used in engineering practice. However, these empirical rules proved to be barely applicable to many common engineering applications which, therefore, require special treatment. Some of the limitations of the mentioned empirical rules are described in following paragraphs.

The first problem is that most of the experimental data, from which the empirical rules were derived, were obtained for incompressible fluid flow and thus its applicability for compressible fluid flow, common in turbomachinery, is questionable.

The second problem arises from the geometry. Since most of the studies focused on pipes of circular cross-section, the similarity between circular and non-circular pipes is usually addressed by the use of *equivalent* or *hydraulic diameter*. Yet, this method might, particularly in the case of non-circular cross-section, introduce significant error due to secondary flows [2].

Another problem in the study of friction in pipes, tubes, and channels is that most of the common engineering calculation procedures assume that the flow is fully developed. This assumption is reasonable if the pipes are sufficiently long. However, for shorter channels it became an issue because it is difficult to determine the necessary length of the channel from the entrance to the location where the flow becomes

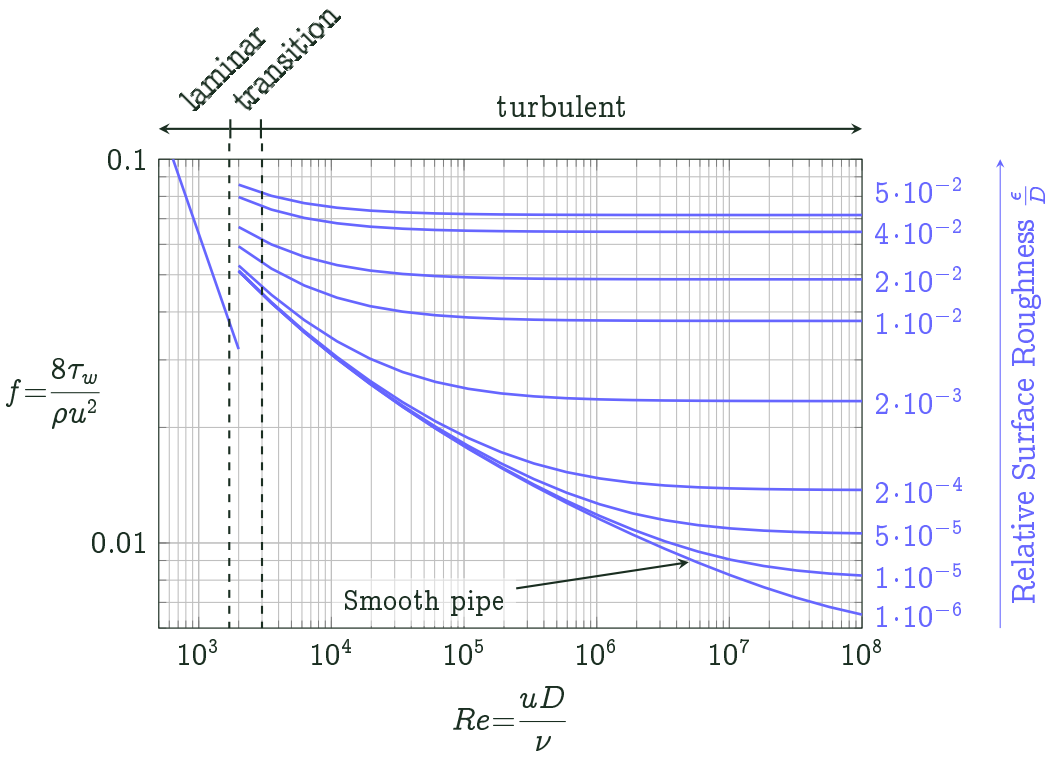

Figure 1: *Moody Chart*

fully developed. This length is referred to as *entrance length* and its values are usually presented in terms of multiples of hydraulic diameter or other characteristic dimension of the channel. This length also significantly depends on whether the flow is laminar or turbulent. The broadly accepted critical value of the Reynolds number for circular pipe flow is $Re \approx 2\,000$. Below this critical value the viscous forces dominate and should effectively dampen any flow perturbations. However, the upper limit of laminar flow existence, above which the turbulent flow would be sustained, is uncertain [3]. There have been experiments in which the laminar flow was established even for $Re = 12\,000$. Generally, the entrance length L_e ranges from dozens to hundreds of the hydraulic diameter D_h. Since there is no clear boundary between the laminar and turbulent mode, and due to ambiguity given by the uncertainty of determination of characteristic dimension, it is evident that such estimates are approximate and might well be affected by the turbulence intensity of the inlet flow and the shape of the channel inlet.

The last problematic factor which will be addressed in this work is surface roughness. From the Moody Chart shown in Figure 1, we can see that its influence is apparent only when the flow is turbulent. In laminar flow the friction factor f is inversely proportional to Re. For turbulent flow, the friction depends on surface roughness and with increasing Re asymptotically approaches constant value for given relative roughness. The constant asymptotic value of the friction factor then

increases with increasing relative roughness [4]. Recent research shows that in the case of small channels, the effects of roughness might be different from those in normal sized channels and the friction might cause unexpected flow behaviour such as the shift of critical conditions. From the engineering point of view, the surface roughness posses another challenge. Since surface finishing, grinding and polishing are expensive operations, which manufacturers would like to avoid if possible, almost no surface in the real world is aerodynamically smooth. For that reason, the surface roughness in aerodynamics is usually expressed as *equivalent sand grain roughness*. This method was introduced for historical reasons since Nikuradse used sand grains of certain average diameter to roughen the inner surface of the pipes he used in his experiments. However, to adequately describe surface roughness, the modern production industry uses more sophisticated methods since one parameter proved to be insufficient to properly characterize all aspects of different surface quality. Therefore, parameters such as arithmetic average roughness Ra, average maximum height of profile Rz, waviness, and many others are used and its conversion to sand grain roughness still poses a problem.

As apparent from the preceding paragraphs, the flow in pipes and channels is still a topical problem of fluid dynamics. This thesis aims to experimentally and numerically examine the flow of a compressible fluid in a simple geometry of two parallel plates forming a narrow channel of the constant, rectangular cross-section, with the characteristic dimension in the order of millimetres. Knowledge and better understanding of phenomena occurring in such flow is necessary for better prediction of the flows in screw-type compressors, control valves and labyrinth seals of steam turbines or in a gap between an impeller and a case in radial turbines and compressors.

2 Literature Review

Most of the contemporary studies related to channel and pipe flow are devoted either to study of the physical mechanism of the transition to turbulence or to the flow in heat exchangers. In the first case, the research is usually concentrated on the flow of incompressible fluid in aerodynamically smooth pipes. The fluid velocities are rather low to obtain $Re \approx 2\,000$ and also to enable the usage of sensitive techniques of flow visualisation and measurements. The aim is usually to study the flow stability, critical conditions influencing the transition from laminar flow to turbulent and phenomenon of relaminarization [5][3]. In the second case of heat exchangers, the research mostly focuses on the increase of its efficiency [6]. In recent decades, a focus is also on microfluidics and nanofluidics, which deal with channels with the characteristic dimensions in the order of micrometres and nanometres respectively. However, these flows are beyond classical continuum fluid dynamics and, therefore, out of the scope of the present thesis.

The flow in narrow pipes and channels can be classified by the characteristic dimension of the channel, which is usually the minimal perpendicular distance of the walls as follows [7].

$L \leq 1\,\mu\text{m}$	Nanochannels
$1\,\mu\text{m} < L \leq 200\,\mu\text{m}$	Microchannels
$200\,\mu\text{m} < L \leq 3\,\text{mm}$	Minichannels
$3\,\text{mm} < L$	Conventional channels

However, this classification is rather vague and varies greatly by author. Another point of view is the classification according to the Knudsen number which measures the degree of rarefaction and is defined as

$$Kn = \frac{\lambda}{D}, \tag{2}$$

where λ is the molecular mean free path and D is the characteristic dimension. Then for $Kn < 1 \cdot 10^{-3}$, the flow can be classified as continuous and modelled by the Navier-Stokes equations with a non-slip boundary condition on the walls. For Knudsen number in the range of $10^{-3} < Kn < 10^{-1}$, it is still possible to use the Navier-Stokes equation model, however, slip boundary condition and temperature jump at the walls have to be taken into account. In the range of $10^{-1} < Kn < 10$ the flow is in transitional regime and the continuum concept can be no longer used. For $Kn > 10$ it is necessary to use the free molecular flow model [7]. If we assume

the characteristic dimensions of the channel $D \approx 1\,\mathrm{mm}$, then the channels considered in this thesis belong within the category of minichannels. Assuming the maximal flow velocity as $M = 1$, the Knudsen number is approximately $Kn \approx 1 \cdot 10^{-5}$, which certainly falls within the range of continuum flow[1].

This work follows upon a previous research done in the Department of Fluid Dynamics of the Institute of Thermomechanics of the Czech Academy of Sciences [8][9] and upon a previous work of the author conducted in the recent years therein [A1][A2][A3]. The previous research was motivated by the need to explore the flow in clearance gap in a dry screw compressor. The dimension of the clearance gap throat in the tested type was ranging from $200\,\mu\mathrm{m}$ to $500\,\mu\mathrm{m}$ which belongs to the category of microchannels. Numerical simulations and qualitative experimental study using Schlieren methods were carried out resulting in successful validation of the analytical model represented by Oseen equation [9]. Further research was focused on constant cross-sectional area channels with the characteristic dimension in the order of millimetres [8]. The aim of the later research was to experimentally investigate the flow of compressible fluid in channels of the height ranging from 0.5 mm to 2 mm, length of 100 mm and 200 mm, and of various width. The data were obtained using static pressure taps and with pitot tube located in the channel exit plane. The study revealed almost non-existing secondary flow structures, such as corner vortices, typical for rectangular channels of the standard size. The extent of secondary flow structures depends significantly on the channel aspect ratio (channel width to height), which was ranging from 5 to 200. The authors also aimed to investigate the losses and friction factor. For the determination of the friction factor, they used the method based on the one-dimensional model of an adiabatic flow with friction (Fanno flow) described for example in [10]. This method is based on the evaluation of the friction factor from the known distribution of the Mach number along the channel. Provided that the mean value of the Darcy friction factor $\bar{f}$ between two locations with the known Mach number can be calculated from equation

$$\bar{f}\frac{L}{D} = \left(\bar{f}\frac{L_{\max}}{D}\right)_{M_1} - \left(\bar{f}\frac{L_{\max}}{D}\right)_{M_2}. \tag{3}$$

where

$$\bar{f}\frac{L_{\max}}{D} = \frac{1-M^2}{\gamma M^2} + \frac{\gamma+1}{2\gamma}\ln\frac{(\gamma+1)\,M^2}{2\left(1+\dfrac{\gamma-1}{2}M^2\right)}. \tag{4}$$

However, in the case of aerodynamically choked flow, this method yields zero value of the mean friction factor in the vicinity of the channel exit plane. Since the exit plane

[1] Molecular mean free path can be calculated using the intermolecular collision model as $\lambda = \dfrac{k_{\mathrm{HS}}\mu\sqrt{rT}}{p}$, where $k_{\mathrm{HS}} = \dfrac{6}{5\sqrt{2\pi}} \approx 1.277$ [7].

is a location where the maximal value of the entropy is reached, it would be strange if the value of the friction factor was approaching zero in this location. Authors conclude with the suggestion to pay more attention to flow structures and the value of the friction factor in the vicinity of the exit plane and they urge for the use of other methods of the wall shear stress measurements. Possibly the methods which would not rely solely on pressure measurements such as the method described above.

Further research included repeated measurements and numerical simulations of the similar geometry - channel formed by two parallel plates of the length and width of 100 mm with a variable height from 0.5 mm to 4 mm [A1],[A2]. The aim was to obtain data using pressure and optical methods and explore the possibility of CFD simulations. The measured data were also used for the validation of the in-house code developed at the Faculty of Applied Sciences of the University of West Bohemia in Pilsen and for the calibration of RANS turbulence models [11]. Subsequent work was focused mostly on the improvement of the measurement facility and modelling using the developing code based on Discontinuous-Galerkin finite element method [A3] [12].

The problem of choked flow with losses is addressed e.g. in theoretical study of Hyhlík et al. [13] and in numerical and experimental investigation of Lijo et al. [14]. The work of Lijo deals with the flow in circular pipes and explore the influence of the losses on the critical conditions with the motivation to investigate this phenomenon influencing performance of sonic nozzles of the small diameter, which are used as a standard flow meters. Lijo concludes that the friction losses, and thus the presence of relatively thick boundary layer (inner pipe diameter was 15 mm), affect the choking in such a way that the sonic line is shifted from the exit plane upstream. And this shift depends, according to them, strongly upon the driving back pressure ratio. They also found out that the exit flow field changes even when the back pressure ratio is below the critical value of $\frac{p}{p_0} = 0.5283$ that applies for air as an ideal gas. Lijo claims that the actual critical pressure ratio, below which the further reduction of the back pressure does not influence the flow in pipe and the mass flow rate, is much lower than the theoretical value of 0.5283 and support this by the numerical study. The authors also address the phenomenon of supersonic region which forms in the pipe core flow downstream the sonic line. They claim that the reason is in the thinning of the boundary layer towards the exit, possibly with a zero boundary layer thickness right at the location of an exit plane forming divergent nozzle, however, they do not give any experimental evidence of this effect.

Considerably different results were obtained in theoretical study of Hyhlík et al. [13]. In this study the one dimensional model of the flow with friction was used to derive the theoretical relation of the critical pressure ratio for the constant

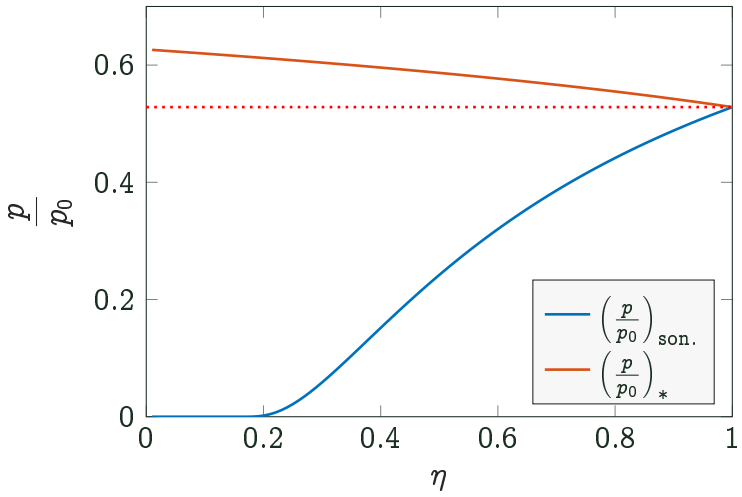

Figure 2: *Critical pressure ratio* (7) *and sonic pressure ratio* (9) *as a function of thermodynamic efficiency* η*. Red dotted line is the critical pressure ratio for isentropic flow* $\frac{p}{p_0} = 0.5283$*.*

thermodynamic efficiency η defined as

$$\eta = \frac{T_1 - T_2}{T_1 - T_{2s}}. \tag{5}$$

The critical conditions occur when a maximal value of the mass flow rate $\dot{m}$ through the channel is reached. Then, any further reduction of the back pressure p_b in the exit plenum does not influence the flow within the channel. This condition can be mathematically expressed for ideal flow as

$$\frac{\partial \dot{m}}{\partial \left(\frac{p_b}{p_0}\right)} = 0. \tag{6}$$

From this condition, while assuming the constant value of thermodynamic efficiency η lower than unity, the following formula for the critical pressure ratio $\left(\frac{p}{p_0}\right)_*$ can be derived

$$\left(\frac{p}{p_0}\right)_* = \left(z + \sqrt{z^2 + \frac{1-\eta}{\eta}\frac{2\gamma}{\gamma+1}}\right)^{\frac{\gamma}{\gamma-1}}, \tag{7}$$

where z is

$$z = \frac{1}{2\eta\left(\gamma+1\right)}\left[\eta\left(3\gamma+1\right) - 3\gamma + 1\right]. \tag{8}$$

Similarly, the expression for the sonic pressure ratio for given thermodynamic efficiency is then

$$\left(\frac{p}{p_0}\right)_{\text{son.}} = \left[1 - \frac{\gamma-1}{\eta\left(\gamma+1\right)}\right]^{\frac{\gamma}{\gamma-1}}. \tag{9}$$

Graph in Figure 2 shows the critical pressure ratio calculated using equation (7) and sonic pressure ratio using equation (9) with respect to thermal efficiency η. It is apparent that sonic and critical conditions are identical only for ideal case of the thermal efficiency $\eta = 1$. For any lower value of the thermodynamic efficiency, the critical and sonic conditions differ. Such difference would mean that the non-ideal flow would reach the maximum of the flow rate significantly before the sonic conditions occur. Therefore, it is a question which of the two conditions is appropriate for aerodynamic flow choking and what is the actual course of the state variables in the range of the pressure ratios between the two conditions.

It follows from the above that the flow in constant area channels of small dimensions is still deeply uncharted territory, particularly with respect to the lack of experimental data, which would allow to identify the nature of the flow and the data of the wall shear stress distribution along the channel walls. The phenomenon of the possible shift of critical conditions in the case of aerodynamically choked flow is also a topical problem awaiting deeper exploration. The aims of this work are summarized in the following section.

3 Aims of the Work

Research goals summarized in points are as follows:

- To determine what is the nature of the flow in the investigated channels using the available measurement techniques, including hot-film anemometry, and numerical simulations. And to describe the influence of the two different types of surface roughness on the flow development and possible transition to turbulence.
- To explore whether the critical conditions separates from the sonic conditions due to effects of friction under the conditions of aerodynamic choking as theoretically predicted in study [13].
- To determine whether the boundary layer might get thinner and the shear stress reduced in the region close to the channel exit.

4 Philosophy of Approach - Design of Experiments

The purpose of this section is to briefly introduce a plan how to reach the aims. The previous work on this topic revealed the necessity to choose more suitable method of surface shear stress measurement. Amongst all the conceivable methods, such as direct measurement using floating elements, liquid crystal coatings, Preston and Stanton tubes, fence probes and hot-film anemometry, the last one was chosen since there was one *Dantec Dynamics 55R45* hot-film probe readily available. However, the disadvantage of this method is its tedious calibration. To tackle this, *Calibration facility* of larger dimensions was constructed, manufactured, and used for the calibration against the fence probe. The calibration measurements also served as a test case to acquire necessary knowledge and experience in using hot film probes in high-speed compressible flow. Later, with the already calibrated hot film probe, the measurements were to be conducted in narrow channels using improved *Narrow channel facility* further described in section 5.2. Amongst the hot-film anemometry, the narrow channel facility enables us to use pneumatic and optical methods (interferometry).

Thanks to the cooperation with *PBS Velká Bíteš a.s.* company, which tackled the problem of flow in the gap between radial turbine impeller and the casing with an impact on the ventilation of this gap and subsequently the cooling of the impeller, we obtained precisely manufactured channel walls with three types of surface finishing. Therefore, we were able to extend the research by the exploration of the influence of surface roughness. As the measurement in the confined area is difficult and not always possible due to its small dimensions, the numerical simulations are also an essential part of this work, in particular with regard to the phenomenon of aerodynamic choking and possible shift of critical and sonic conditions.

The chosen combination of measurement methods should provide novel data, the later analysis of which together with the results of numerical simulations will help to answer the questions outlined above. Following section describes in detail all measuring methods used throughout this work.

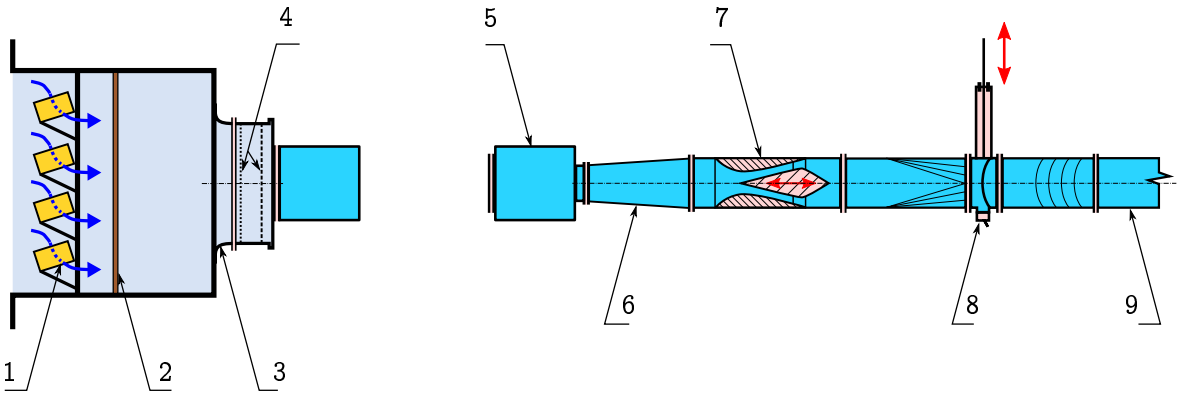

Figure 3: *Schematic diagram of the modular in-draft type wind tunnel: 1-Silica gel drier, 2-Filters, 3-Bellmouth contraction, 4-Honeycomb and wire meshes, 5-Settling chamber, 6-Diffuser, 7-Controll nozzle, 8-Quick acting valve, 9-Main duct to vacuum tank.*

5 Experimental Facilities & Measurement Techniques

5.1 Introduction

The experimental part of this work was carried out in the Laboratory of internal flows of the Institute of Thermomechanics of the Czech Academy of Sciences in Nový Knín. The laboratory is equipped with a modular in-draft type wind tunnel facility (Figure 3) which utilises 6300 m^3 vacuum tank. The air from the vacuum tank is evacuated using three liquid ring vacuum pumps each of them with an electrical input of 50 kW enabling long-time continuous operation of the facility for low mass flow rates. The vacuum tank is connected to a settling chamber through a piping equipped with a quick acting valve and a control nozzle. The settling chamber enables to mount different models or test sections to be measured. The in-drafted medium might be either non-preconditioned air sucked directly from the laboratory or dried and filtered outside ambient air. In the latter case, a bell mouth inlet with a honeycomb flow straightener and a set of wire meshes is used to remove swirl and turbulence from the flow. The control nozzle enables to continually change the pressure in the settling chamber from approximately 0.01 MPa up to the value close to the ambient atmospheric pressure.

The modular facility enabled us to use a variety of measurement techniques. Pneumatic methods were used to measure distributions of the static and total pressure in the channels. For the reason of small dimensions of the investigated geometries, a major advantage was a possibility to utilize the optical measurement techniques using Mach-Zehnder interferometer, which allows for measuring of the flow field without an undesirable intrusion of the flow. Since the wall-shear stress

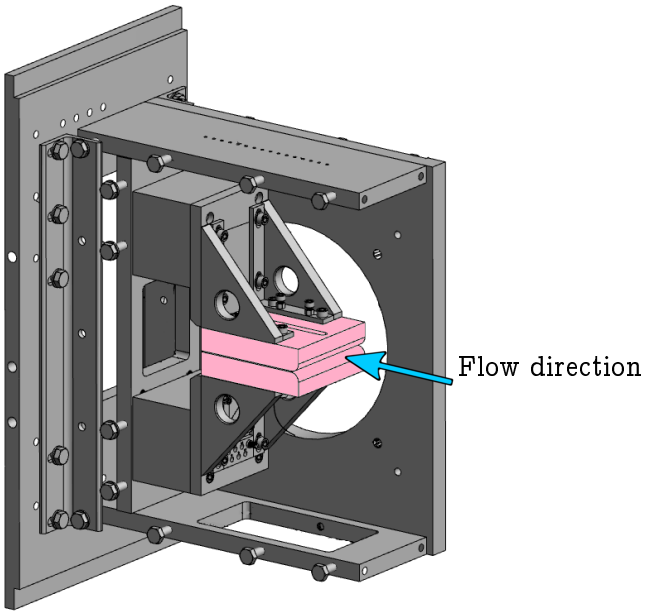

Figure 4: *View on the 3D CAD assembly of the narrow channel facility with uncovered left side wall and with the plates forming narrow channel coloured in purple.*

investigation was one of the main objectives, it was decided to calibrate a surface hot-film probe, which, unlike the other types of wall shear stress measurement methods, such as Preston, Stanton or sublayer fence probe, is suitable for the use in narrow channels thanks to its low intrusive nature. The principle of the hot-film probe measurements is described in section 5.7, while the whole calibration procedure together with the extensive set of measurements in the facility developed specifically for this purpose is described in detail in section 7.

5.2 Narrow Channel Facility

The narrow channel facility is shown in Figure 4. The actual channel is formed by two parallel walls made of stainless steel with optical windows as the side walls allowing optical access. The upper and lower wall is attached to the adjustable supporting elements which enable adjusting the gap between the walls in the range from zero to approximately 4 mm. The inlet part is of the quarter-cylinder shape of 8 mm in radius and the following straight part of the channel is 100 mm long. The width of the channel is 100 mm to achieve sufficient aspect ratio to eliminate secondary flow effects and to provide sufficiently long optical path necessary for adequate sensitivity of the interferometry. The whole assembly of the channel consisting of steel plates, supporting elements, and optical windows is fitted in the casing which is connected to the settling chamber (No. 5 in Figure 3).

Table 1: *Narrow channel walls roughness parameters as measured using Diavite DH-8 high precision surface roughness meter.*

Surface lay	in flow direction		perpendicular to flow direction	
	2A	2B	3A	3B
Ra (μm)	3.333	3.485	3.371	3.971
Rz (μm)	12.84	13.45	12.60	14.42
R_{max} (μm)	13.46	15.00	13.11	14.89

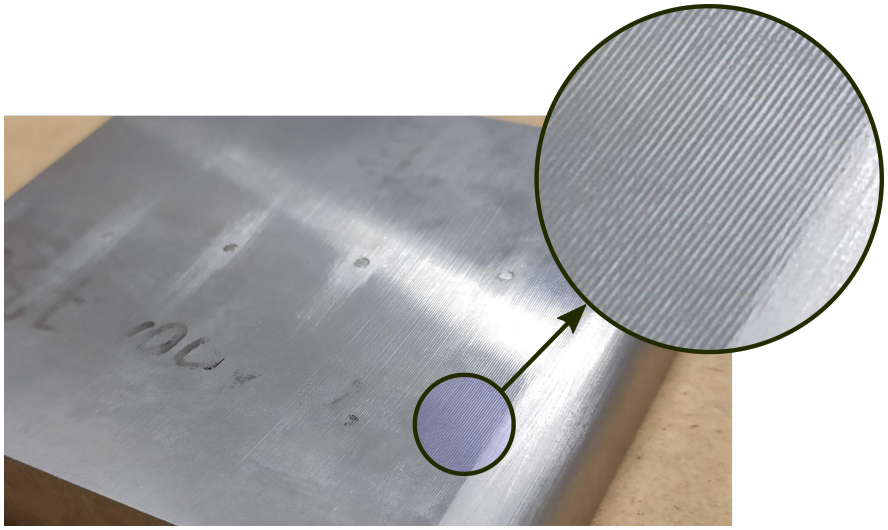

Figure 5: *Detail view of the roughened surface with the surface lay perpendicular to the flow direction (cross-flow roughness).*

The present version of the narrow channel facility is the improved version of the facility used for the preceding research [A3]. The facility was adapted for the use of hot-film probes and enables measurement of the total pressure at the outlet from the channel. Based on the experience gained in previous research, it turned out that the setting of the wall parallelism is essential and needs to be improved. Therefore, the side walls made of precise filler gauges were used for the measurements which did not require optical access. This measure allowed to minimize the necessity of the laborious setting of the parallelism of the walls after each measurement run and thus improved the repeatability of the experiments.

As the surface roughness effects were of particular interest, the channel walls were manufactured with three different surface finishes of the channel straight part. One pair of the walls was smooth and two others were roughened by end-milling process with the different lay of a surface (the direction of predominant surface pattern). One pair has the lay of the surface perpendicular to the flow direction (cross-flow) while the other has it in the direction of the flow (streamwise). The surface roughness

parameters measured at the right angle to the lay is shown in Table 1 and the picture of the actual roughened surface is on the photo in Figure 5.

Each pair of the plates forming the channel walls were instrumented by two resistance thermometers (RTD), which were located just under the wall surface. One plate of each pair contained 21 static pressure taps along the channel axis, which were densely spaced in the exit region and located under slight angle with respect to channel axis not to influence the taps located downstream (See Figure A.50 and A.51 in Appendix A for technical drawing of the narrow channel wall plates). The walls opposite to the tapped ones had five bores drilled to precisely accommodate hot-film probes. Since only one hot-film probe was available, only one of the bores could have been instrumented at a time, so the others were equipped with blind plugs carefully aligned with the wall surface. To minimize the influence of the upstream lying blind plugs, which were smooth even for roughened wall plates, the bores were located under the slight angle off the channel axis in the similar manner as the static pressure taps.

Since the total pressure measurement in the exit flow field including the traversing through the exit jet was of particular interest, the narrow channel facility was modified to allow measuring using the traversing device described in more details in section 5.4.

In summary, the facility enables to use the variety of independent measurement techniques capable to provide novel data of complex phenomena present during the compressible flow in narrow channels.

5.3 Hot-Film Sensor Calibration Facility

With regard to the geometry of narrow channels, it was decided to perform the calibration of the hot-film sensor in a geometrically similar device, yet of the dimensions large enough to enable measurements using other more intrusive techniques such as Preston or Stanton tubes or sublayer fence probes. Aforementioned considerations led to a design and manufacture of the facility hereafter referred to as *Calibration Channel*. The calibration channel, pictured in Figure 6, has an inlet of Bernoulli lemniscate shape. The follow-up 1.526 m long straight section of constant cross-sectional area is of the cross-sectional dimensions of 200x10 mm. The whole internal surface of the channel and inlet are smooth-finished and the transitions from the inlet part to the straight section were puttied and sanded smooth.

The calibration channel measurements aimed to clearly identify the flow conditions in the calibration channel to ensure fully developed flow and to provide exper-

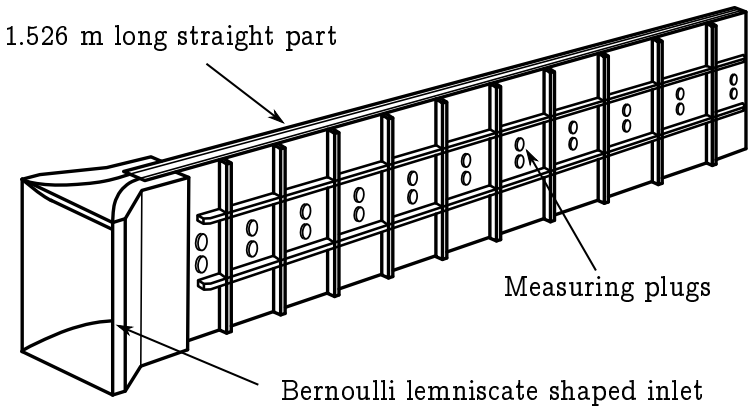

Figure 6: *Schematic depiction of the calibration channel.*

imental data for accompanying CFD computations [12]. The entrance length and an identification whether the flow is fully turbulent were of particular interest.

For this purpose, the calibration channel was designed to allow measurements using numerous techniques. The channel is equipped with 89 static pressure taps in the channel axis which were spaced more densely downstream from the location $\frac{x}{L} = 0.75$ to capture expected higher pressure gradient in this area. The pressure tappings are of conventional design - with the diameter of $d_{\text{tapp}} = 0.5\,\text{mm}$ and the depth of $2.5\,d_{\text{tapp}}$. In order to minimize the influence of the upstream orifice on the downstream one the densely spaced tappings were drilled slightly diagonally (under the angle of 10°) with respect to the channel axis. The wall opposite to the pressure tapped one has 21 holes of 16 mm in diameter, which can be either equipped with blind plugs carefully aligned with surface or with an instrumented plug enabling measurements using the sublayer fence probe, hot-wire probe, pitot probe or surface hot-film sensor. During the calibration measurements, the temperature was also measured at various locations for the purpose of temperature compensation of the hot-film probe measurements - one fast temperature sensor was placed upstream of the inlet to measure the inlet air total temperature and three others were placed in the measuring plug. One of those located in the plug was surface flush-mounted. The scheme of the calibration facility can be seen in Figure 6 and the technical drawing of the assembly with the exact dimensions and locations of the measuring plugs in Appendix B.

5.4 Pneumatic Measurements

Besides the measurements of the static pressure distributions along the calibration channel, the measurements of the total pressure in the channel axis using Pitot probe were also performed together with the measurements of total pressure profiles in a few strategic locations to assess the development of the flow along the channel.

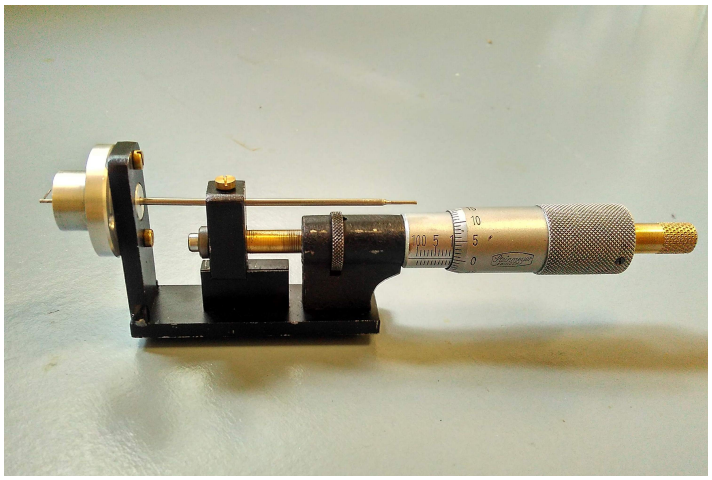

Figure 7: *Traversing device incorporating micrometric screw for a precision positioning of the Pitot probe.*

Exact positions of the static pressure tappings and of the total pressure measurement locations in the calibration channel can be seen in Appendix B. Measurements of the profiles of the total pressure in the calibration channel were conducted using the traversing device, incorporating calibrated micrometric screw enabling precision positioning of the Pitot probe within the channel. Figure 7 shows a picture of the traversing device.

In the case of the total pressure profiles measurements, the total pressure data were corrected for wall proximity effects. As described by MacMillan [15], the total effect of wall proximity might be split into two portions. The first one is the effect of the shear causing the displacement of the effective centre of the tube δ_{eff} from the geometric center towards the region of higher velocity. This correction was determined as

$$\frac{\delta_{\text{eff.}}}{D} = 0.15 \tag{10}$$

within the region where the ratio of the distance of the center of the tube y to its diameter D is $\frac{D}{y} < 0.5$. The second correction must be applied in the region in the immediate wall vicinity $\frac{D}{y} > 0.5$ where the streamline shift due to the velocity gradient in the boundary layer is limited by the proximity of the wall and the measured total pressure approaches the exact value as the tube is closer to the wall. Unlike the shear correction, this effect is dependent upon the Reynolds number $Re_{u_*} = \frac{u_* D}{\nu}$ based on the shear velocity u_* and the tube diameter D, and of the ratio $\frac{D}{y}$. The graph depicting the total displacement of the effective centre with respect to the ratio $\frac{D}{y}$ and Re_{u_*} can be seen in Figure 8. The value of the correction in the case when the probe lies on the wall was obtained from equation

$$\frac{\delta_{\text{eff}}}{D} = 0.1822\, Re_{u_*}^{-0.11} \tag{11}$$

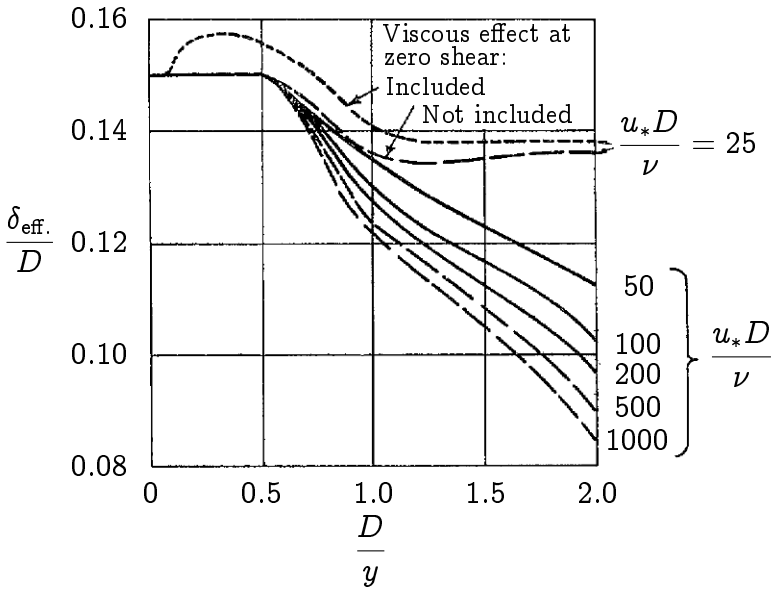

Figure 8: *Total displacement effect, due to MacMillan 1957 [15].*

which interpolates the points laying in the graph in Figure 9 at the position $\frac{D}{y} = 2$.

For the narrow channel facility, the static pressure distribution was also measured, however, due to small dimensions the total pressure was measured downstream the exit plane only (approximately 2 mm downstream the exit plane). In all measurements both the pressure at the inlet p_{in} and the pressure in the settling chamber p_{b} were also measured.

For the pressure data acquisition, two 16 channel *PSI 9116* pressure scanners and *Texas Instruments* data acquisition module connected to PC were used. Each scanner integrates 16 silicon piezoresistive pressure sensors and microprocessor that performs a correction for sensor zero, span, linearity, and thermal errors. The manufacturer guarantees the system accuracy of up to $\pm 0.05\%$ of the full-scale reading which is 15 PSI (103.4 kPa) [16]. The connection between the pressure scanners and pressure taps was realised through the sealed tubing of 0.5 mm in diameter.

5.5 Optical Measurements

Thanks to the presence of density gradients the compressible fluid flow is well suitable for an investigation using optical methods which are based either upon the dependency of the phase shift of the light on the refractive index of the medium, through which the light passes (interferometry), or upon the deflection of the light by a refractive index gradient in the medium (schlieren, shadowgraph).

The interferometry method used mostly for the quantitative investigation of flow fields is based upon the physical phenomenon that the speed of the propagation of the light in the medium depends on the index of refraction of the medium, through

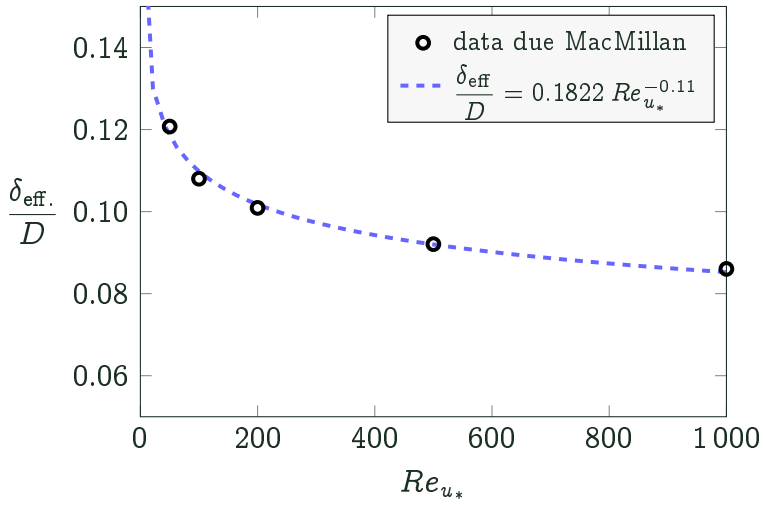

Figure 9: *Approximation of the wall proximity correction for the total pressure probe laying on the wall.*

which the light passes, and the index of refraction in turns depends on its density. Therefore, using the interferometry, the changes of density can be measured directly enabling to observe density fields. Subsequently, the fields of other properties, which depend on the density, can be determined [10].

The qualitative schlieren technique is based upon the effect that the light passing through the medium, in which the gradients of the index of refraction are present, is deflected producing shadow patterns on the viewing screen. These shadow patterns are representations of expansion and compression regions in the investigated flow field.

The mentioned optical methods are quite useful due to its non-intrusive nature, which enables us to measure the fluid flow in the narrow channels without the undesirable intrusion of any disturbances to the flow field. Since the characteristic dimension (most frequently the height) of the narrow channels is comparable with the dimensions even of smallest probes, any probe intrusion could considerably impaired the measurements.

Laboratory of internal flows in Nový Knín is equipped with a Mach-Zehnder type interferometer[2]. The scheme of the optical path of the used apparatus is given in Figure 10. During the exposition, the light from the light source passes through the monochromatic filter and field lens to make a collimated beam of monochromatic light. The beam is then split by the beam splitter forming a reference and a sample beam. The sample beam further passes through the test section, in which the measured model is placed. Meanwhile, the reference beam is reflected by the mirror

[2]This type of interferometer was invented independently in 1891 and 1892 by Swiss physicist Ludwig Zehnder and by Austrian physicist Ludwig Mach (the son of Ernst Mach). [17]

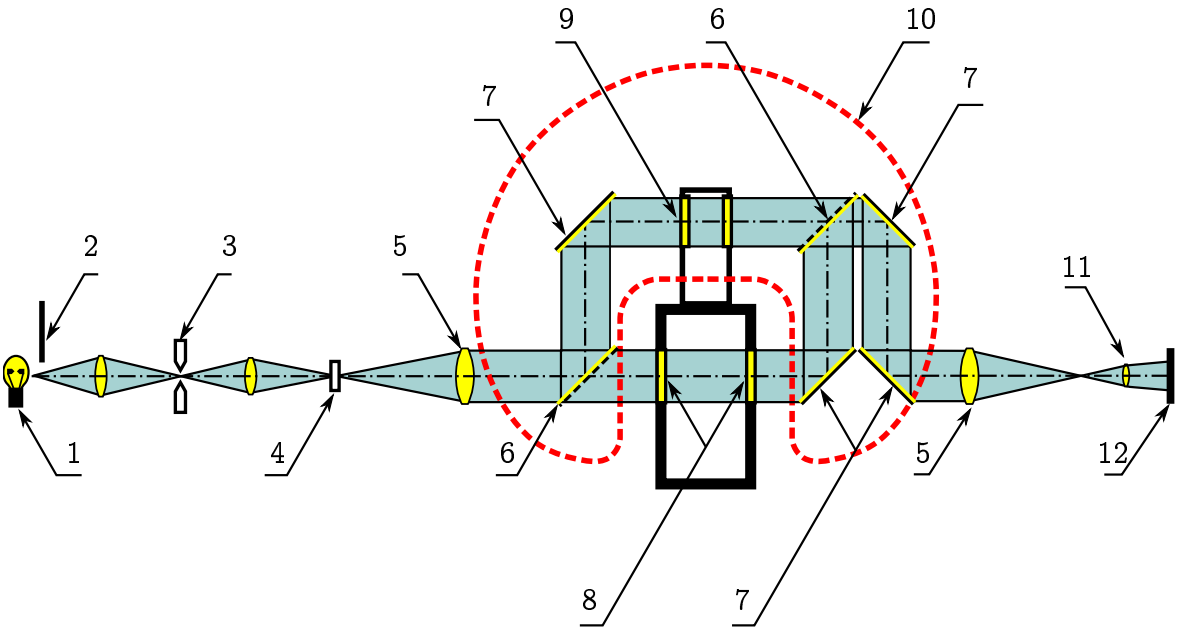

Figure 10: *Schematic depiction of the light beam passing through the Mach-Zehnder interferometer: 1-Mercury lamp, 2-Flap, 3-Spark-light source, 4-Monochromatic filter, 5-Field lens, 6-Beam splitter, 7-Mirror, 8-Test section windows, 9-Compensating glasses, 10-Casing of the interferometer, 11-Objective lens, 12-Image plane (CCD)*

to the upper branch of the interferometer. In the upper branch, the compensating glasses are placed in order to retain the same optical path as for the sample beam. Then, both sample and reference beams meet again and after passing through several other optical elements these are further reflected at the image plane (CCD camera). Lasers, spark light generators or light emitting diodes can be used as a light source. In our case, the spark light source was used providing sufficient light intensity and sufficiently short exposition time (approximately $2 \cdot 10^{-6}$ s), which allows taking an image of instantaneous flow situation even when the flow is unsteady.

When there is no flow in the test section and the mirrors are adjusted exactly in line and parallel, then both beams have the same phase shift and no interference patterns can be observed at the image plane (camera). This set-up is known as an *Infinite-Fringe* technique. During the measurement there are significant density gradients and thus gradients of the index of refraction in the test section, causing the phase shift of the sample beam. If there is a phase shift between the sample and reference beams, the interference patterns are formed and it is possible to take the interferograms using the digital camera. The camera used was 80 Mpx *Phase One XF IQ3*. An example of the interferogram is shown in Figure 11a, while the actual interferometer in operational position is depicted in Figure 11b.

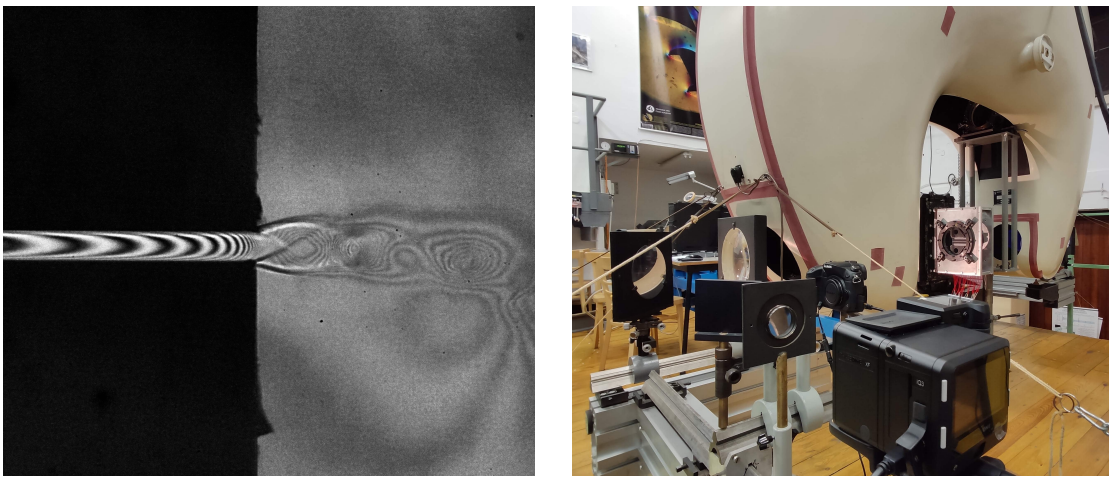

(a) *(b)*

Figure 11: *Example of the interferogram (flow at and downstream of the exit part of the narrow channel) (a), and Mach-Zehnder interferometer in operational position above the narrow channel facility (b).*

Evaluation of the flow parameters from the interferograms is based upon a Lorenz-Lorentz equation[3], which relates the density ρ and the absolute index of refraction n of the transparent medium as follows

$$\frac{n^2-1}{n^2+2}\cdot\frac{1}{\rho}=r, \tag{12}$$

where r is a specific refraction. It is experimentally verified, that for the changes of density, pressure, temperature and even for some state changes of the transparent media, specific refraction can be considered as a constant. Since the index of refraction for the air $n \doteq 1$, it is possible to rewrite the relation (12) into equation

$$r=\frac{n^2+1}{n^2+2}\cdot\frac{n-1}{\rho}\doteq\frac{2}{3}\cdot\frac{n-1}{\rho}, \tag{13}$$

which can be simplified to Gladston-Dale relation

$$\frac{n-1}{\rho}=K, \tag{14}$$

where K is the Gladston-Dale constant.

The absolute index of refraction of the dry air under the normal conditions ($t = 20\,^{\circ}\mathrm{C}$, $p = 101\,325\,\mathrm{Pa}$) can be calculated from equation [19]

$$n_N^2=1.00057642+\frac{3.277}{\lambda_V^2-5685}, \tag{15}$$

[3]Discovered independently by the Danish mathematician and scientist Ludvig Lorenz in 1869 and by the Dutch physicist Hendrik Lorentz in 1878. [18]

Table 2: *Gladston-Dale constant K in dry air and other gasses for some characteristic wavelengths [20].*

		$K \cdot 10^4\,(\mathrm{m^3 \cdot kg^{-1}})$			
$\lambda\,(\mathrm{mm})$	color	air	O_2	N_2	Ar
$4.358 \cdot 10^{-4}$	blue	2.297	1.935	2.418	1.606
$5.461 \cdot 10^{-4}$	green	2.272	1.907	2.393	1.589
$5.770 \cdot 10^{-4}$	yellow	2.267	1.895	-	1.587
$5.791 \cdot 10^{-4}$	yellow	2.267	-	-	-

where λ_V (in nm) is a wavelength of the light in vacuum. Density of the dry air under normal conditions is $\rho_N = 1.2932\,\mathrm{kg \cdot m^{-3}}$. Knowing this, it is possible to determine the Gladston-Dale constant from equation (14) for dry air and given wavelength λ_V. In Table 2 the values of K in the dry air are shown for some characteristic wavelengths as well as values for another common gasses [20].

Since the influence of the humidity on the K is not much significant in comparison with other errors emerging during the evaluation, the dry air values are usually used for measurements in the aerodynamic laboratories where the air is dried [19]. The density of the dry air can be calculated using the equation

$$\rho = \rho_N \frac{1}{1 + \alpha t} \cdot \frac{p}{p_N}, \tag{16}$$

where $\alpha = 0.00367\,^\circ\mathrm{C}^{-1}$ is a coefficient of thermal expansion of air, t is a temperature in Celsius degrees and p is a pressure. Subscript $_N$ denotes normal conditions.

From geometrical optics and considering the assumption of negligible influence of beam curvature on the optical path length, the following relation can be derived

$$\rho = \rho_{\mathrm{ref.}} - Ci. \tag{17}$$

$\rho_{\mathrm{ref.}}$ is a known reference density (density of free stream, density in stagnation point on an airfoil), i is a number of interference fringe from the reference one and C is a constant involving wavelength of the used light, Gladston-Dale constant and width of the test section L_{ts}

$$C = \frac{\lambda}{L_{\mathrm{ts}} K}. \tag{18}$$

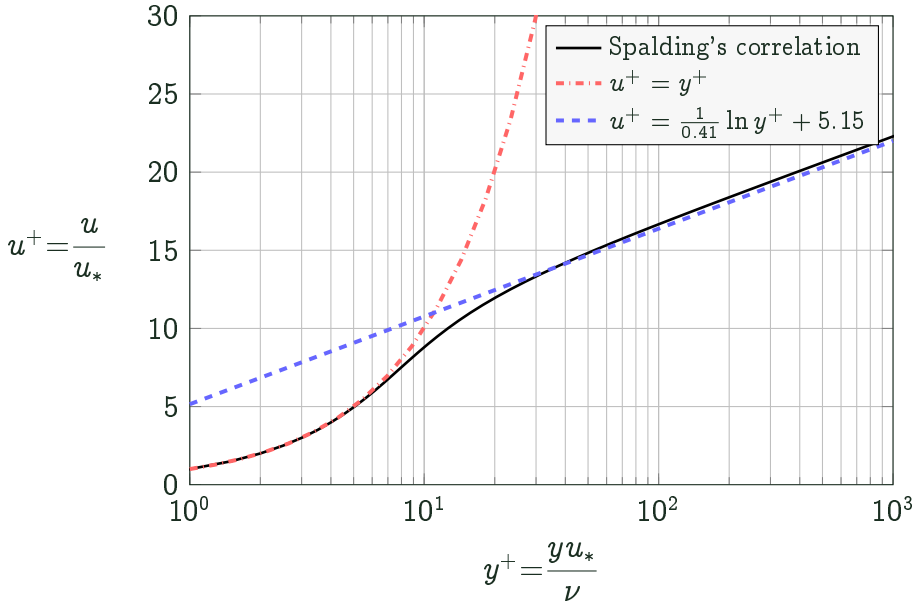

Figure 12: *Law of the wall for fully developed turbulent boundary layer*

5.6 Sublayer Fence Probe Measurements

Calibration of the hot-film sensor was made using the sublayer fence probe, which was already calibrated. The working principle of the sublayer fence probe is similar to that of Preston or Stanton probes and is based upon the assumption of the self-similar velocity distribution in the turbulent boundary layer known as *Law of the Wall*. The law of the wall states that in the turbulent boundary layer, there is a region close to the wall where the velocity profile depends upon the wall shear stress, physical properties of the fluid, and the distance from the wall and at the same time does not depend on the state of the flow outside the boundary layer. This law is usually given in the form

$$\frac{u}{u_*} = f\left(\frac{yu_*}{\nu}\right), \tag{19}$$

where $u_* = \sqrt{\frac{\tau_w}{\rho}}$ is the friction velocity and $\frac{yu_*}{\nu} = y^+$ is the dimensionless wall distance. The distribution of the dimensionless velocity $u^+ = \frac{u}{u_*}$ with respect to dimensionless wall distance y^+ is pictured in the semilogarithmic plot in Figure 12. The region of the applicability of the law of the wall can be divided to two regions with buffer layer in between. The first one lying at $y^+ < 5$ is called viscous sublayer and the following linear relation is applicable

$$u^+ = y^+. \tag{20}$$

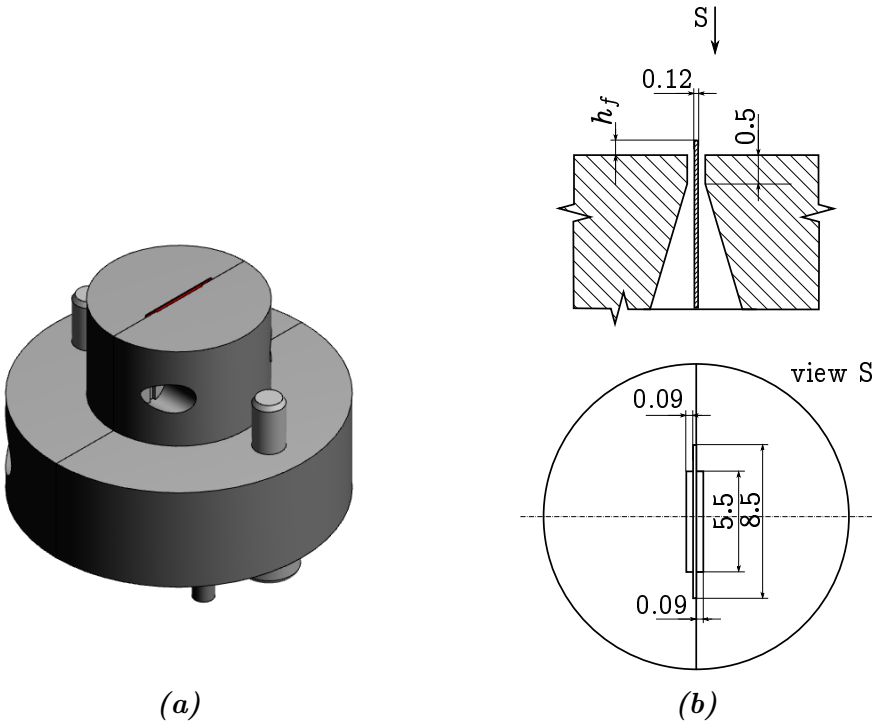

Figure 13: *3D view of the sublayer fence probe (a) and schematic depiction of the design with main dimensions (b).*

The second one lying at $y^+ > 30$ is the log-law region where the relation between y^+ and u^+ is logarithmic

$$u^+ = \frac{1}{0.41} \ln y^+ + 5.15. \tag{21}$$

The law of the wall thus enables us to determine the wall shear stress from the velocity measured in the region of its applicability and if the physical properties of the flow are known. If the obstacle in the form of fence is placed in the law of the wall region, then the following relation between fence height h_f, pressure difference measured using pressure taps located immediately upstream and downstream of the fence Δp, and shear stress can be written:

$$\frac{\Delta p}{\tau_w} = f\left(\frac{h_f u_*}{\nu}\right). \tag{22}$$

Assuming the universal validity of the law of the wall for turbulent flow, the above outlined relations are also universal and the obtained calibrations can be used for any geometrically similar probes [21].

The actual design of the sublayer fence probe is the same as of the probe manufactured in the Institute of Thermomechanics AS CR in the seventies and is shown in Figure 13. The fence is made of razor blade, which is clenched between two half cylindrical bodies with the slits working as the pressure taps right upstream and

downstream of the fence. The calibration of this probe was thoroughly described in [21]. The calibration was made against the floating element in the turbulent boundary layer on the wall with the zero pressure gradient. The calibration curve of the form

$$\bar{y} = a + b\bar{x} = -0.525 + 0.710\bar{x} \tag{23}$$

where

$$\bar{x} = \log \frac{\Delta p h_f^2}{\rho \nu^2}; \quad \bar{y} = \log \frac{\tau_w h_f^2}{\rho \nu^2} \tag{24}$$

was obtained for the range of the Reynolds number based on the shear velocity u_* defined as $u_* \equiv \sqrt{\tau_w/\rho}$ and the height of the fence h_f

$$4.7 < \frac{u_* h_f}{\nu} < 45.3. \tag{25}$$

According to [21] the obtained calibration curve approximates the value of the wall shear stress with the accuracy of 2%.

The recommended ratio of the fence height to boundary layer thickness is within the interval

$$1 \cdot 10^{-4} < \frac{h_f}{\delta} < 0.01. \tag{26}$$

Therefore, assuming boundary layer thickness of half dimension of the channel width $\delta \simeq 5\,\mathrm{mm}$, the fence height should be then in the interval $5 \cdot 10^{-4}\,\mathrm{mm} < h_f < 0.05\,\mathrm{mm}$. To obtain reasonable sensitivity of the sublayer fence probe, the highest possible fence height that meets mentioned requirements ($h_f = 0.05\,\mathrm{mm}$) was chosen and used in the case of the probe newly manufactured for present measurements.

5.7 Surface Hot-Film Sensor Measurements

Though the idea of relating the heat transfer from an electrically heated strip embedded in a surface and the wall shear stress is known for several decades (e.g. pioneering work of Liepmann and Skinner [22]), its usage for quantitative measurements is still limited due to difficult calibration. The difficulty lays mainly in the heat transfer to the probe substrate, which is problematic to quantify, and the dependency on the flow temperature, both of which must be compensated.

Despite all the drawbacks, the method of wall hot-film measurement is important since it is one of the few minimal intrusive methods suitable to effectively investigate the surface shear stress even in small confined geometries where the complete measurement of boundary layer is impossible. Among its significant benefits, we can also include fast frequency response and thus the ability to provide time-resolved data,

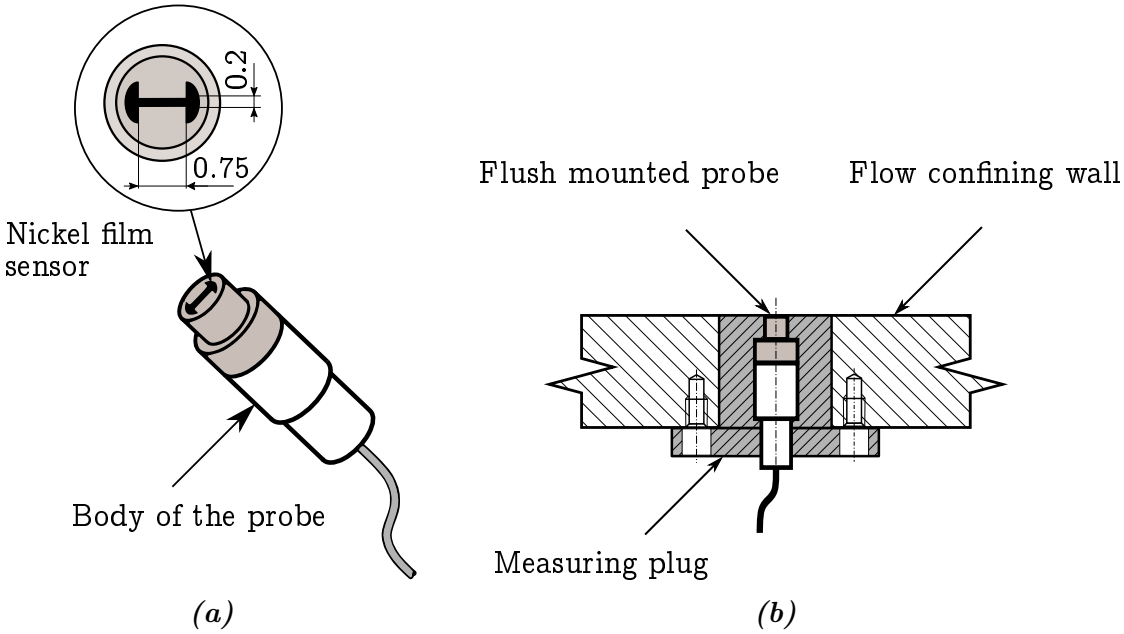

Figure 14: *Dantec Dynamics 55R45 hot-film probe (a) and the depiction of its mounting to channel wall with sensor flush with a wall surface (b).*

from which it is possible to identify boundary layer transition and flow separation even using uncalibrated sensor [23].

The calibration of a surface hot-film sensor might be made against a Preston tube, for which the universal calibration was developed (assuming the flow with the known law of the wall across the tube diameter), or against a calibrated Stanton tube or sublayer fence probe. Due to the availability of a calibrated sublayer fence probe and due to its better sensitivity (almost double the pressure difference Δp than in the case of a Stanton probe), the latter option was chosen. The calibration procedure and measurements are described in detail in section 7.

5.7.1 Constant Temperature Anemometer Operation

The *Dantec Dynamics 55R45* hot-film sensor (Figure 14) was operated in constant temperature mode using *A. A. Lab AN1003* anemometry system. The overheat temperature of the sensor was set after consideration of the highest operating temperature of the nickel heat element which is 300 °C according to the manufacturer and the fact that increasing sensor temperature increases its sensitivity [24]. The sensor temperature should also satisfy the inequality

$$5\sqrt{\frac{\mu k}{c_p \rho^2}}\sqrt{\frac{\rho}{\tau_w}} < L < 125\frac{c_p \mu^2}{k\rho}\sqrt{\frac{\rho}{\tau_w}}, \tag{27}$$

where the air density ρ, dynamic viscosity μ, and thermal conductivity k are evaluated at the film overheat temperature and L is the length of the heated element in the flow direction [22]. After evaluation of the wall shear stress from the sublayer fence probe measurements, this inequality appeared not limiting for the expected range of the wall shear stress and Mach numbers. On the other hand, the high film temperature might cause excessive heat transfer to an opposing channel wall in case of small gaps. Considering this, the overheat temperature was set at 120 °C.

Since the film sensor has a low but not inconsiderable heat capacity, it takes some finite time to respond on any change in the flow field, in which it is being operated. Due to this effect, the anemometry system must be reasonably set in terms of damping, offset and sampling frequency to allow to measure as much flow field activity and prevent unstable behaviour of the system. The most convenient method to determine the frequency response of a CTA bridge is to measure its response to a square wave pulse - so-called *Square wave/pulse test* and observe the output signal using an oscilloscope. By using this method the sensor was determined to have a frequency response of approximately 25 kHz. Based on this, the sampling frequency was set at 50 kHz. Prior the sampling by *Texas Instruments* data acquisition module connected to PC, the output signal was filtered through a low pass filter (anti-aliasing filter) with a setting for the cut off frequency set at 16 kHz, which is the maximum for the used anemometry system. The procedure of setting up the used anemometer is described in detail in [25] and [26].

5.7.2 Flow Character Identification

One of the advantage of the hot film-probe is its capability of high-frequency sampling of the flow instabilities. This feature can be advantageously used for the flow characterization from the sensor raw signal without the necessity of sensor calibration. Several methods have been devised and reported to interpret the flow regime from a raw hot-film probe signal [27][28]. These methods are most commonly based on the change of the signal root mean square (RMS) or other signal characteristics such as the signal skewness. The one reported by Hodson et al. [27], which uses skew function, had already been used before in Laboratory of internal flows of the Institute of Thermomechanics for qualitative evaluation of the hot-film array measurements of the flow past a transonic airfoil [A4]. This method uses the skew function (SF) defined as

$$SF = \frac{\frac{1}{n}\sum_{i=1}^{n}(x_i - \overline{x})^3}{\left[\frac{1}{n-1}\sum_{i=1}^{n}(x_i - \overline{x})^2\right]^{\frac{3}{2}}}, \tag{28}$$

where x stands for measured signal variable (voltage) and $\bar{x}$ its mean value. According to this method a typical nature or bypass transition behaviour in terms of intermittency γ, which describes the fraction of time during which the flow at a certain position is turbulent, might be identified [28]. Zero skewness corresponds to the flat time-resolved signal without any random disturbances (e.g. pure laminar flow, $\gamma = 0$; or pure turbulent flow, $\gamma = 1$). For $\gamma = 0.25$, the skewness reaches its maximum. At $\gamma = 0.5$ where equal periods of laminar and turbulent flow exist, the skew function decreases to zero. This point at the same time typically coincides with the random fluctuation maximum. At $\gamma = 0.75$ the skewness exhibits a minimum. The shortcoming of this method is that the signal noise and other random effects (e.g. shock oscillations) may lead to a noisy and messy skew distribution which might then deviates significantly from the described ideal distribution. However, this concerns in particular the flows past cascades where shock waves appear frequently, which is fortunately not so much the case of the channel flow.

The other method relies on the evaluation of the root mean square (RMS) of the signal, which is defined for discrete data as

$$RMS = \sqrt{\frac{1}{N}\sum_{i=1}^{n} x_i^2}. \tag{29}$$

However, this method is rather comparative than an absolute measure of the flow regime. Then, lower values of RMS suggest that the flow is laminar. Nevertheless, in adverse pressure gradients the flow regime identification using RMS should be accompanied by flow visualisation to identify possible separation bubble, which might significantly affect the resulting RMS value [29].

5.7.3 Hot-Wire Anemometry

One of the first test measurements also included an examination of the inlet turbulence level at the calibration facility inlet to obtain reliable data for the inlet boundary condition in numerical simulations. Measurements were carried out using *Dantec 55P11* hot-wire probe and *Dantec StreamLine* hot-wire anemometer system.

Resulting turbulence intensity Tu in the location in the middle of the channel and 100 mm in front of the inlet are listed in Table 3 for different pressure ratios.

Table 3: *Turbulence intensity measured 100 mm in front of the calibration channel inlet for various pressure ratios π.*

pressure ratio π	0.2	0.3	0.4	0.5	0.6	0.7	0.8
Tu (%)	1.29	1.25	1.19	1.26	1.22	1.27	1.3

5.8 Uncertainties of the Measurements

Measurement uncertainties of the pneumatic measurements were evaluated according to the standard methodology consisting of the evaluation of Type A (where the series of measurements were available) and Type B uncertainties [30]. Finally, the combined standard uncertainty and expanded uncertainty were determined. During the sampling of the pressure data, pressure scanners sample the signal with the frequency of 100 Hz. A *LabView* data acquisition program then automatically computes type A uncertainty based on the standard deviation of the data series taken during one measuring point. Measurement of the static pressure was carried out several times for each measurement point, therefore, the standard deviation was determined from repeated measurements. Since the distribution of the total pressure was measured just once, the standard deviation was determined from the sample series taken during each measurement point. Nevertheless, the values of standard deviation of total and static pressure measurements were of comparable magnitudes.

For the hot-film probe measurements, the repeatability tests were not yet performed, therefore, no absolute values of uncertainty can be given. Similar measuring arrangements reported in literature [31] usually gives the uncertainty of up to 10% or less for less thermally loaded flows [24].

The uncertainty of the numerical simulations is addressed separately in Section 6.5.

6 Numerical Simulations

6.1 Introduction

For its cost effectiveness and the ability to explore many design variants in relatively short time, the numerical simulations play increasingly important role in nowadays applied research and industry. Since its first practical usage in the 1960s, the Computational Fluid Dynamics (CFD) established itself not only as a powerful design tool but in many cases represents a role of theory, to which the results of experiments are compared. Nevertheless, one might keep in mind that the mathematical models are limited by assumptions from which the models were derived. For that reason, it is broadly accepted that the numerical simulations should be accompanied by validation experiments. Although this is true, it is useful to accompany also an experimental research with CFD computations, which in this case might provide additional data and lead to better understanding of the given problem. In this work, the CFD is used both as a tool to support the experiments and as a subject of investigation. Though, in the case of *calibration channel* the simulations were used to support the experimental results, while in the case of the narrow channel flow, the most appropriate numerical model was searched for. Besides that, the results of both experiments were also used for a validation purposes of the numerical solver based on the discontinuous Galerkin method developed at the Research centre of the Faculty of Applied Sciences (NTIS) at the university of West Bohemia. The in-house code and its validation is thoroughly described by Helena Prausová in her doctoral thesis [12]. The next sections describe the procedures and methods used for the present research. The synthesis and evaluation of the results will be presented in Chapter 9.

6.2 Numerical Methods

The numerical computations presented in this thesis were performed using Ansys Fluent 19.3 commercial code. This software package uses finite volume method to solve the governing Navier-Stokes equations for compressible fluid flow. This set of equations consists of continuity equation, momentum equations, energy equation and the equation of state. In the index notation, the Navier-Stokes equations can be written in 2D as

$$\frac{\partial \rho}{\partial t} + \frac{\partial \left(\rho u_j\right)}{\partial x_j} = 0, \tag{30}$$

$$\frac{\partial \left(\rho u_i\right)}{\partial t} + \frac{\partial \left(\rho u_i u_j\right)}{\partial x_j} = -\frac{\partial p}{\partial x_i} + \frac{\partial \tau_{ij}^{\text{eff.}}}{\partial x_j}, \tag{31}$$

$$\frac{\partial \left(\rho e_0\right)}{\partial t} + \frac{\partial \left(\rho h_0 u_j\right)}{\partial x_j} = \frac{\partial}{\partial x_j}\left(\tau_{ij}^{\text{eff.}} u_i + \rho \alpha^{\text{eff.}} \frac{\partial h}{\partial x_j}\right), \tag{32}$$

where $i = 1,\ 2$ is an index of Cartesian vector component and $j = 1,\ 2$ is a summation index.

Since the air could be considered as an ideal gas for the conditions considered in the narrow channels, the ideal gas flow model was used throughout all computations. Hence, the equation of state has a form

$$\rho = \frac{p}{RT}, \tag{33}$$

where p is the pressure, R the specific gas constant, and T is the thermodynamic temperature. The temperature dependence of the viscosity was modelled using the Sutherland's law given by equation

$$\mu = \mu_{\text{ref.}} \left(\frac{T}{T_{\text{ref.}}}\right)^{\frac{3}{2}} \frac{T_{\text{ref.}} + S}{T + S}, \tag{34}$$

where $\mu_{\text{ref.}} = 1.716 \cdot 10^{-5}\,\text{kg}\cdot\text{m}^{-1}\cdot\text{s}^{-1}$ and $T_{\text{ref.}} = 273.11\,\text{K}$ are reference viscosity and temperature and $S = 110.56\,\text{K}$ is Sutherland's constant.

For the turbulence modeling the Reynolds-averaged Navier-Stokes (RANS) approach was chosen. Using this approach the instantaneous variables in the governing equations are decomposed into mean and fluctuating components. As a result, this decomposition of the governing equations gives rise to additional terms, representing the effects of turbulence, which need to be modelled to close the system of equations.

There are many turbulence models with different levels of complexity available. The $\text{k} - \omega$ SST turbulence model of Menter [32] can be considered as the workhorse of the current industrial simulations. This model is a Linear eddy-viscosity model based on the Bousinesque eddy-viscosity assumption, and hence, neglects the turbulence anisotropy. Another class of turbulence models is based on the idea of the direct simulations of the components of the Reynolds stress tensor. This idea gave birth to so called Reynolds stress models (RSM), in which additional transport equations are solved for the Reynolds stress tensor components. These models are, however, substantially more hardware demanding. For this reason, the Explicit Algebraic

Reynolds Stress Models (EARMS), offering some of the advantages of the RSM models but at the computational cost comparable with $k-\omega$ SST models, were devised. According to studies such as [33], the EARMS models should better predict secondary flows which are important in the simulations of the hub sections of turbine blades or the airfoils with high curvature. On the other hand, this models should give very similar results in the case of the flat plate as the models upon which they are based. Therefore, it was of the interest, whether the EARMS model brings any improvement over the classical $k-\omega$ SST model in the case of the narrow channels.

Throughout this work, various RANS turbulence models were used either to support the calibration measurements for the hot-film and sublayer fence probes in the case of calibration channel or to obtain computational data of the flow in narrow channel. Simulations of the calibration channel were performed using the $k-\omega$ SST and EARSM $-\omega$ fully turbulent models and using SST – Transitional model capable to predict the transition to turbulence. However, the usage of the transitional models for the simulations of the calibration channel was later abandoned due to the use of the turbulators at the channel inlet, which makes the simulation of the transition unimportant since the turbulent regime was forced from the very inlet of the channel. In the case of the narrow channels, the SST – Transitional and $k-\omega$ SST turbulence models with the intermittency model of transition were used besides the already mentioned $k-\omega$ SST and EARSM $-\omega$ turbulence models.

All computations were performed using the density based implicit solver and using the second order accuracy upwind schemes in space. The inviscid fluxes were approximated using the Advection Upstream Splitting Method (AUSM) upwind scheme with linear reconstruction. The computations were conducted using the high performance computing cluster of the Institute of Thermomechanics using 16 cores of the Intel Xeon E5-2683 v4 CPU running at 2.10 GHz.

6.3 Numerical Simulation of the Calibration Channel

6.3.1 Computational Domain and Boundary Conditions

Calibration channel computations were performed to support the measured data and improve the calibration of the fence probe and consequently of the hot-film probe. The two-dimensional computational domain with boundary conditions is shown in Figure 15. The boundary conditions were as follows:

- Pressure inlet
  - Total pressure; $p_0 = 101325\,\mathrm{Pa}$
  - Total temperature; $T_0 = 300\,\mathrm{K}$

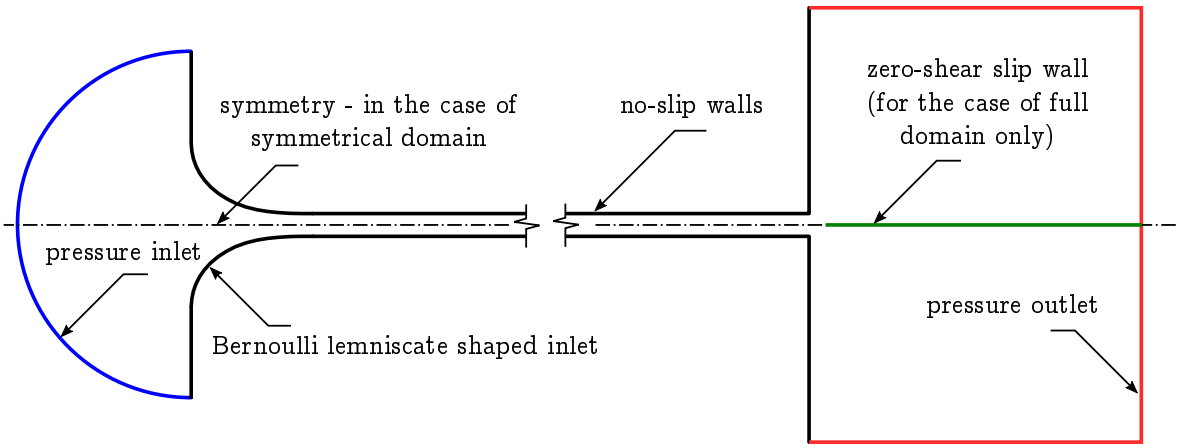

Figure 15: *Scheme of the calibration channel computational domain.*

  - Turbulence intensity; $Tu = 1.3\,\%$
  - Eddy viscosity ratio (Ratio of the eddy viscosity and molecular viscosity); $\frac{\mu_t}{\mu} = 10$
  - Intermittency; $\gamma = 1$; (For Transitional SST model only)

- Pressure outlet
  - Static pressure according to the desired pressure ratio π
  - Other quantities extrapolated from flow field

- Walls
  - Zero velocity components; $u_i = 0$
  - Zero heat flux through the wall

- Symmetry
  - Zero normal components of all quantities

The turbulence boundary conditions at the inlet are based on the hot wire measurements which gave the turbulent intensity at an inlet of approximately 1.3 % (see Table 3.

6.3.2 Computational Mesh

Since the problem is symmetric about the channel axis, it is advantageous to speed up the computation by using only the half of the domain with the symmetry boundary condition in the channel axis. Nevertheless, some simulations were also performed using the full domain to make sure the results on the symmetric domain corresponds

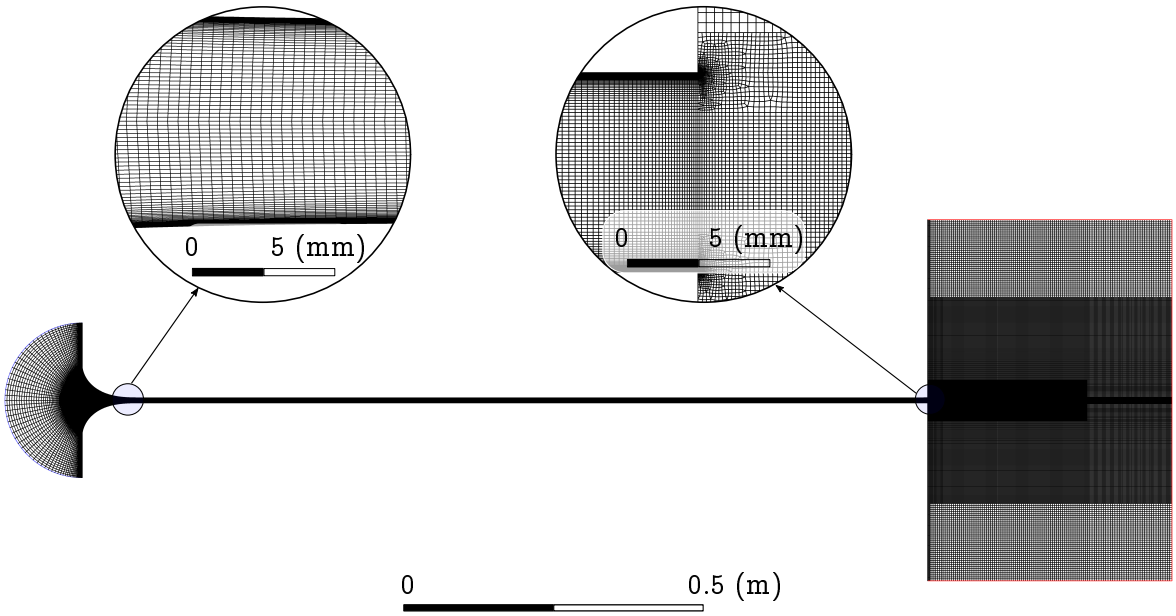

Figure 16: *Computational mesh of the calibration channel.*

well. The simulation on the full domain have, however, brought up the problem with convergence particularly in the area of the channel exit, which is realised as the sudden expansion from the channel to the plenum. It is because this configuration is naturally unstable and the exit plume tends to oscillate between two stable positions - attracted either to the upper or lower exit plenum wall. This unstable behaviour was later observed during the measurements using optical method. To make the computations converge well using the steady state solver, the infinitely thin wall with the zero–shear slip boundary condition was placed in channel axis, certain distance downstream from the channel exit (see Figure 15). This measure worked well and the results of the test cases were the same as for the symmetric domains, therefore, the symmetric mesh was used for most of the computations. Besides that, the grid convergence study was performed using two finer meshes according to the methodology described by Roache in [34]. A similar study was also performed for the narrow channel. The details of both these studies can be found in Section 6.5.

The computational mesh was created in ANSYS ICEM mesh generator and consisted of 178 218 quadrilateral elements (for the symmetric case) with reduced spacing in the channel wall vicinity to satisfy the requirement of the dimensionless wall distance less then unity $y^+ < 1$, necessary for the use of turbulence models resolving viscous sublayer. The mesh was coarsened using the hanging nodes in the outlet plenum region to spare computational resources, except the area of the exit jet plume where the steep gradients of flow variables are expected. Figure 16 shows the calibration channel computational mesh with the detail view of the region at the channel outlet and inlet.

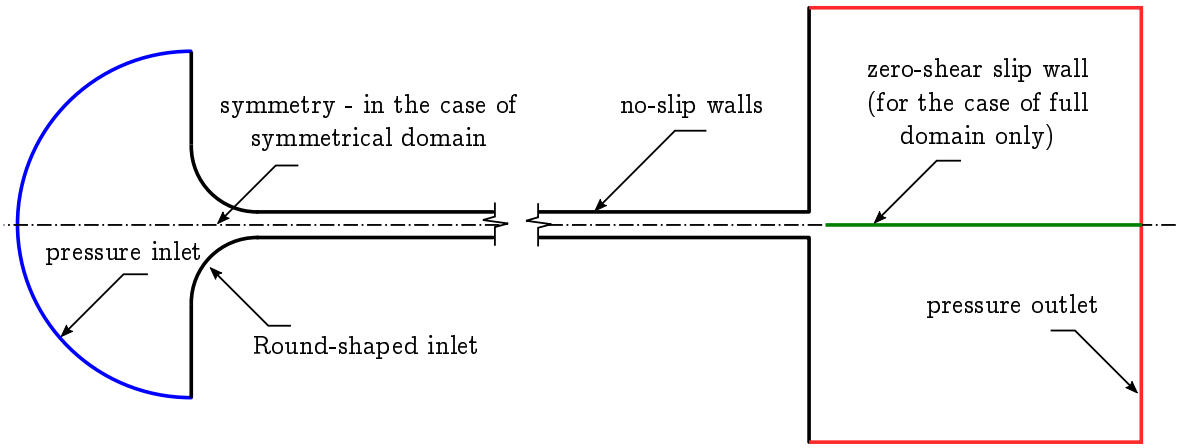

Figure 17: *Scheme of the narrow channel computational domain.*

6.4 Numerical Simulation of the Narrow Channel

Numerical simulations of the narrow channel aim to choose the most appropriate numerical model and to obtain data to complement experimental results. As the flow regime is of particular interest in this study, a number of turbulence models was tested. In addition to already mentioned k $-\omega$ SST, EARSM $-\omega$ and SST – Transitional models, the $k-kl-\omega$ and $\gamma - Re_{\theta_t}$ models were also tested for some of the cases.

6.4.1 Computational Domain and Boundary Conditions

Two dimensional computational domain of narrow channels is similar to that of calibration channel. Except the overall size of the domain, the main difference is the shape of the inlet part which is of the quarter circle shape. Figure 17 shows a scheme of the domain with marked boundary conditions.

Since boundary conditions varies slightly across specific turbulence models, the list below summarise all variations of boundary conditions used for the narrow channel CFD investigation.

- Pressure inlet
  - Total pressure; $p_0 = 101325\,\mathrm{Pa}$
  - Total temperature; $T_0 = 300\,\mathrm{K}$
  - Turbulence intensity; $Tu = 1.3\,\%$
  - Eddy viscosity ratio (Ratio of the eddy viscosity and molecular viscosity); $\frac{\mu_t}{\mu} = 10$
  - Intermittency; $\gamma = 1$; (For Transitional SST and $\gamma - Re_{\theta_t}$ models)

  - Laminar kinetic energy; $kl = 1{\cdot}10^{-6}\,\mathrm{m}^2{\cdot}\mathrm{s}^{-2}$; (For $k - kl - \omega$ model only)

- Pressure outlet
  - Static pressure according to the desired pressure ratio π
  - Other quantities extrapolated from flow field

- Walls
  - Zero velocity components; $u_i = 0$
  - Zero heat flux through the wall

- Symmetry
  - Zero normal components of all quantities

6.4.2 Computational Mesh

Although the problem is symmetric, some of the computations were performed for the full mesh such as in the case of calibration channel computations. In the case of full domain, similar stability issues as in the case of calibration channel arose, therefore, the same measure of infinitely thin inviscid wall located in the axis behind the channel exit was adopted. Since the results of the full domain computations were well comparable to that using a symmetric mesh, the majority of computations were carried out as symmetric to spare computational time. The view of the mesh for the narrow channel of the height of 2 mm is pictured in Figure 18. Details show the inlet part of the channel with triangular cells and the outlet part of the channel where the hanging nodes were used to coarsen the mesh in the plenum region. Number of cells depends on the channel height h and varies from 119 936 for $h = 0.5$ mm to 154 022 for $h = 4$ mm and symmetric domain.

As in the case of calibration channel, the grid convergence study was also performed using two finer meshes. The details of the used method and its results are described in the following subsection.

6.5 Grid Refinement Study

Similarly as it is important to evaluate measurement uncertainties in experiment it is a good practice to assess the mesh dependency of the results in CFD. Therefore, the refinement study was carried out according the methodology of Roache [35] [34]. The objective was to evaluate whether the coarse mesh intended for use in most of the computations is sufficient. For both calibration and narrow channel meshes, two

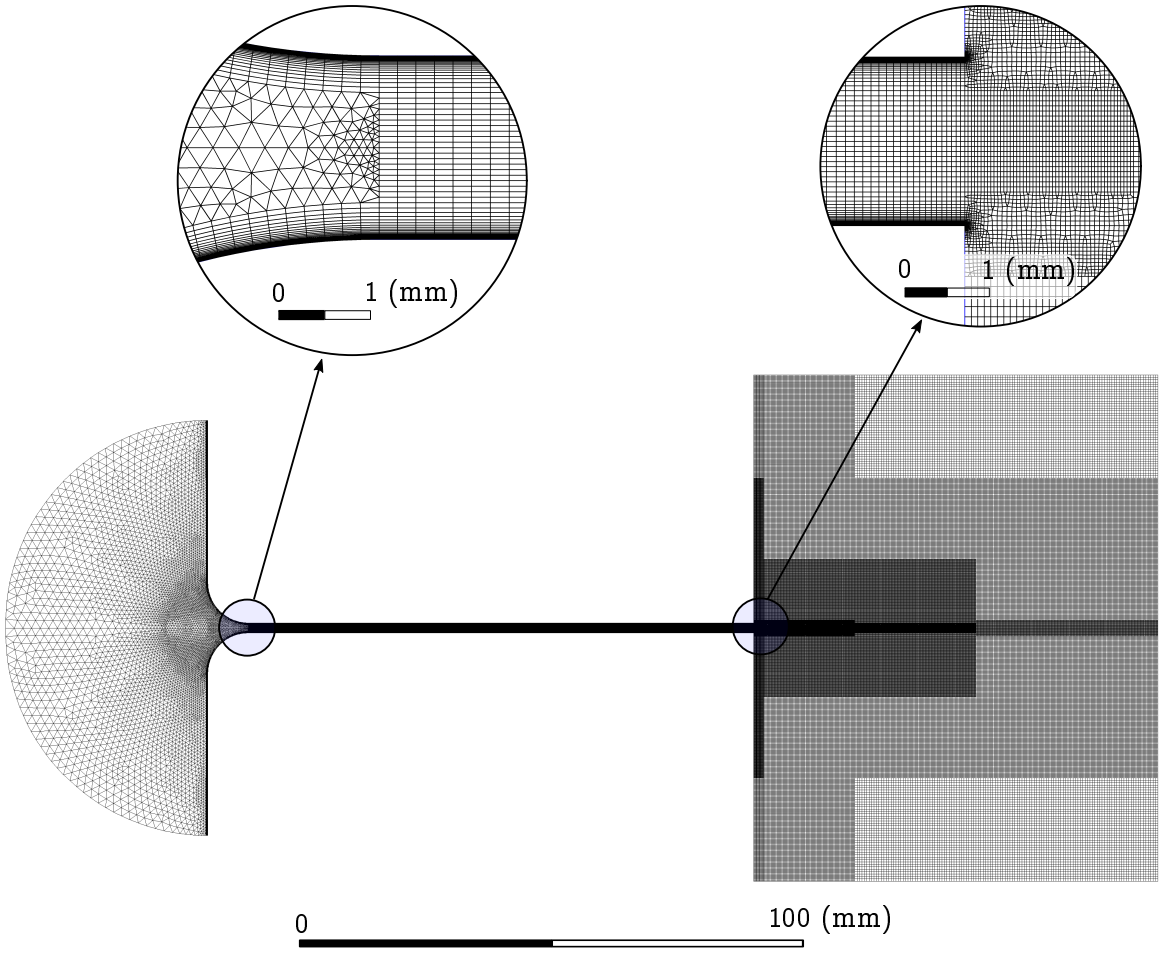

Figure 18: *Computational mesh of the narrow channel (for the case of the height $h = 2\,\mathrm{mm}$) including details of the channel inlet part and coarsening in the plenum region using hanging nodes.*

Table 4: Number of cells of meshes used for the CFD computations and for the estimation of numerical error given by spatial discretization.

	Number of grid cells N	
mesh	narrow channel	calibration channel
coarse	259944	178218
medium	364243	265726
fine	509684	398589

more meshes denoted as *medium* and *fine* were generated, each with approximately 1.2 times more grid cells than the coarser one. Table 4 shows the number of cells for each mesh and case.

Since there was a large number of combinations of regimes and geometries in the case of narrow channels, the grid refinement study was performed for k $-\omega$ SST turbulence model, 2 mm gap and pressure ratio $\pi = 0.3$. Pressure ratio $\pi = 0.3$ was chosen since this regime features most complex flow structures at the exit plenum region from all the examined regimes, therefore, it might be assumed that for larger pressure ratios the convergence would be comparable or even better. In the case of the calibration channel, the EARSM $-\omega$ turbulence model was used for the regime of the pressure ratio $\pi = 0.3$ for the same reason as in the case of narrow channels.

The method used is based on the evaluation of the Grid Convergence Index (GCI) defined as

$$GCI = F_s|E|, \tag{35}$$

where F_s is safety factor and E is the Richardson error estimator, which can be evaluated either for coarse mesh as

$$E^{\text{coarse}} = \frac{r^p \epsilon}{1 - r^p} \tag{36}$$

or for a fine mesh as

$$E^{\text{fine}} = \frac{\epsilon}{1 - r^p}. \tag{37}$$

In this study the coarse mesh was intended for use in most of the computations, therefore, the former definition was used. Variables p and r in equations above stands for a formal order of accuracy of the used method and the refinement factor between the coarse and fine grid respectively. The order of accuracy was in our case $p = 2$ and the effective refinement factor, which can be calculated for 2D meshes as $r = \sqrt{\frac{N_{\text{fine}}}{N_{\text{coarse}}}}$, where N is a number of cells, was approximately $r = 1.2$. Then, ϵ is

Table 5: *Results of grid refinement study in terms of grid convergence index GCI (%). GCI_{32} indicates value of grid convergence index evaluated from coarse and medium mesh and GCI_{21} from medium and fine mesh.*

	narrow channel	calibration channel
GCI_{32} (%)	0.345	0.272
GCI_{21} (%)	0.218	0.094

the relative error of the solution obtained using coarse and fine meshes $\epsilon = \frac{f_2 - f_1}{f_1}$. Finally, the recommended conservative value of the safety factor of $F_s = 3$ [34], which can be interpreted as coverage factor in measurement uncertainty evaluation, was used. As a solution parameter f, the integral value of mass flow rate in the cross section in the 95 % of the channel length was chosen as the most convenient variable to asses.

Table 5 summarizes the obtained values of the GCI for both calibration and narrow channels. For each of the cases, three meshes (coarse, medium and fine) were used for the analysis. GCI_{32} then indicates value of grid convergence index evaluated from coarse and medium mesh and GCI_{21} from medium and fine mesh. For both cases, the coarse mesh GCI is approximately 0.3 % (for safety factor $F_s = 3$), which is well acceptable, therefore, even the coarse mesh should provide sufficient resolution for intended computations.

7 Hot-Film Sensor Calibration Procedure

7.1 Introduction

There are several calibration procedures of hot-film sensors reported in literature. All of the procedures builds upon the King's law, which is widely used in hot-wire anemometry and provides a basic empirical approximation between the convective heat loss of a hot-wire and the flow velocity as

$$V^2 = A + Bu^m, \tag{38}$$

where A, B and m are calibration constants, V is the voltage measured on the bridge of a CTA anemometer and u is the flow velocity [23]. In the case of hot-films, the King's law given by equation (38) can be rebuild to the form

$$V^2 = A + B\,\tau_w^{\frac{1}{3}}, \tag{39}$$

where τ_w is the wall shear stress defined as

$$\tau_w = \mu \frac{\mathrm{d}u}{\mathrm{d}y}. \tag{40}$$

The calibration then comprises of obtaining of the calibration constants. Some of the procedures are based on the exact quantification of all means of heat transfer from the hot-film, so as the total heat flux can be adjusted and the value net of heat fluxes other than convection to flow can be determined and used for the calculation of the Nusselt number Nu, and subsequently the wall shear stress τ_w. These methods necessitate a correct modelling of all factors having an effect on the heat transfer from the hot-film operated in the constant temperature mode. These include for instance the heat conduction to hot-film probe substrate, to ambient flow, and to near wall if there is any present. In these methods the sensitivity of thermal sensor voltage needs to be determined a priori. However, the sensitivity determination is usually made using analytical corrections which are mostly derived from those for hot-wire sensors. Such corrections are unfortunately valid only for small temperature ranges as the method described and reported by Jonáš in [24]. Since the conduction from the hot-film to the probe substrate dominates the convection to flow, the technique of simple correction represented by equation

$$V^2 = A + Bu^m \left(T_{\mathrm{sensor}} - T_{\mathrm{fluid}}\right), \tag{41}$$

widely used for wires, which have large length to diameter ratio compared to hot-films, can not be successfully applied for hot-films as reported by Thünker et al in

[36]. Therefore, a correct determination of the sensitivity of the sensor to ambient temperature variations is the key issue, which makes this kind of methods difficult to carry out. Other class of methods is based on a semi-empirical calibration, which should eliminate the disadvantages described before at the price of longer measurement times and usage limited for similar flows and the same sensor as was used for the calibration measurements.

After several attempts the semi-empirical calibration method of Davies described in [29] was chosen as the most suitable one for the use in our investigation. This method is based on the continuous measurement until the temperature equilibrium is reached, which took approximately 20 minutes in our case, and on the subsequent measurement immediately after switching off the airflow giving zero flow voltage V_0. Using the zero flow voltage, the temperature variation effects can be successfully eliminated for thermal equilibrium flows. The relation for the wall shear stress is then given by equation

$$\tau_w = \left[\frac{V^2 - V_0^2}{C_1(T_s - T_\infty)}\right]^3 + C_2\frac{\mathrm{d}p}{\mathrm{d}x}, \tag{42}$$

where C_1 and C_2 are calibration constants, incorporating the physical properties of the fluid and the dimensions of the sensor. To obtain the calibration constants, the set of measurements in the calibration facility using the sublayer fence probe and hot-film sensor was carried out. The obtained data were used for the determination of the calibration constants using optimization script written in MATLAB programming environment. The following sections deal with the optimization procedure used for the determination of the hot-film probe calibration constants and the calibration measurements on the calibration channel together with the problems which had to be solved before the actual calibration.

7.2 Initial Measurements

Initial measurements on the calibration channel revealed flow instabilities in the entrance part of the channel possibly affecting downstream flow. The instabilities were measured by yet uncalibrated hot-film probe and evaluated using the raw signal analysis as described in 5.7.2. To tackle this issue and obtain stable turbulent flow, the turbulator tapes were installed at the channel inlet. The turbulator tapes were of the *Zig-Zag* type 9 mm wide and 0.5 mm in heigh, which are commercially available and intended for use in general aviation to force the boundary layer transition upstream the control surfaces of the sailplains or on its wings to avoid laminar separation. After this modification, the instabilities ceased to exist as apparent from Figure 19, which shows the comparison of the hot-film probe signal in the location

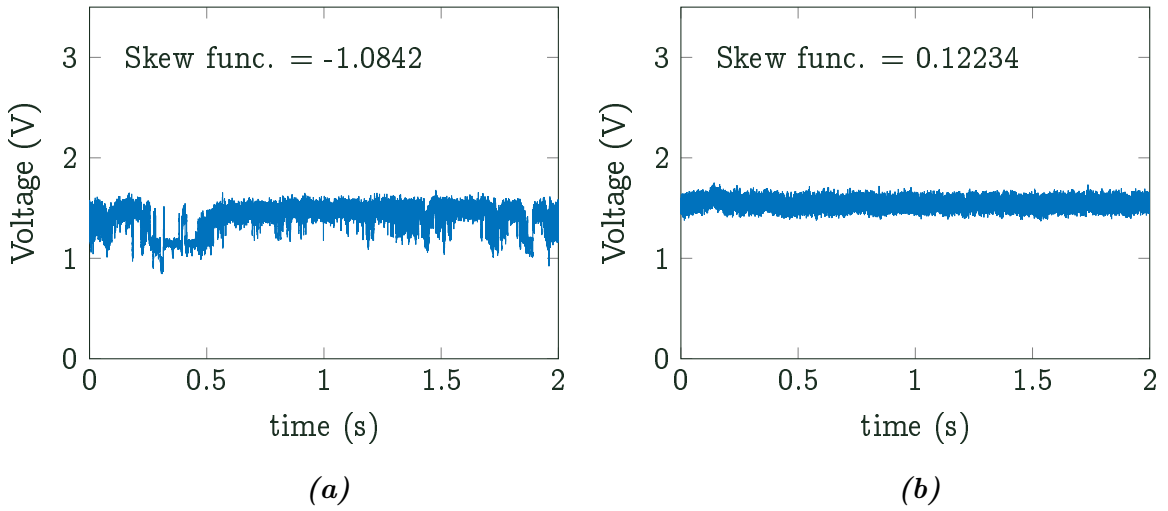

(a) *(b)*

Figure 19: *Hot-film probe signal (CTA bridge voltage and its Skew Function* (28)*) measured at the location* $x = 176\,\text{mm}$ *without the turbulator tape at the inlet (a) and with the turbulator tape (b).*

$x = 176\,\text{mm}$ (the closest measuring position downstream of the inlet) without (19a) and with (19b) installed turbulator tapes. As already discussed in Section 5.7.2 the value of the Skew-function (Equation (28)) around zero indicates fully developed flow (either laminar or turbulent) while negative or positive values indicate transitional flow or flow affected by shock waves or separation [27], [28]. It follows from the signal analysis shown in Figure 19 that the flow in calibration channel equipped with the turbulator tapes at the inlet is most likely turbulent starting at least from the location of the first measuring plug ($x = 176\,\text{mm}$). Another issue is, however, the entrance length which, according to the literature [37], might reach the distance of even a few hundred times the characteristic dimension that is 10 mm in this case. Since the issue whether the flow in the calibration channel is turbulent and fully developed or not is vital for the hot-film calibration, it was decided to further examine the flow development using pneumatic methods and to support the results with CFD computations.

The flow development in calibration channel was first examined by measuring the total pressure distribution along the channel axis and later by measuring of the total pressure profiles in seven locations using traversing device described in Section 5.4. The measurement of the total pressure distribution along the channel axis was carried out for the channel with and without the turbulator while the total pressure profiles were measured for the case with the turbulator tape at the inlet only. The measurements were conducted for pressure ratios $\pi = 0.8$, 0.6 and 0.3 which should cover vast range of regimes from low subsonic to aerodynamically choked.

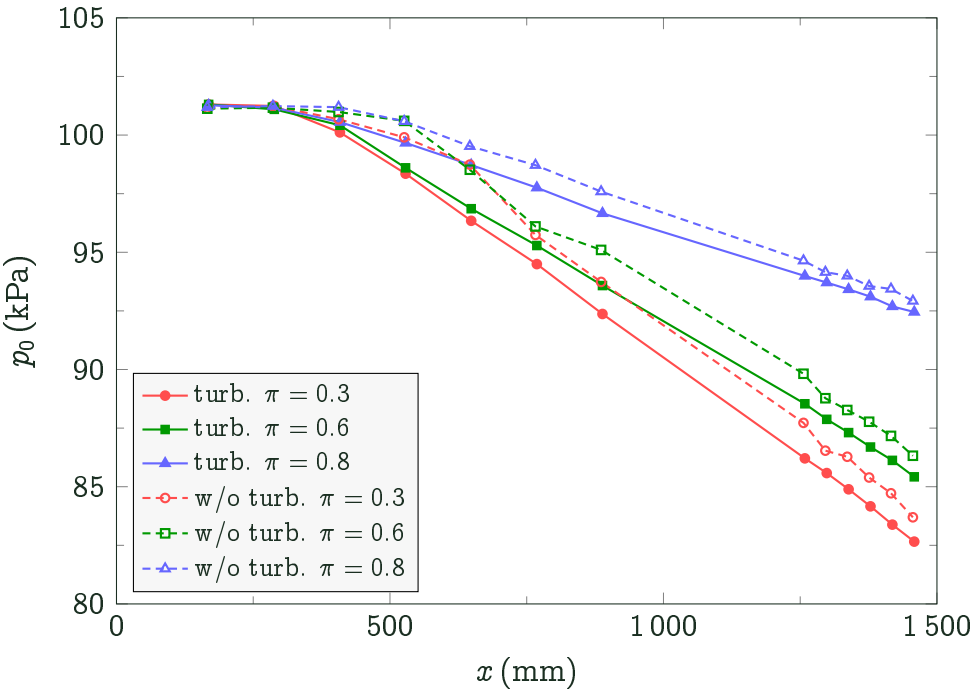

Figure 20: *Distribution of the total pressure measured in the axis of the calibration channel equipped with and without turbulator tape at the channel inlet for various pressure ratios π.*

The distributions of the total pressure in the channel axis are shown in Figure 20. It is apparent that the effect of the inlet turbulator tapes is significant for both the entrance length and further flow development. Without the turbulator tapes (dashed lines) the total pressure drop indicating the vanishing of the inviscid flow core occurred at the location approximately $x = 500$ mm. The exact location was, however, strongly influenced by the inlet fluctuations, the presence of which was apparent even from the pressure data sampled by the NetScanner pressure transducer, which in this case exhibits increased measurement uncertainties. When using the turbulator tapes, the total pressure drop was measured from the location $x = 300$ mm, which accounts for a distance of 30 channel heights, and the pressure data measured along the rest of the channel length showed lower fluctuations than in the case without the turbulators.

To support the results obtained from the total pressure measurements in the channel axis, the total pressure profiles were measured for a number of locations. The total pressure profiles were measured using the traversing device described in Section 5.4 and the measured values of total pressure were compensated for the wall proximity effects as set out therein. Figures 21, 22 and 23 show the measured total pressure profiles for pressure ratios $\pi = 0.3$, 0.6 and 0.8 respectively. The graphs show also the profiles obtained from the CFD computations using k-ω SST and EARMS-ω

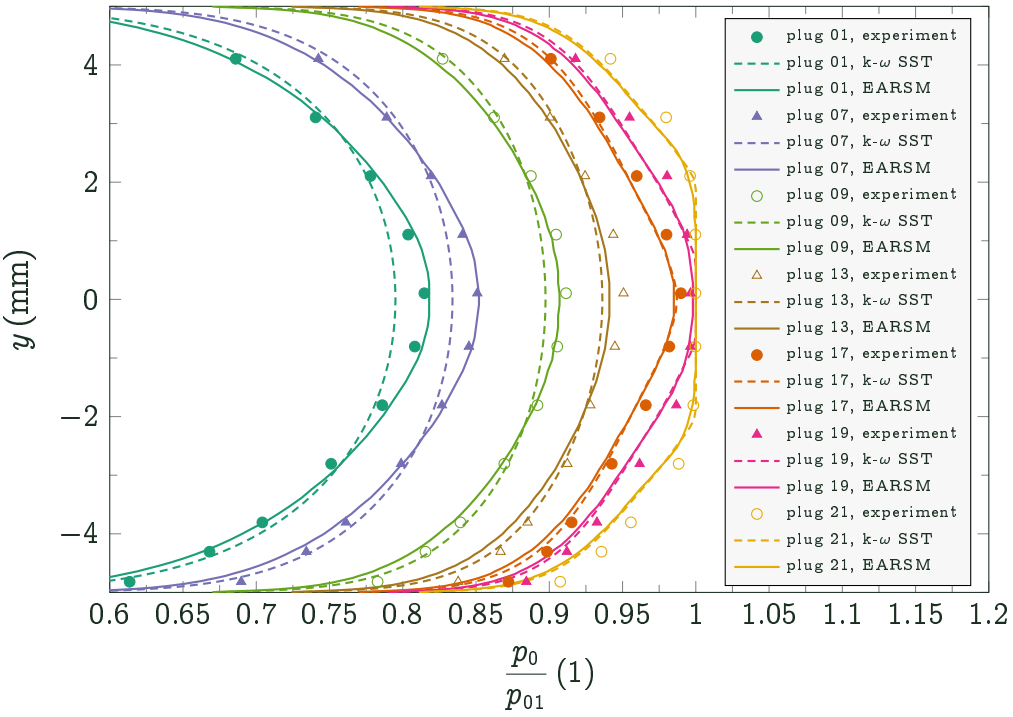

Figure 21: *Total pressure profiles measured across the calibration channel in various locations along the channel axis for the pressure ratio* $\pi = 0.3$.

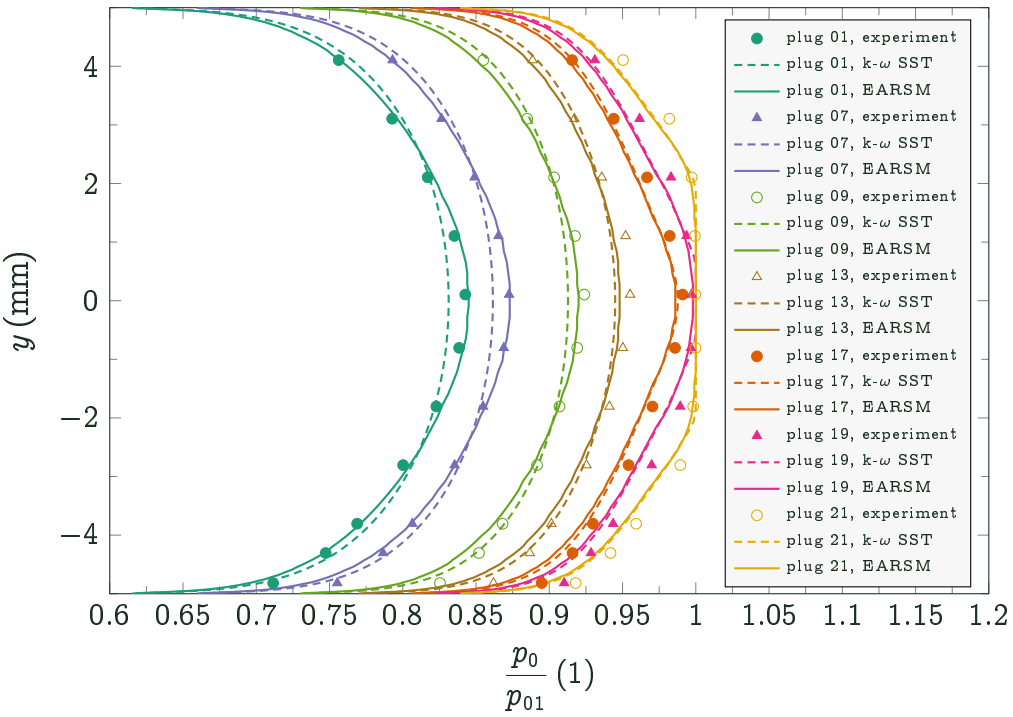

Figure 22: *Total pressure profiles measured across the calibration channel in various locations along the channel axis for the pressure ratio* $\pi = 0.6$.

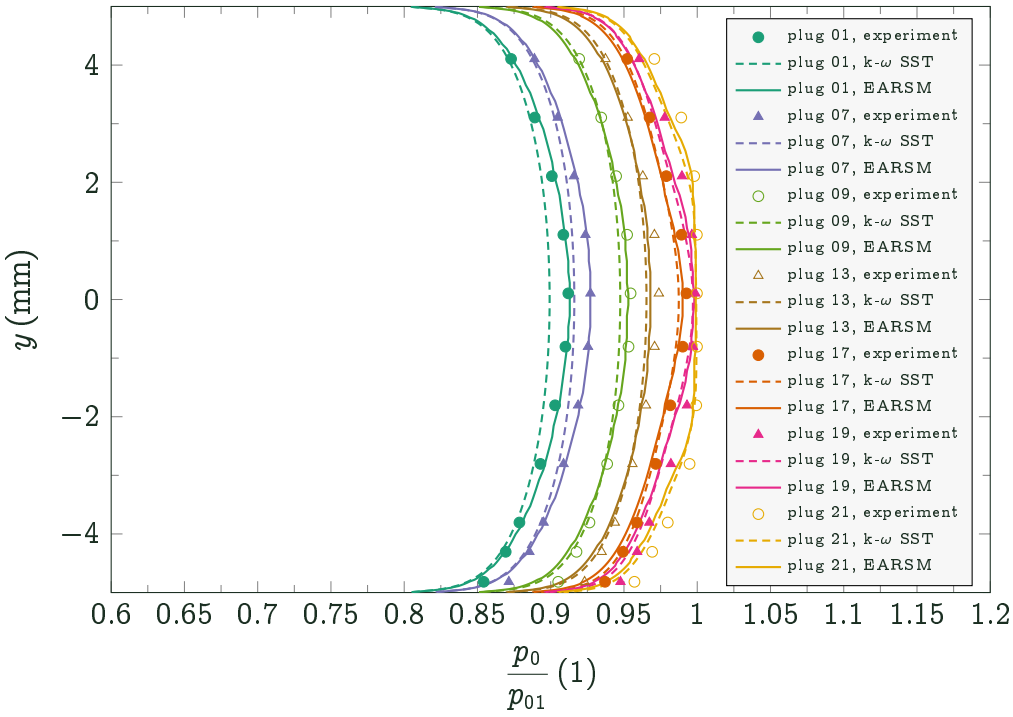

Figure 23: *Total pressure profiles measured across the calibration channel in various locations along the channel axis for the pressure ratio* $\pi = 0.8$.

turbulence models. The obtained total pressure profiles revealed that even at the locations where the total pressure at the channel axis starts to drop, the actual profiles seem not to be fully developed. Total pressure profile data suggests that the flow in the calibration facility equipped with the turbulators at the entrance can be considered to be turbulent and fully developed approximately from the location of the plug No. 13, which is located at $x = 656$ mm downstream of the inlet.

The results of the numerical simulations are shown in Figures 24 and 25. It is apparent that fully turbulent models show good agreement with the experiments. EARMS-ω model appears to well predict both distribution of the total and static pressure as well as the total pressure profiles (Figures 21, 22 and 23). Static pressure distribution computed using k-ω SST model is comparable to that of EARMS-ω, however, the total pressure distributions and profiles of total pressure differ from the measured data. The transitional model performed worst. The data obtained using this model did not surprisingly match even the experimental data obtained on the channel without the turbulators. This might be accounted for the inlet shaping, which, despite its smooth bernoulli lemniscate shape, might induce transition due to separation on the edge of the inlet. Nevertheless, both static pressure and total pressure distributions obtained using the transitional model differ significantly from what might be expected in the channel and from the measured data. It turned out that the use of more computationally demanding EARSM model can be highly

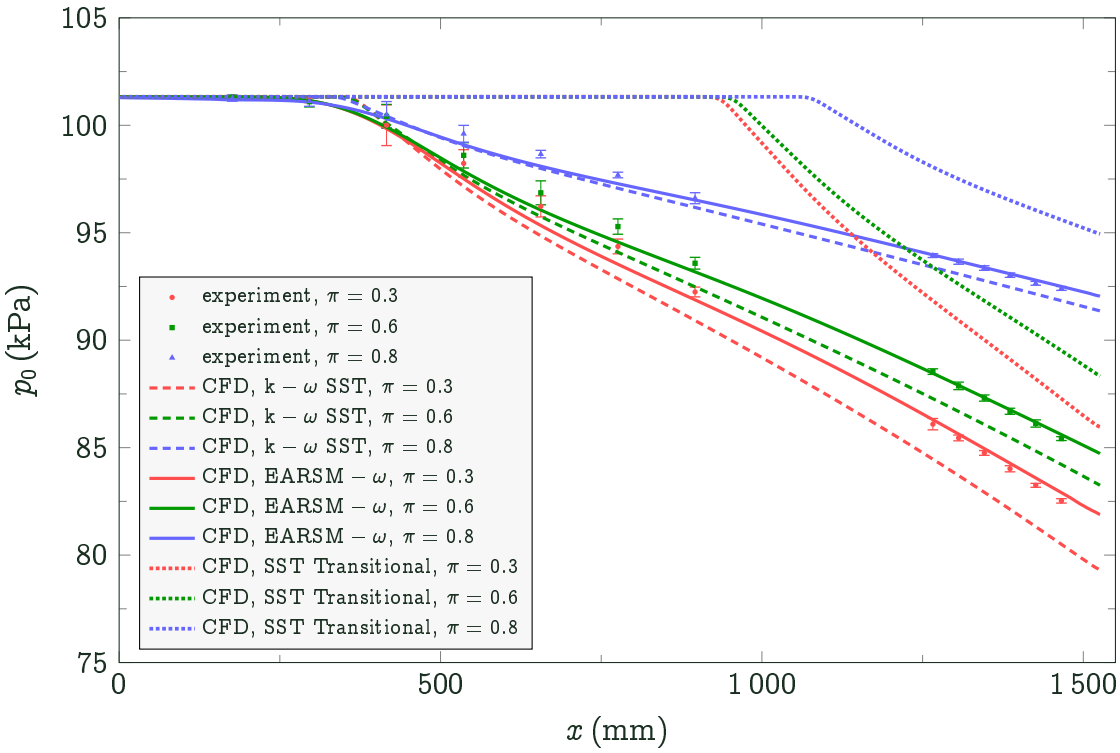

Figure 24: *Comparison of measured total pressure data including error-bars of the measurement uncertainties and CFD data obtained using various turbulence models.*

recommended in such cases. The data obtained using this model were later used for the recalibration of the fence probe and subsequently for the calibration of the hot-film probe.

7.3 Sublayer Fence Probe Recalibration

Prior to the final calibration of the hot-film probe we decided to verify the original calibration of the sublayer fence probe since the original calibration represented by equation (23) was carried out for incompressible flow only. The original calibration was then compared with the data obtained using Fluent CFD code and EARMS-ω turbulence model, which turned out to perform best amongst all the tested models in prediction of the total and static pressure distributions in the calibration channel as discussed in the foregoing section. The comparison of the wall shear stress values obtained from the original calibration with the CFD data is shown in Figure 26. As can be observed, there is a significant offset of the fence probe data with respect to the CFD results. Nevertheless, the overall trends of the wall shear stress were well captured over the full length of the calibration channel. The offset was most possibly caused by the inaccuracy of the measurement of the fence height. To cope with this discrepancy, the new calibration was made using the CFD data, which

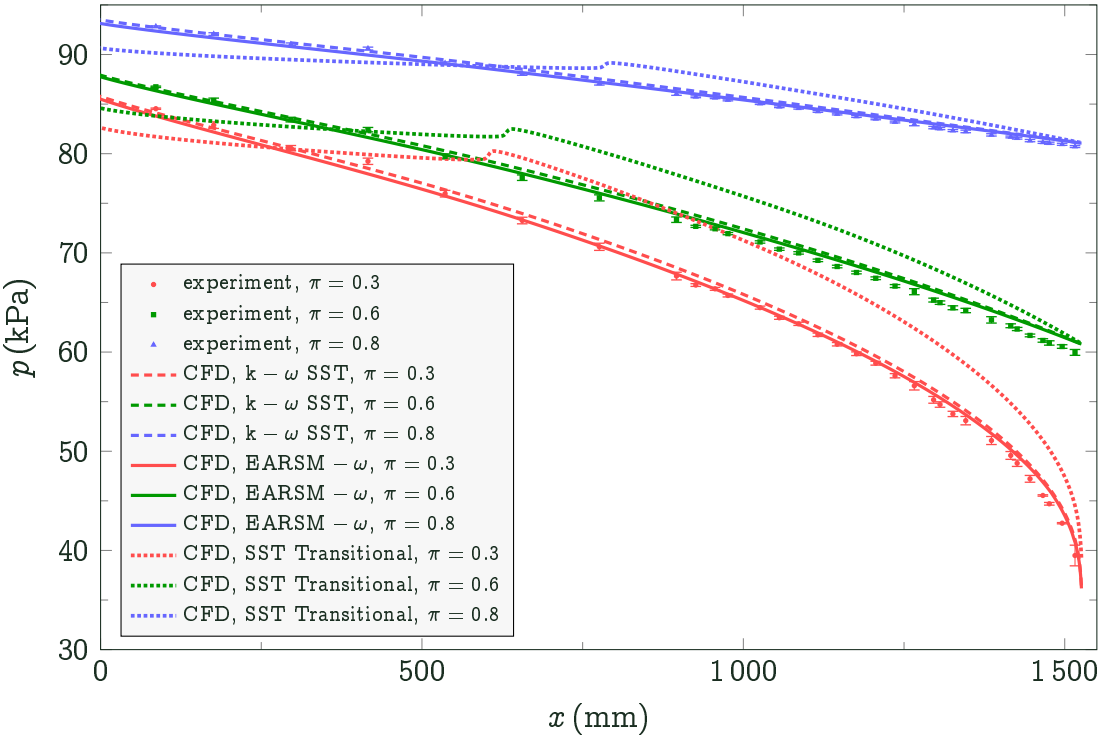

Figure 25: *Comparison of measured static pressure data including error-bars of the measurement uncertainties and CFD data obtained using various turbulence models.*

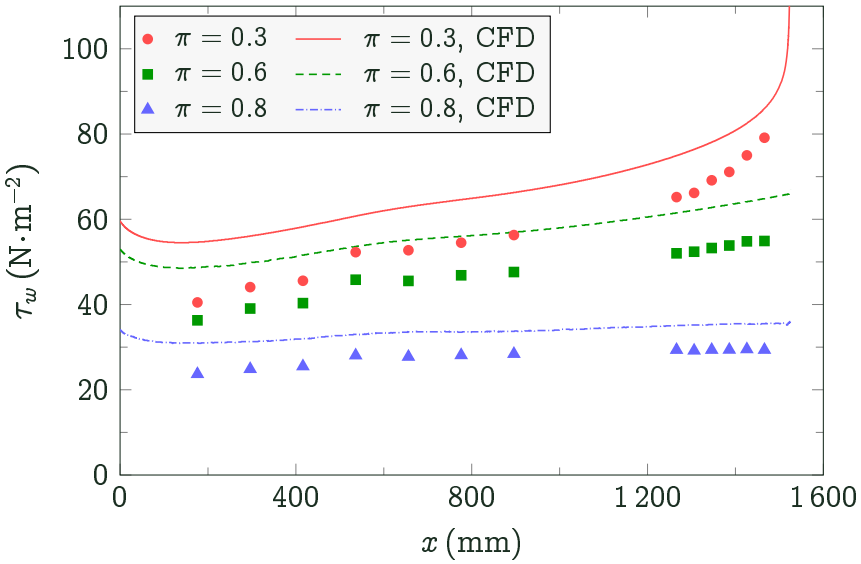

Figure 26: *Wall shear stress τ_w along the calibration channel measured by the sublayer fence probe for various pressure ratios π using the original calibration together with the CFD data obtained using EARMS-ω turbulence model.*

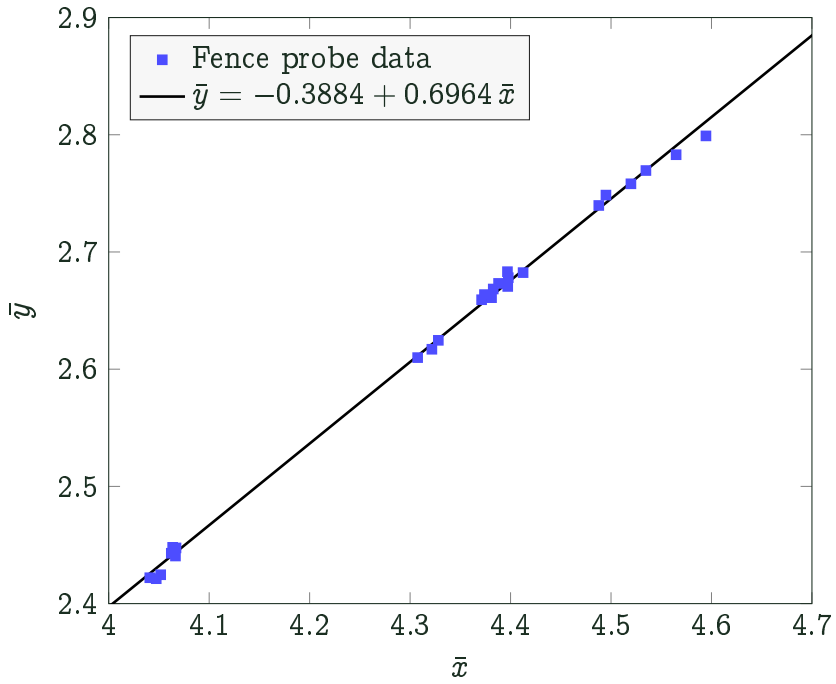

Figure 27: *New calibration curve of the fence probe made using the CFD computations data.*

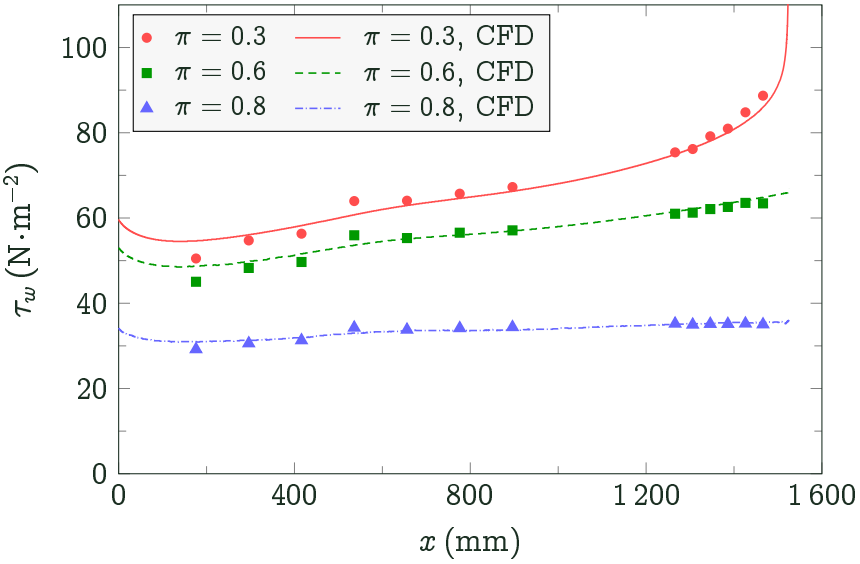

Figure 28: *Wall shear stress τ_w along the calibration channel measured by the sublayer fence probe for various pressure ratios π using the new calibration together with the CFD data obtained using EARMS-ω turbulence model.*

were considered to be reliable since the measured velocity profiles, determining for the values of the wall shear stress, agreed well with the computations in the region of fully developed flow. The new calibration was made in the same way as the original one by expressing the terms $\bar{x}$ and $\bar{y}$ given in equation (24) and searching for a linear interpolation that best fits the given values of $\bar{x}$ and $\bar{y}$. The new calibration constants were find out giving the new calibration relation

$$\bar{y} = a + b\bar{x} = -0.3884 + 0.6964\,\bar{x}, \tag{43}$$

which was used for the hot-film calibration and could be used for further measurements with the same sublayer fence probe. The graph in Figure 27 pictures the calibration curve and Figure 28 the wall shear stress obtained using the new calibration compared to CFD data. It can be concluded that the calibration coefficient $b \approx 0.7$ is in good agreement with the original calibration and the only change is in the constant $a = -0.3884$, which can be most likely accounted for inaccurately measured fence height $h_f = 0.05\,\text{mm}$, which was beyond the possibilities of available equipment. As a consequence, the hot-film probe calibration described in the following section, was eventually conducted using the wall shear stress data obtained from the new sublayer fence probe calibration, which is based upon the CFD computations using EARMS-ω turbulence model.

7.4 Hot-Film Probe Calibration Measurements

For the calibration measurements, the same driving pressure ratios of the settling chamber pressure to inlet pressure $\pi = \dfrac{p_b}{p_{01}} = 0.3$; 0.6 and 0.8 as in the case of initial measurements were chosen. Such range of pressure ratios should cover sufficiently large range of the wall shear stress values in the calibration channel. For each of these pressure ratios, the values of the wall shear stress were measured along the channel axis using the sublayer fence probe together with the distribution of the static pressure. The total pressure data could not be measured simultaneously since the fence probe occupied the measuring plug, however, these data had already been measured for the same pressure ratios before. The pneumatic measurements were performed several times to allow assessment of the measurement uncertainties as described in Section 5.8. Then, the measurements were conducted operating the hot-film probe in the calibration channel for the same regimes given by the driving pressure ratios, and thus, the same wall shear stress distributions, which enabled us to determine the link between the voltage across the hot-film sensor V and the aerodynamic wall shear stress τ_w using the semi-empirical calibration method of Davies.

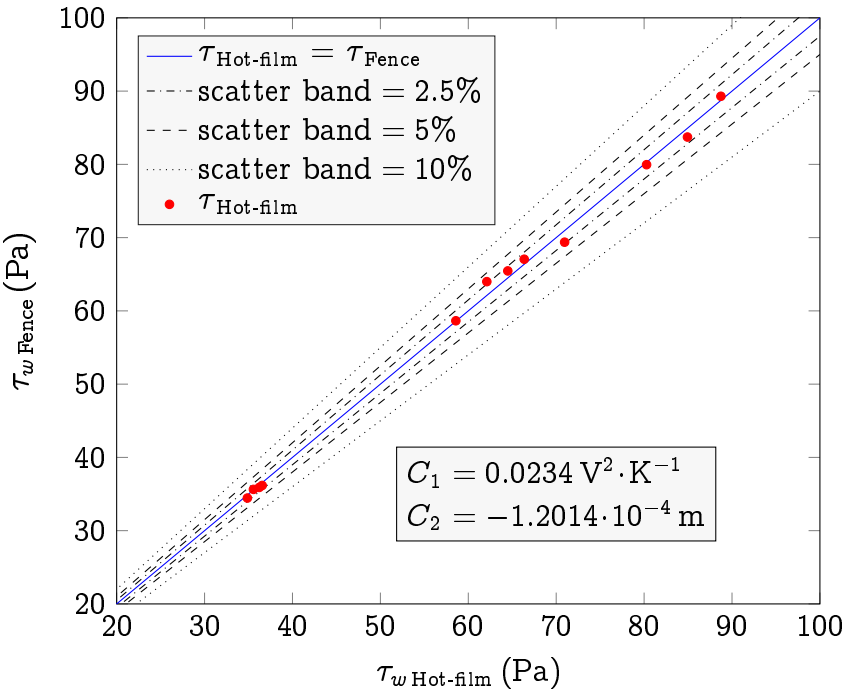

Figure 29: *Calibration curve of the hot-film probe with the marked uncertainty bands of* 2.5, 5 *and* 10%.

To obtain the calibration constants C_1 and C_2 for the relation (42), the optimisation algorithm based on the minimization of an objective function was written in MATLAB. The *objective function* was of the following form

$$f(V,\, V_0,\, p,\, T_s,\, T_\infty) = \sqrt{\left\{\left[\frac{V^2 - V_0^2}{C_1(T_s - T_\infty)}\right]^3 + C_2\frac{\mathrm{d}p}{\mathrm{d}x} - \tau_{w\,\text{Fence}}\right\}^2}. \tag{44}$$

The optimization algorithm (Nelder-Mead simplex direct search) then searched for the combination of the calibration constants so as the objective function is minimized in the least squares sense for the given test data consisting of the vector of wall shear stress measured by the sublayer fence probe and the corresponding vector of the voltage $V^2 - V_0^2$, where V is the voltage measured on the hot-film sensor after the temperature equilibrium was reached for a given flow regime and V_0 is the sensor voltage measured immediately after the switching off the flow. Using this method, we obtained the calibration constants $C_1 = 0.0234\,\text{V}^2\cdot\text{K}^{-1}$ and $C_2 = -1.2014\cdot10^{-4}\,\text{m}$. Figure 29 shows the comparison between the values obtained using the sublayer fence probe and the hot-film calibrated using the determined constants. It can be seen that the wall shear stress data fall within the scatter band of $\pm2.5\%$ accuracy. It should be noted that such calibration can only be used for the same sensor operated under the same overheat temperature in the air and if the sensor is mounted in the material of the same thermal conductivity as was used during the calibration.

8 Narrow Channel Measurements

8.1 Introduction

Preceding sections gave details of the measurement techniques, calibration of the hot-film probe, and CFD computations to be used during the present investigation. In this section, the subsequent optical, pneumatic and hot-film measurements in the narrow channels are presented with the aim to complete the set of experimental data required to satisfactorily analyse the flow and answer the research questions outlined in *Aims of the Work* section.

To effectively use the available methods, the narrow channel measurements were conducted in three stages. During the first stage, the optical measurements of the channel of the heigh of 2 mm was carried out for several pressure ratios and for each of three surface finishes. Other channel heights were not measured in this stage due to limitation of the optical method, which requires sufficient channel height to prevent light reflections from channel walls that make measurements impossible. These measurements are continuing of the previous investigation conducted in Nový Knín laboratory [A5][A2][A6][A3], but now improved by the use of the new high resolution camera and improved construction of narrow channel facility providing higher accuracy of the channel height setting.

The second stage comprises of measurements of all surface roughness variants in channels of the height of 0.5; 1 and 2 mm. Each of these combinations were measured for pressure ratios 0.3; 0.6 and 0.8. Since the number of measured regimes was too large for time demanding quantitative measurements using hot-film probe, the regimes were first investigated qualitatively without the need for long continuous measurement runs necessary to achieve temperature equilibrium. To reduce number of measurements and still obtain reasonable data about the flow development along the channel, the hot-film probe was placed in turn in measuring locations 1 (the most upstream one), 3 (in the middle) and 5 (the most downstream one), thus skipping locations number 2 and 3. Besides that, the pneumatic measurements using static pressure taps and the measurements of the total pressure were carried out during this stage.

The third stage included quantitative measurement using the hot film probe at the regimes chosen based on the interim analysis of the first stage measurements. This stage was primarily intended to measure shear stress in the channel and its near exit region and to complete measurements from the stage two.

Each of these mentioned stages is further described in following subsections while the analysis and results of the measurements are presented in section 9.

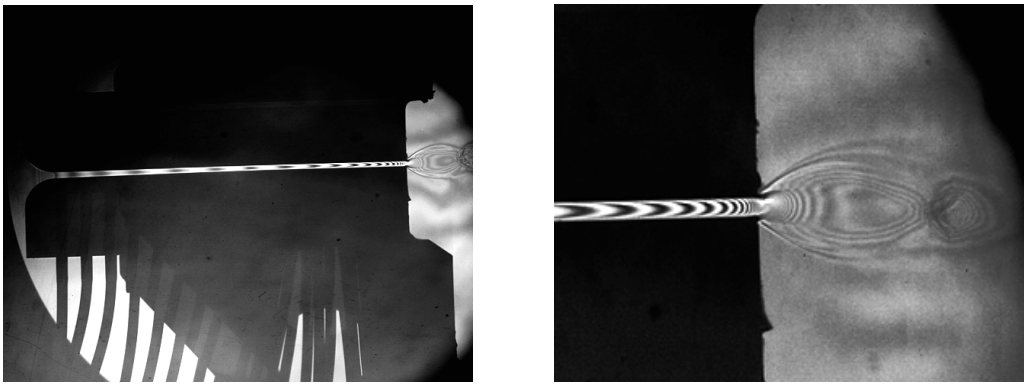

(a) *(b)*

Figure 30: *Example of the interferogram taken with the lens setting capturing the whole channel (a), and the one capturing the datail of the exit region (b).*

8.2 Stage 1 - Optical Measurements

Optical measurements were intended for flow regimes defined by pressure ratio $\pi =$ 0.12, 0.3, 0.6 and 0.8. Due to confusion of the pressure tube measuring the ambient pressure and the one measuring the pressure at the first pressure tap in the channel, the resulting regimes differ slightly. After the compensation for this mistake, the actual measured regimes were $\pi = 0.088$, 0.22, 0.44 and 0.61.

The interferograms were taken using two sets of lenses with different focal length. The first set provides the field of view of the whole channel while the other one was focused on the exit area only. Figure 30 shows raw images comparing the two used focal lengths. The raw images were later edited to allow automatic evaluation using a MATLAB script made for this purpose. Each of the regimes was measured multiple times with slightly different focusing point. Selection of the interferograms of all measured combinations are listed in Appendix D.

8.3 Stage 2 - Pneumatic and Qualitative Hot-Film Probe Measurements

Stage 2 experiments were intended to gather relatively large set of data for various combinations of regimes. Since only one hot-film probe was available, the hot-film probe investigation was limited to only three measuring locations of five available during this stage. The hot-film probe was operated as described in subsection 5.7. Each regime was carefully set by regulation valve for desired pressure ratio. Prior to the sampling, a period of a few seconds was necessary for flow parameters to settle to steady state. The sampling period was set to 2 seconds and for each regime multiple samples were recorded.

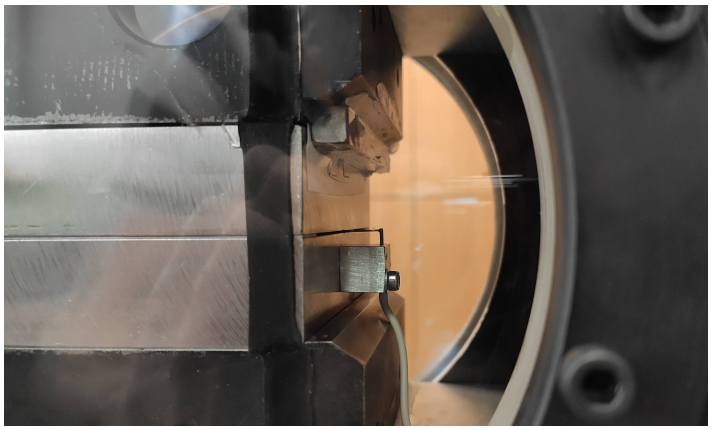

Figure 31: Pitot probe positioned at the channel midheight (channel of the height 0.5 mm).

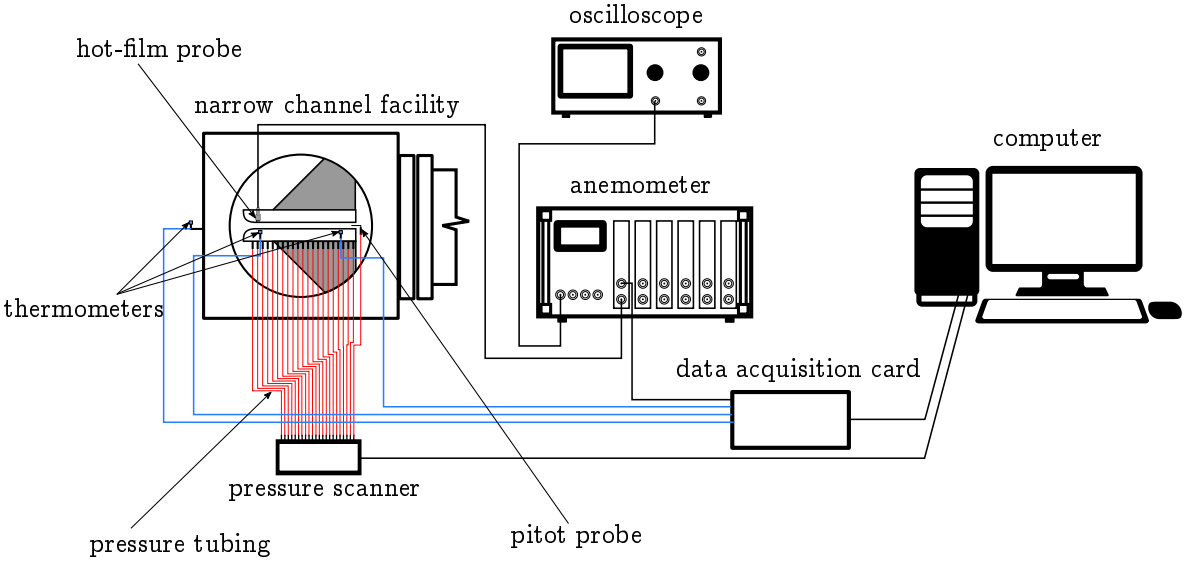

Figure 32: Diagram of the measuring chain.

During each measuring run, the pressure data were also periodically collected including the total pressure from the pitot probe located 2 mm upstream the channel exit plane in the midchannel. The pitot probe has an outer diameter of 0.5 mm and an inner diameter of 0.25 mm. Photo in Figure 31 shows the actual mounting of the pitot probe at the exit of the channel of the height 0.5 mm. Despite the first intention was to traverse the pitot probe across the channel height, only the midchannel measurements were accomplished. The reason was that the planned mounting of the traversing device was too far from the channel. This resulted in the necessity to have the pitot probe attached to long beam, which could not apparently provide desired stability for the probe that tends to oscillate during the measurements. A scheme of the measurement chain is depicted in Figure 32.

8.4 Stage 3 - Quantitative Hot-Film Probe Measurements

Since the quantitative measurements necessitate relatively long measurement runs to reach the temperature equilibrium of the channel walls, only two regimes were chosen for further investigations. The first chosen regime was specified by the channel height of 0.5 mm and pressure ratio $\pi = 0.5$ and the second regime by the channel heigh of 2 mm and pressure ratio $\pi = 0.6$. Either of these regimes were investigated for smooth walls and both roughness variants. The values of pressure ratio were limited by the use of new regulation valve, which was more convenient for regulation during the long measurement periods but on the other hand the maximal achievable pressure drop was limited due to smaller inner diameter of the valve bore. Other settings were the same as in the case of qualitative measurements, which is shown on the scheme in Figure 32. Unlike in the case of earlier qualitative measurements, all five possible hot film probe measurement locations were now employed in each regime.

During the measurement the temperature of the channel walls was continually measured to determine when the temperature leveled off and thus the thermal equilibrium was reached. This usually took from 15 to 20 minutes. After this period the hot film data were sampled. Immediately after data sampling, the flow was switched off using the fast acting gate valve and several other samples were taken during the shutting down period which took about 20 seconds. The data sampled after the switching off the flow were later used for temperature compensation with the aim to determine the wall shear stress τ_w using the calibration described in section 7. The static pressure distribution was also measured to obtain pressure gradient $\frac{\mathrm{d}p}{\mathrm{d}x}$ necessary for wall shear stress determination from equation (42).

Results of the measured data are presented in the following section together with thorough analyses to fulfil the aims of this work.

9 Results & Discussion

9.1 Flow analysis

As was introduced in section 1, the problem of identifying whether the flow in narrow channels of dimensions comparable with the investigated channels is laminar or turbulent is still a topical problem of fluid dynamics. This section provides thorough analysis of numerical simulations and of measured data including data obtained using the hot-film probe with the aims to shed more light on the nature of the flow in the narrow channels.

9.1.1 Results of the Pneumatic Measurements

The first available and easiest to process data were those measured using pneumatic methods, therefore, its analysis and comparison with the numerical simulations were also conducted first, resulting in following findings.

Graphs in Figures 33, 34 and 35 show the comparison of computed and measured distributions of the static pressure (normalized by the inlet total pressure p_{01}) along the channel for three channel heights and three different pressure ratios. It is apparent that closer to the channel inlet, the measured distributions falls approximately in between distributions computed using fully turbulent and transitional models. However, with increasing x-coordinate, the fully turbulent models seem to perform better, while there is almost no difference between k $-$ ω SST and EARSM-ω models in cases for which both these models were tested. Later on, the pneumatic measurements were completed with the measurements on the channels equipped with rough walls. The graphs presenting the comparison of the static pressure for smooth and rough walls are in the Appendix C. It can be observed that the cross-flow roughness shifts the distribution upwards with respect to the smooth wall. This difference is most apparent for the moderate pressure ratio $\pi = 0.6$ and increases towards the channel exit. The streamwise roughness on the other hand shifts the distributions lower with respect to the smooth wall case. This is most likely caused by increase of the effective cross-section of the channel, resulting in distributions which correspond to larger channel height than the nominal height measured using filler gauges. This effect apparently weakens as the ratio between the roughness and the channel height became smaller with increasing channel height, which results in almost no difference between the smooth wall and streamwise roughness in the case of the channel height $h = 2\,\mathrm{mm}$ (Figure C.56).

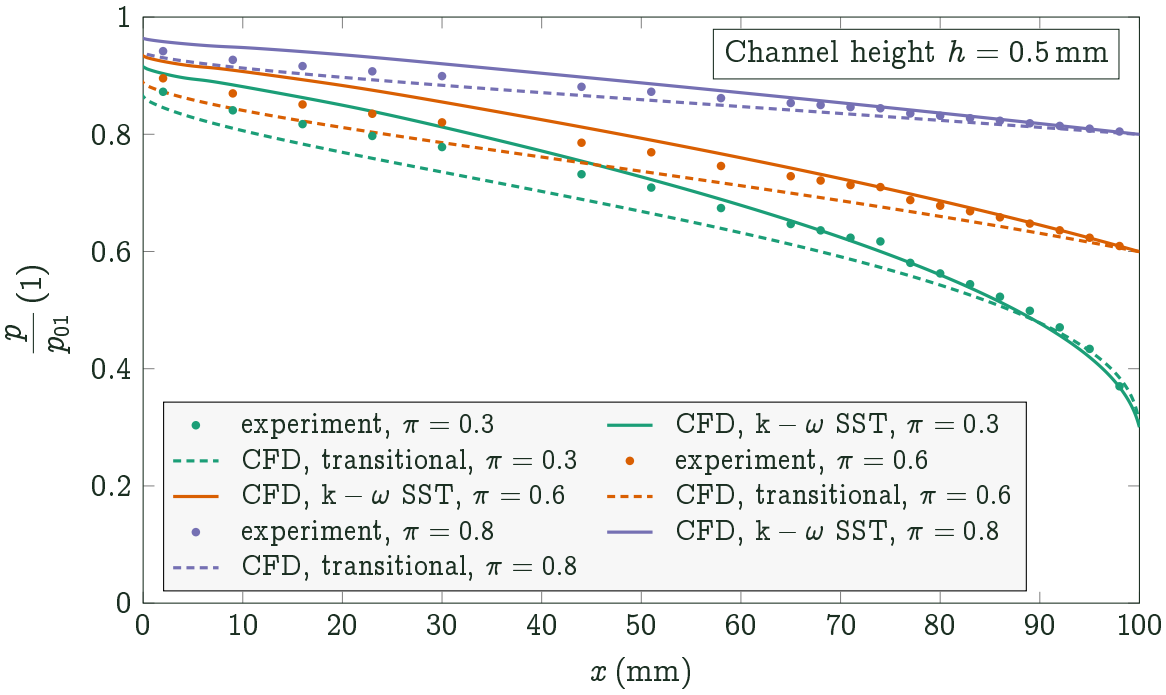

Figure 33: *Distributions of the normalized static pressure* $\frac{p}{p_{01}}$ *along the channel length* x *for channel of the height* $h = 0.5\,\mathrm{mm}$ *and pressure ratios* $\pi = 0.3$, 0.6 *and* 0.8. *Comparison of measurements and simulations.*

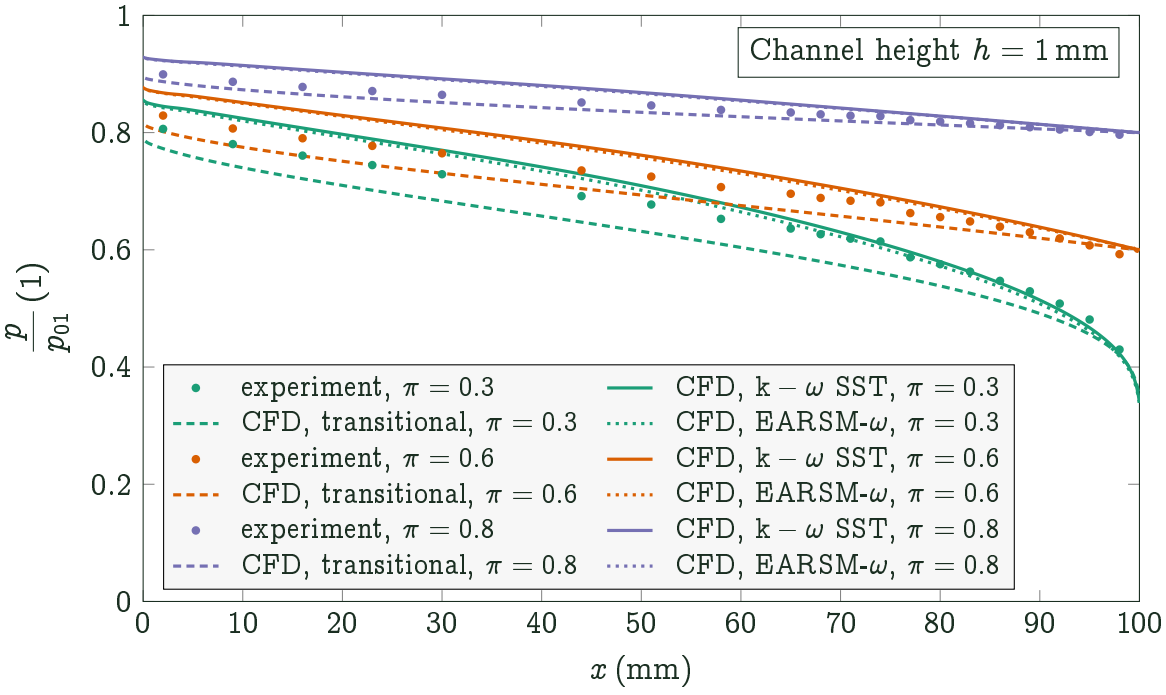

Figure 34: *Distributions of the normalized static pressure* $\frac{p}{p_{01}}$ *along the channel length* x *for channel of the height* $h = 1\,\mathrm{mm}$ *and pressure ratios* $\pi = 0.3$, 0.6 *and* 0.8. *Comparison of measurements and simulations.*

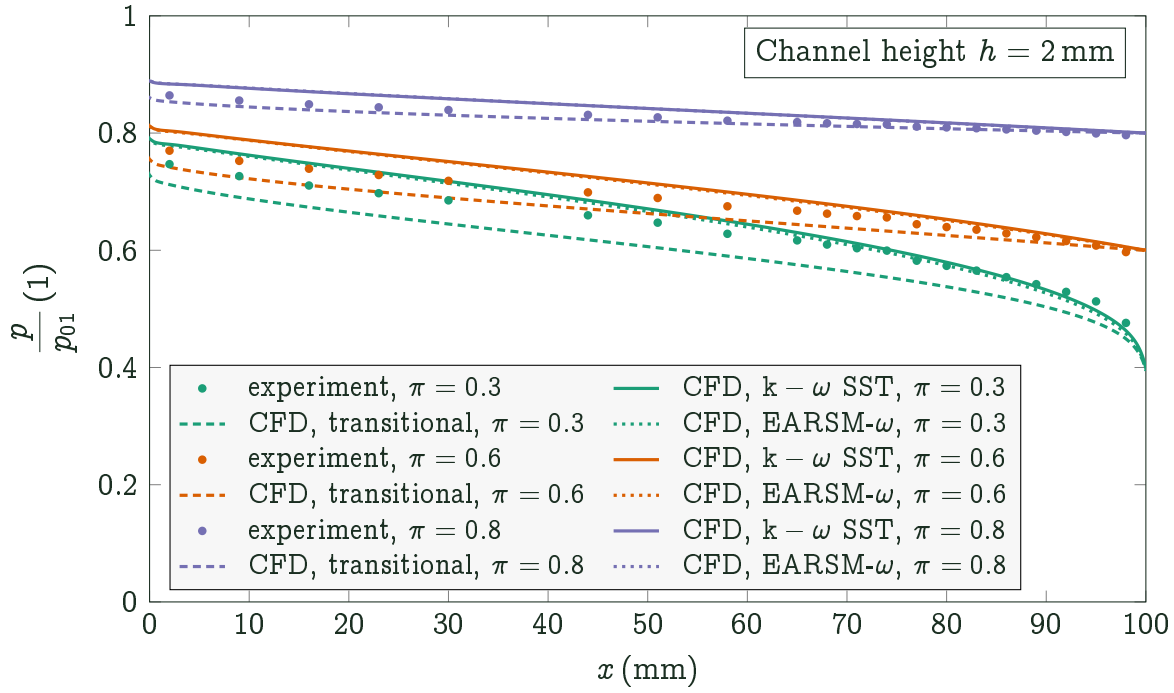

Figure 35: *Distributions of the normalized static pressure* $\frac{p}{p_{01}}$ *along the channel length* x *for channel of the height* $h = 2\,\text{mm}$ *and pressure ratios* $\pi = 0.3$, 0.6 *and* 0.8. *Comparison of measurements and simulations.*

Another comparison provides the graph in Figure 36. This graph shows values of total pressure measured in the mid channel in location $x = 98\,\text{mm}$ (2 mm downstream the exit plane) with respect to pressure ratio π for various channel heights and compares it to computed values. The comparison reveals that both transitional models (Transitional SST and $\gamma - Re_{\theta_t}$) significantly over-predicts the entrance length resulting in almost no total pressure drop along the entire channel length. This is most apparent for channel heights $h = 1$ and $h = 2\,\text{mm}$. In the case of $h = 0.5\,\text{mm}$, the computed total pressure drop is present but its magnitude is still much lower then the measured one.

When the measurements were completed with rough wall measurements, the total pressure loss was evaluated in terms of total pressure loss coefficient

$$\zeta = 1 - \frac{p_0}{p_{01}}. \tag{45}$$

These results are summarized in the graph in Figure 37, showing the total pressure loss coefficient ζ plotted against the pressure ratio π for various channel heights and roughness. It is rather surprising that the higher pressure loss was measured for smooth variants of the channel walls than for its rough variants. This is most apparent for the channel height $h = 2\,\text{mm}$. The plot pictures also the error bars

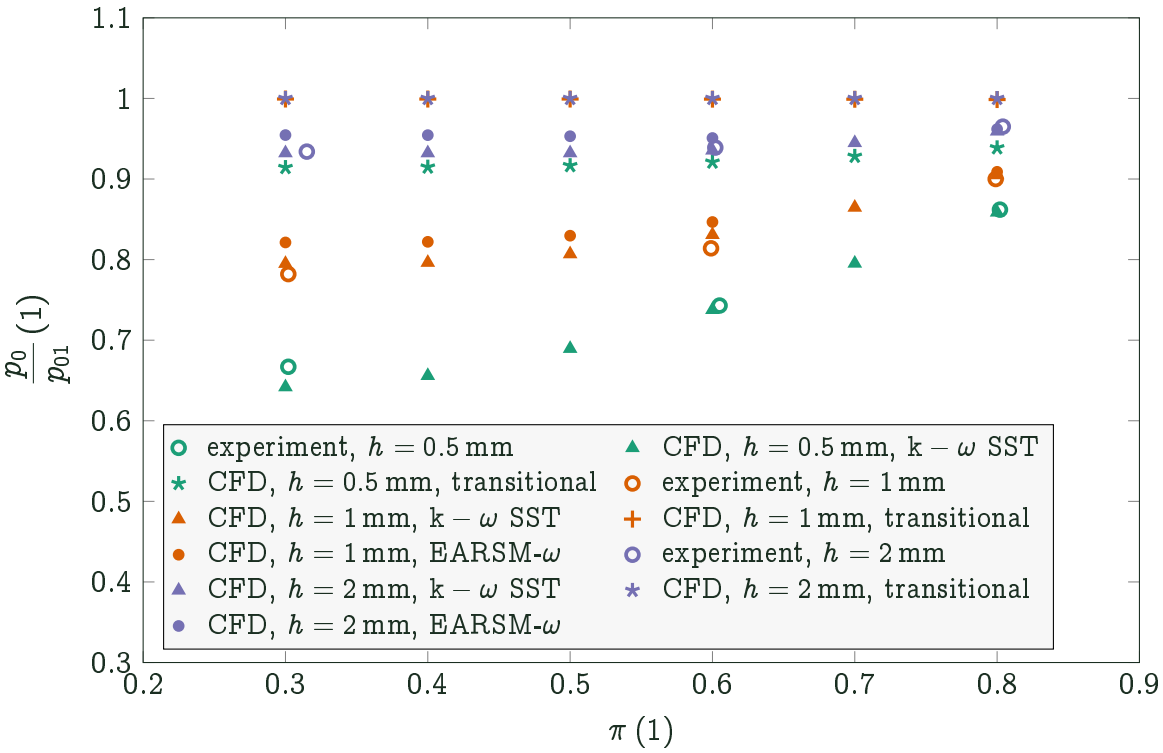

Figure 36: *Normalized total pressure* $\frac{p_0}{p_{01}}$ *measured in mid channel in location* $x = 98$ mm *with respect to pressure ratio* π *for various channel heights* h.

which show standard deviation of both total pressure loss coefficient ζ and pressure ratio π. It is well apparent that smooth wall variants exhibits for most cases larger deviations most likely due to stronger flow oscillations, nevertheless, this hypothesis needs to be explored by further measurements.

Even though the measuring facility underwent major improvements compared to the version used before [A5] and total pressure data gave new valuable results, it is still difficult to assess the mode of the flow and its development based on the pneumatic measurements only. Yet, having such data is important not only for assessments of the numerical simulations but besides that also for further investigation since the knowledge of pressure distributions is essential for wall shear stress evaluation using a hot film probe.

9.1.2 Results of the Optical Measurements

As a next step, the assessment of the optical measurements and its comparison with computed flow fields was made. Although the new high resolution camera was used for the optical measurements a substantial part of the flow field in the wall vicinity is not clearly visible perhaps due to shadow caused by not ideal alignment of the optical path with the channel walls. Therefore, it is not possible to evaluate density

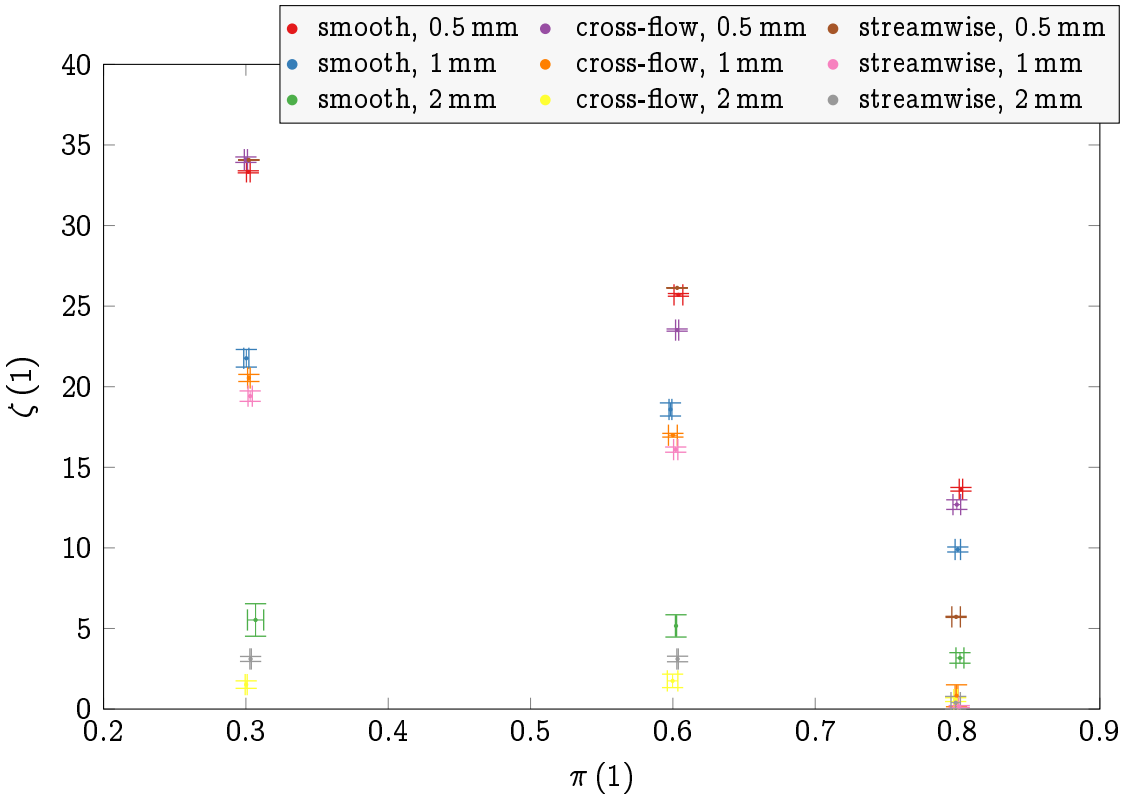

Figure 37: *Total pressure loss coefficient ζ (45) plotted against the pressure ratio π for various channel heights and wall roughness.*

profiles up to channel walls to estimate wall shear stress. Nevertheless, at least some qualitative assessment of the measured flow fields to computational results is possible.

Figure 38 shows the computed density contours obtained using k $-$ ω SST turbulence model (top of each subfigure) and interferograms of the exit region for channel height $h = 2\,\text{mm}$ and three different pressure ratios. As can be seen both the shape of the density contours close to the channel exit and flow structures downstream the sudden expansion seem to show quite a good agreement with the interferograms. This might lead to a conclusion that the flow in the cases above is most likely turbulent. Though, as it is impossible to evaluate the wall shear stress from the optical measurements, it is not possible to draw this conclusion with certainty. This uncertainty was later confirmed by further measurements, which revealed that the flow is not completely turbulent.

Regarding the roughened walls, the resulting interferograms are well comparable in the case of streamwise roughness, however, in the case of cross flow roughness, the interference fringes are sort of blurred (see Figure D.3 in Appendix D). It is not clear whether it is because the light is scattered by the roughness in such way it makes the resulting image fuzzy or if it is because the flow field oscillates. To answer this question, the fast camera should have been employed but it would also require

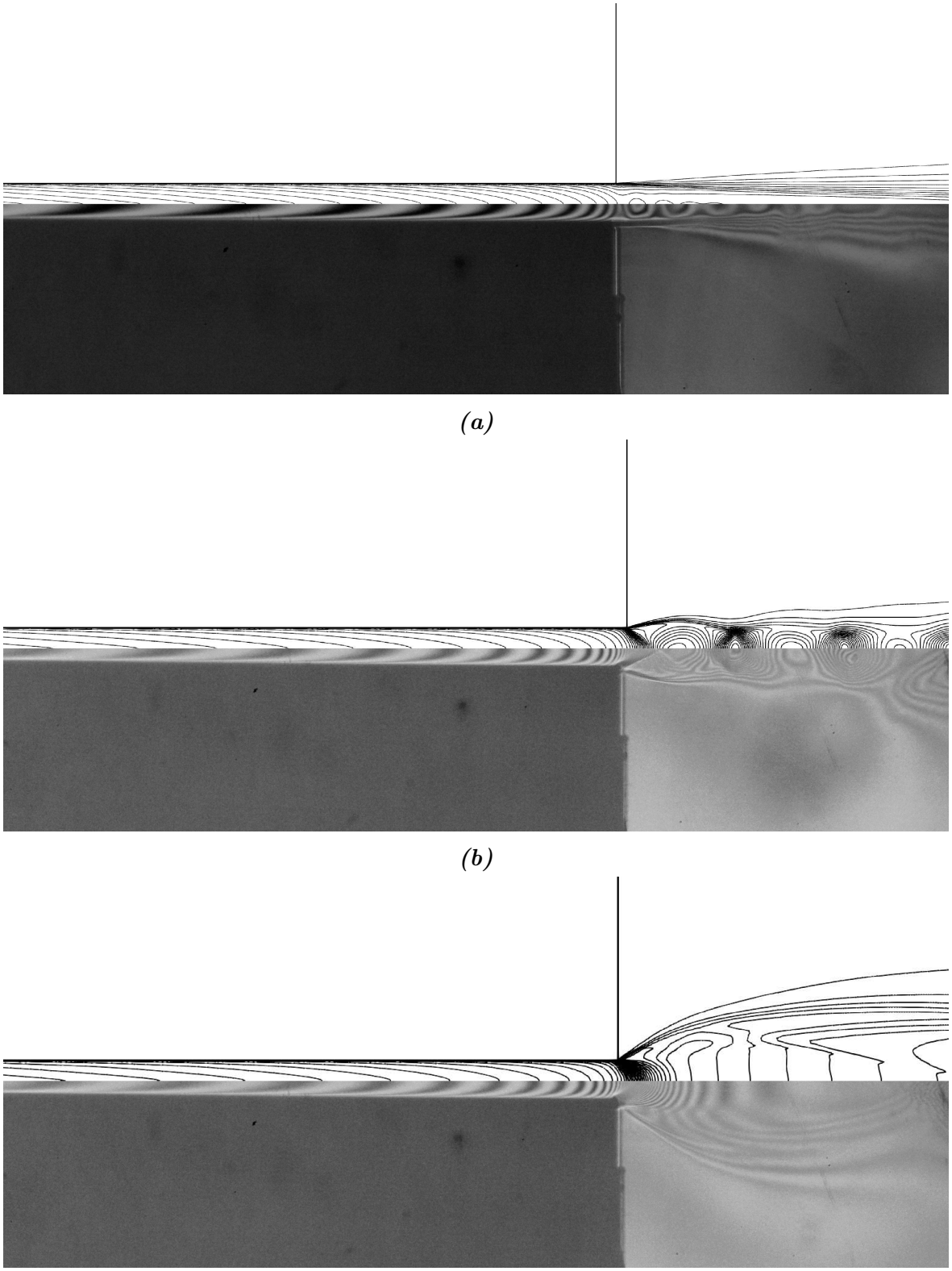

(a)

(b)

(c)

Figure 38: *Comparison of density contours computed using* $\mathrm{k}-\omega$ *SST turbulence model (top) with interferograms (bottom) for pressure ratio* $\pi = 0.44$ *(a),* $\pi = 0.219$ *(b) and* $\pi = 0.088$ *(c).*

significant changes in the whole imaging system, mainly in different light source and its synchronization with the camera. Since such an upgrade is far beyond the scope of this work, the most promising way to evaluate possible flow oscillations seams to be the hot-film probe.

9.1.3 Qualitative Hot-film Probe Investigation Results

Further insight in the problem of the flow transition in investigated narrow channels is offered by qualitative hot film probe measurements. This investigation is based on the analysis of the raw hot-film probe signal as well as the analysis based on the signal *skew function* defined by equation (28) as described in section 5.7.2.

Signal samples shown in Figure 39 well illustrate the method of turbulent transition identification based on the skew function. First sample (A) exhibits low level of perturbations with low signal skewness indicating laminar flow. Sample B contains perturbations, which indicate transition onset and result in higher positive skewness. Sample C illustrates the situation with approximately equal periods of turbulent and laminar flow ($\gamma = 0.5$), resulting in the low signal skewness. At the same time, we can observe that the fluctuations are maximal at this stage. Sample D shows signal that is predominantly turbulent with laminar perturbations ($\gamma \approx 0.75$). In this case the skew function become negative before the flow turn to be fully turbulent with approximately zero skewness as shows the last sample (E). The drawback of this method is that even some occasional disturbance might significantly affect resulting skewness. Therefore, it is necessary to assess the course of the raw signal and, if necessary, to clip the signal so as it does not contain any isolated disturbances. Although, it might be difficult in some cases to decide which perturbations are turbulence transition related and which are of different origin that should be cut off. Further paragraphs present the obtained results of the hot-film measurements. Subsequently, based on this, the flow development in narrow channels of various height and under various back pressure ratios is discussed.

Figures 40, 41 and 42 picture the series of graphs of the raw hot-film probe signal for smooth channel walls, three locations of the hot film probe, three different channel heights, and pressure ratio $\pi = 0.3$. It can be seen that for channel heights $h = 0.5\,\text{mm}$ and $h = 1\,\text{mm}$ the signal exhibits turbulent character from the plug No. 3, therefore, the transition in these two cases most likely completed between plugs No. 1 and 3. It is worth noting the reduced signal width in the last plug (No. 5), which is probably caused by steep expansion which occurs close to the channel exit and is more pronounced with decreasing channel width. If we look on the situation for the channel height $h = 2\,\text{mm}$ shown in Figure 42, we can see that the transition

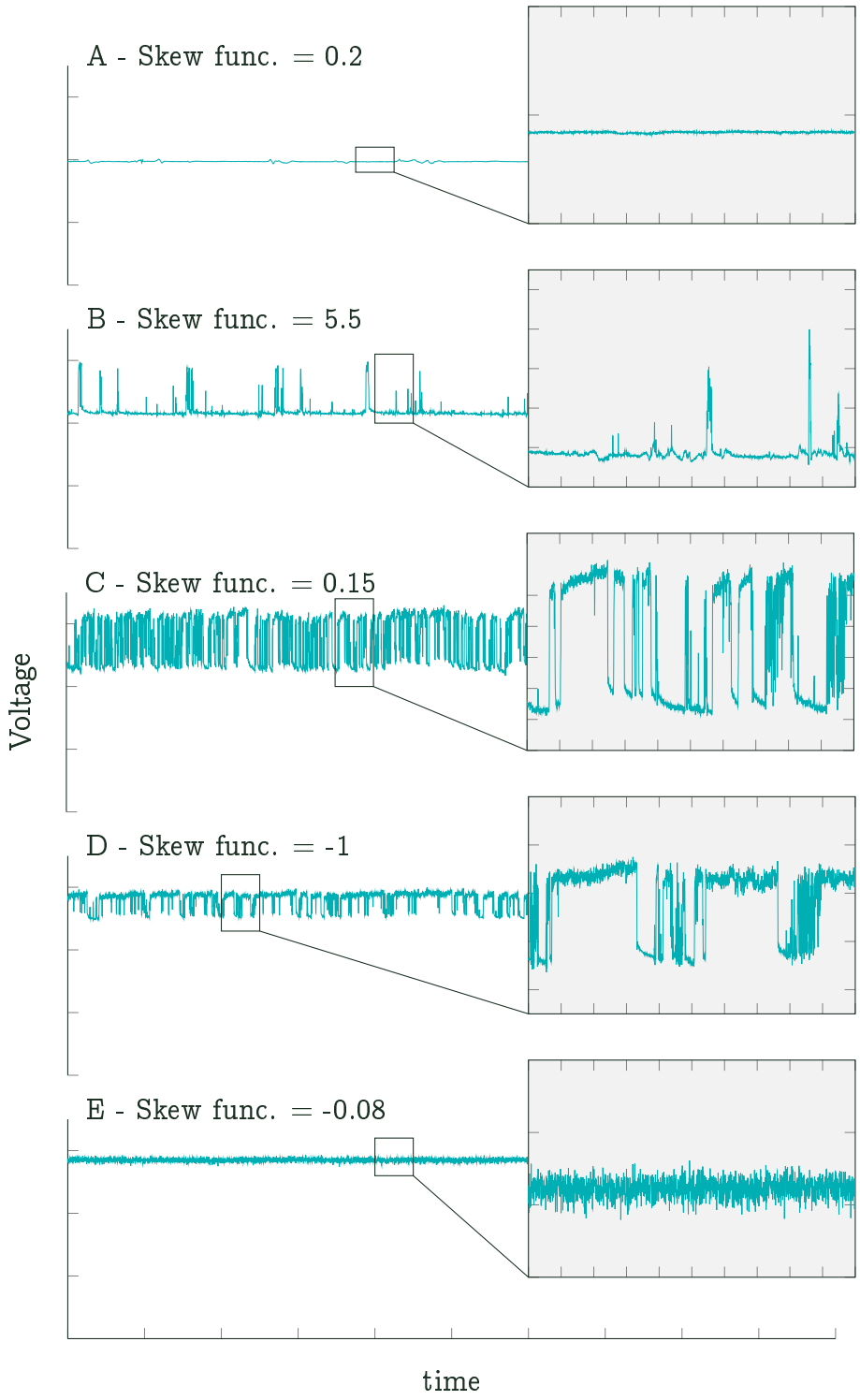

Figure 39: *Illustration of the development of the hot-film probe signal across the laminar-turbulent transition with the corresponding skew function.*

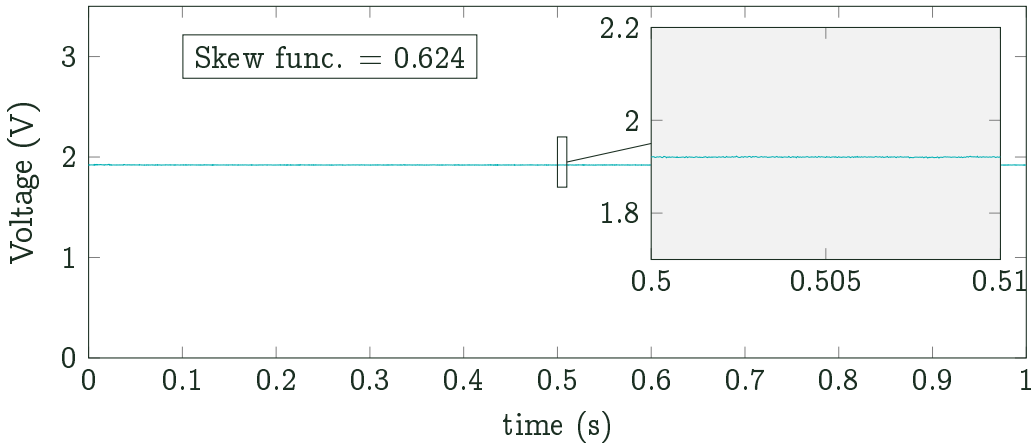

(a)

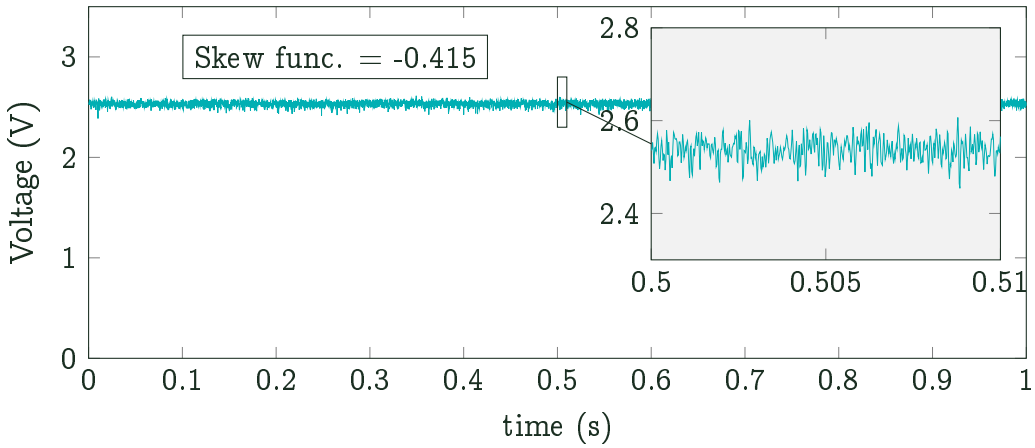

(b)

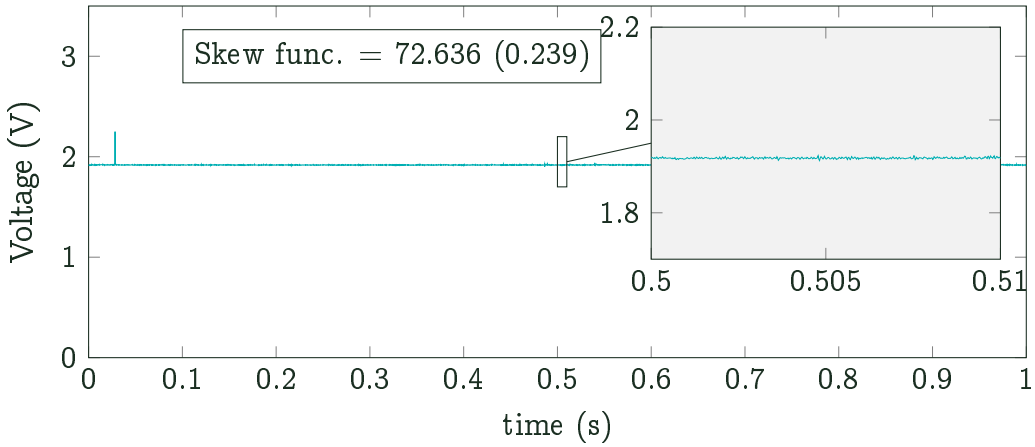

(c)

Figure 40: *Hot-film probe signal measured in plug 1 (a), 3 (b) and 5 (c) in the smooth channel of the height* $h = 0.5\,\mathrm{mm}$ *and* $\pi = 0.3$.

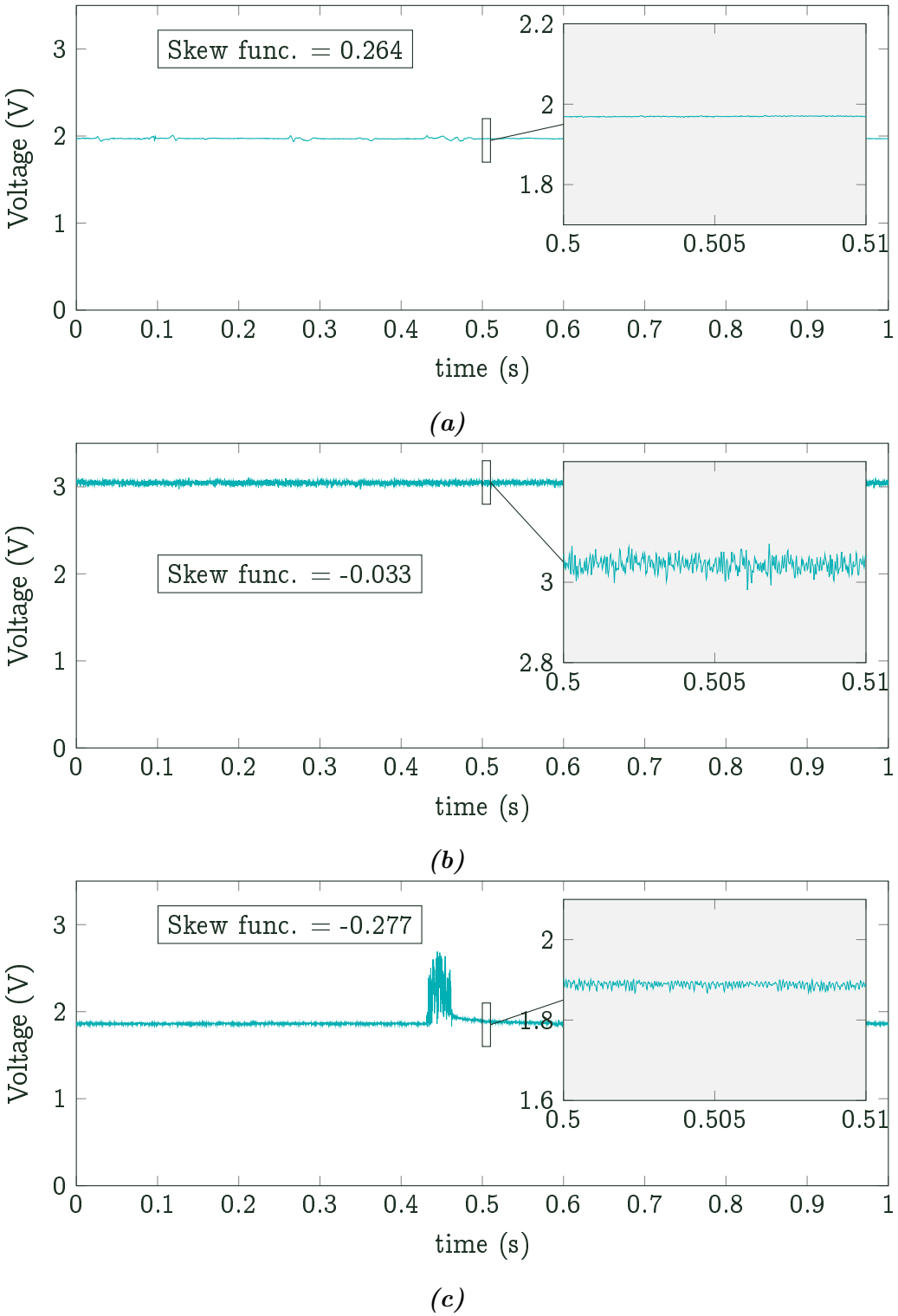

Figure 41: *Hot-film probe signal measured in plug 1 (a), 3 (b) and 5 (c) in the smooth channel of the height* $h = 1\,\mathrm{mm}$ *and* $\pi = 0.3$.

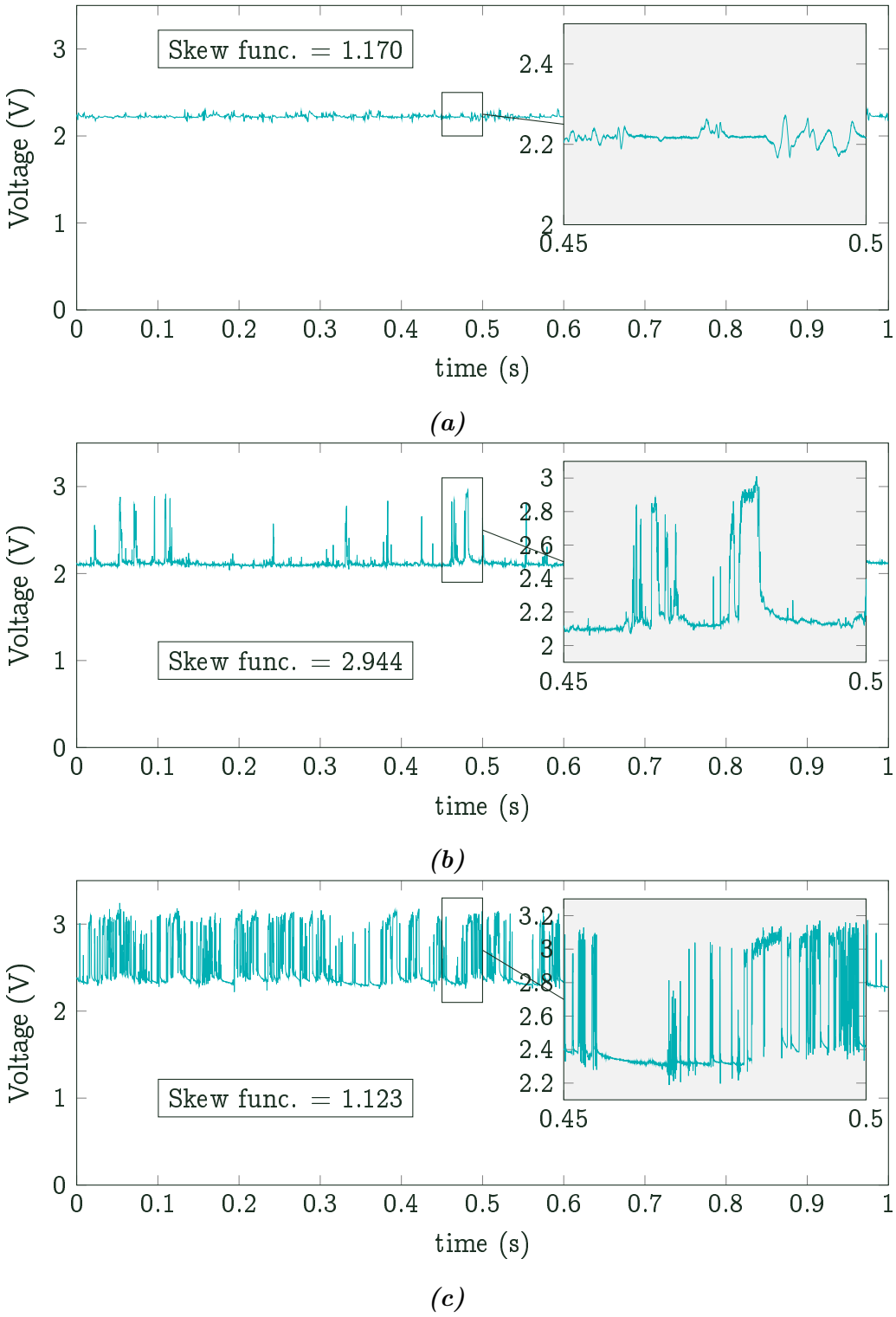

Figure 42: *Hot-film probe signal measured in plug 1 (a), 3 (b) and 5 (c) in the smooth channel of the height* $h = 2\,\mathrm{mm}$ *and* $\pi = 0.3$.

is not completed even at the location of the plug No. 5, in which the signal shows highly intermittent characteristics and the positive skew function suggests the values of intermittency $\gamma < 0.5$. In the case of increased pressure ratio, the situation is comparable with the case of the pressure ratio $\pi = 0.3$ without any major qualitative differences observable in the raw signal.

However, the situation become different in the case of rough walls (Figures in Appendix E). In the channel of the height $h = 0.5\,\text{mm}$ and cross-flow roughness, the significant oscillations, which show nearly harmonic behaviour in the plug No. 1, appeared in the signal. Using the spectral analysis, the significant frequency was identified to be approximately 590 Hz. These oscillations, however, disappeared for larger channel gaps and for increased pressure ratios π. For the channel height $h = 2\,\text{mm}$, the influence of the cross-flow roughness seems to be in shifting of the transition upstream, resulting in lower skew function value measured in the plug No. 5, which corresponds to intermittency $\gamma > 0.5$. This also explains higher standard deviations of the total pressure measured for smooth walls in the plug No. 5 as discussed earlier in Section 9.1.1. It is because in the smooth case, the fluctuation maximum related with intermittency $\gamma = 0.5$ is apparently closer to the channel exit, and thus to the plug No. 5, compared to roughened walls, in which case the fluctuation maximum occurs earlier.

Streamwise roughness (Figures E.7, E.8 and E.9) appears to have very similar effect to the cross-flow roughness including shift of the transition upstream, which is, however, not so significant in this case.

9.1.4 Quantitative Hot-film Probe Investigation Results

A different point of view provides the quantitative hot-film probe investigation. Figures 43 and 44 show comparison of the computed wall shear stress distributions along the channel length with the measured data including data measured in channels with rough walls with cross-flow roughness. If we first focus on the measured data only, we can see that the smooth wall value is comparable to that of rough wall solely in the location of the first measuring plug in the case of channel height $h = 0.5\,\text{mm}$. In all other locations, the wall shear stress shows expected behaviour of increased values in the case of rough walls.

Comparing the measured data with computations, it can be seen that in the case of the channel height $h = 0.5\,\text{mm}$ the values computed using $\text{k} - \omega$ SST turbulence model well correspond to those measured using rough walls in both the absolute value of the wall shear stress and overall trend of the distribution, while the transitional models significantly underestimates the wall shear stress. This is most likely

caused by overestimation of the entrance length by the transitional model as already illustrated using total pressure data in section 9.1.1. An important point is that computed values corresponding to smooth walls are in this case larger than the smooth wall measurements. This might question whether the use of k $-\omega$ SST turbulence model is adequate for the smooth narrow channels equipped with smooth shaped inlet part. Under such conditions the entrance length might increase and the transition to turbulence might delay leading to lower wall shear stress values than that predicted by the fully turbulent model. This problem seems to increase with increasing channel height.

As can be seen in Figure 44, showing the case with the channel height $h = 2\,\mathrm{mm}$, none of the used models predicts the wall shear stress satisfactorily. In this case, the better prediction over the early portion of the channel was given by transitional model and the fully turbulent one seems to significantly over-predict the wall shear stress. This is most likely caused by the fact that the flow is not yet fully developed, and as can be seen in the qualitative analysis, the mean value of the anemometer voltage, from which the wall shear stress is calculated, is in this case somewhere between fully laminar and fully turbulent value. The increased value of the wall shear stress in the case of rough wall is also in accordance with the observations of qualitative analysis which shows that the transition in the rough case is shorter resulting in higher intermittency γ i.e. higher proportion of the turbulent signal over the laminar one and thus higher mean voltage measured using hot-film probe.

The assessment of the conducted measurements and computations seems to reveal that the flow in investigated channels is for most of the regimes transitional and not fully developed with the exception of the channel height $h = 0.5\,\mathrm{mm}$. Only this case appeared to be fully turbulent towards the channel exit. Due to this, the fully turbulent numerical models proved not to be satisfying for wall shear stress determination and neither did the transitional model, which significantly over-predicts the entrance length.

Additionally, the mean friction coefficient $\bar{f}$ was evaluated using the equation for the adiabatic, constant area flow [10]

$$\bar{f}\frac{L}{D} = \left(\bar{f}\frac{L_{\max}}{D}\right)_{M_1} - \left(\bar{f}\frac{L_{\max}}{D}\right)_{M_2}. \tag{46}$$

In this equation the term $\left(\bar{f}\dfrac{L_{\max}}{D}\right)$ is solely a function of the Mach number at the given location of the channel

$$\bar{f}\frac{L_{\max}}{D} = \frac{1-M^2}{\gamma M^2} + \frac{\gamma+1}{2\gamma}\ln\frac{(\gamma+1)\,M^2}{2\left(1+\dfrac{\gamma-1}{2}M^2\right)}. \tag{47}$$

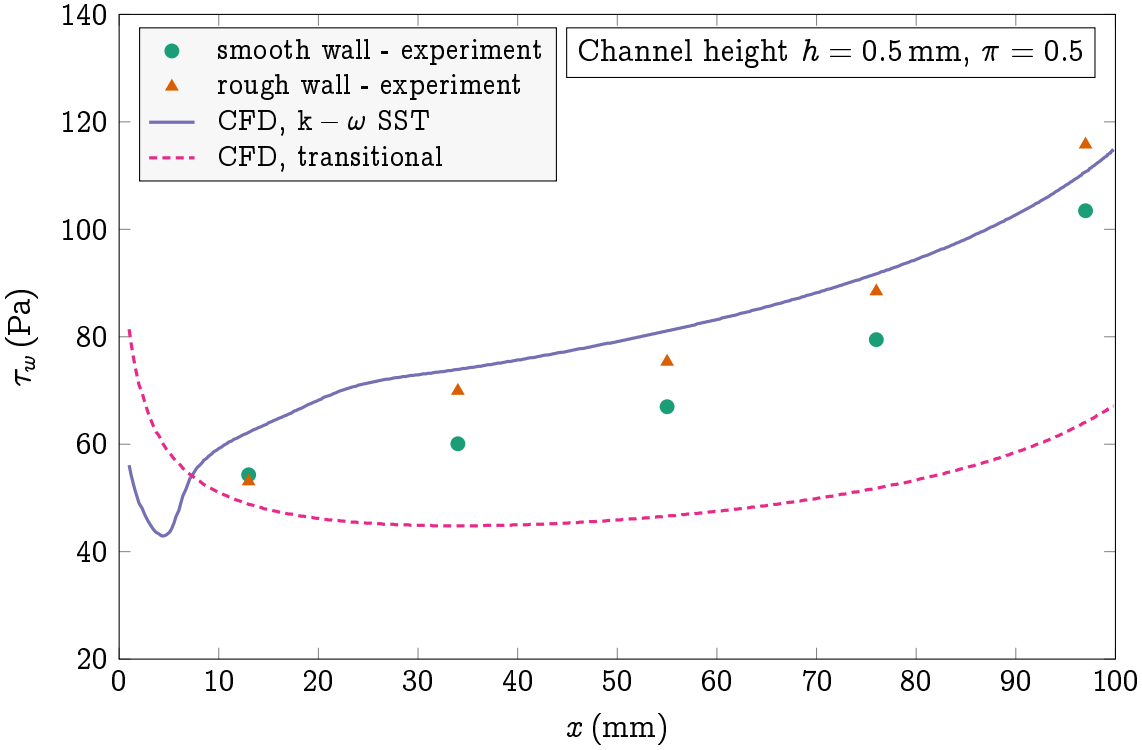

Figure 43: *Plot of the wall shear stress τ_w over the length of the channel of the height $h = 0.5\,\text{mm}$ and for $\pi = 0.5$. Experiment and CFD values.*

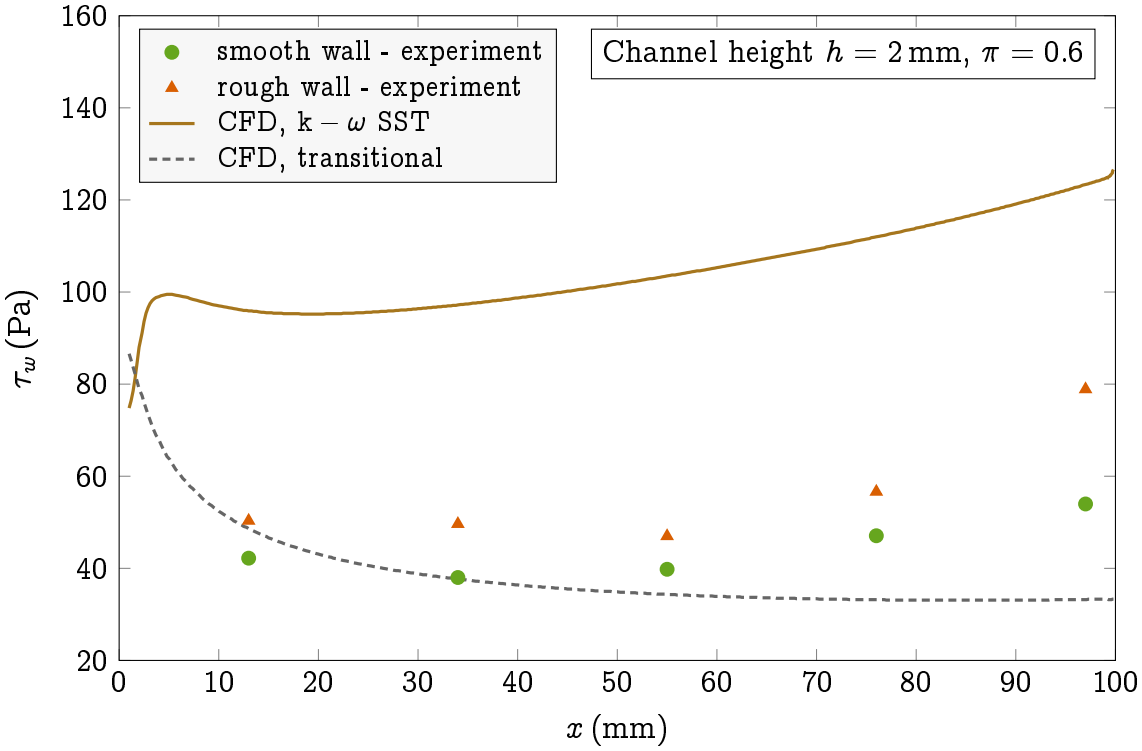

Figure 44: *Plot of the wall shear stress τ_w over the length of the channel of the height $h = 2\,\text{mm}$ and for $\pi = 0.6$. Experiment and CFD values.*

Table 6: *Mean friction factor $\bar{f}$ evaluated using one-dimensional approach for adiabatic, constant area flow. Values for channel height $h = 0.5\,\text{mm}$ and various pressure ratios π.*

	mean friction factor $\bar{f}$ (1)		
π	smooth wall	streamwise roughness	cross-flow roughness
0.3	0.0084	0.0063	0.008
0.6	0.0079	0.0052	0.0071
0.8	0.005	0.0159	0.0053

Since this relation is based upon the one-dimensional theory, and thus a fully developed flow is assumed, only the case of the channel height $h = 0.5\,\text{mm}$, which provides largest length to height ratio, was evaluated.

The resulting values of the mean friction factor for different surface roughness and various pressure ratios are summarized in Table 6. Taking into account that the Reynolds number was ranging from approximately 3 500 to 4 000 (considering height h as a characteristic dimension), the mean values of the friction factor are by an order of magnitude smaller than what corresponds to Moody chart shown in Figure 1. Moreover, no particular difference is observable between smooth and cross-flow roughness. The reason might be in still not fully developed flow even in the case of $h = 0.5\,\text{mm}$. Even though the length to height ratio in this case is 200 and the limiting ratio is referenced to be approximately 50 [10], it is conceivable that for narrow channels, the length for which the flow experiences dramatic changes in velocity profile due to both transition from laminar to turbulence and effects of the channel inlet and exit might affect much larger portion of the channel compared with larger channels. It is referenced in [38] that under such conditions, the one-dimensional approach might falsely yield even negative values of the friction factor. Therefore, the one-dimensional approach described in [10] and used in study [8] seems to fail in correlating the wall shear stress in investigated channels, and thus, different methods such as hot-film measurements or numerical simulations are necessary for appropriate wall shear stress estimation.

9.2 Aerodynamic Choking Analysis

The next research question stated in Section 3 was whether the flow of the viscous compressible fluid through narrow channels experiences the separation and shift of critical and sonic conditions due to friction as claimed based on the theoretical in-

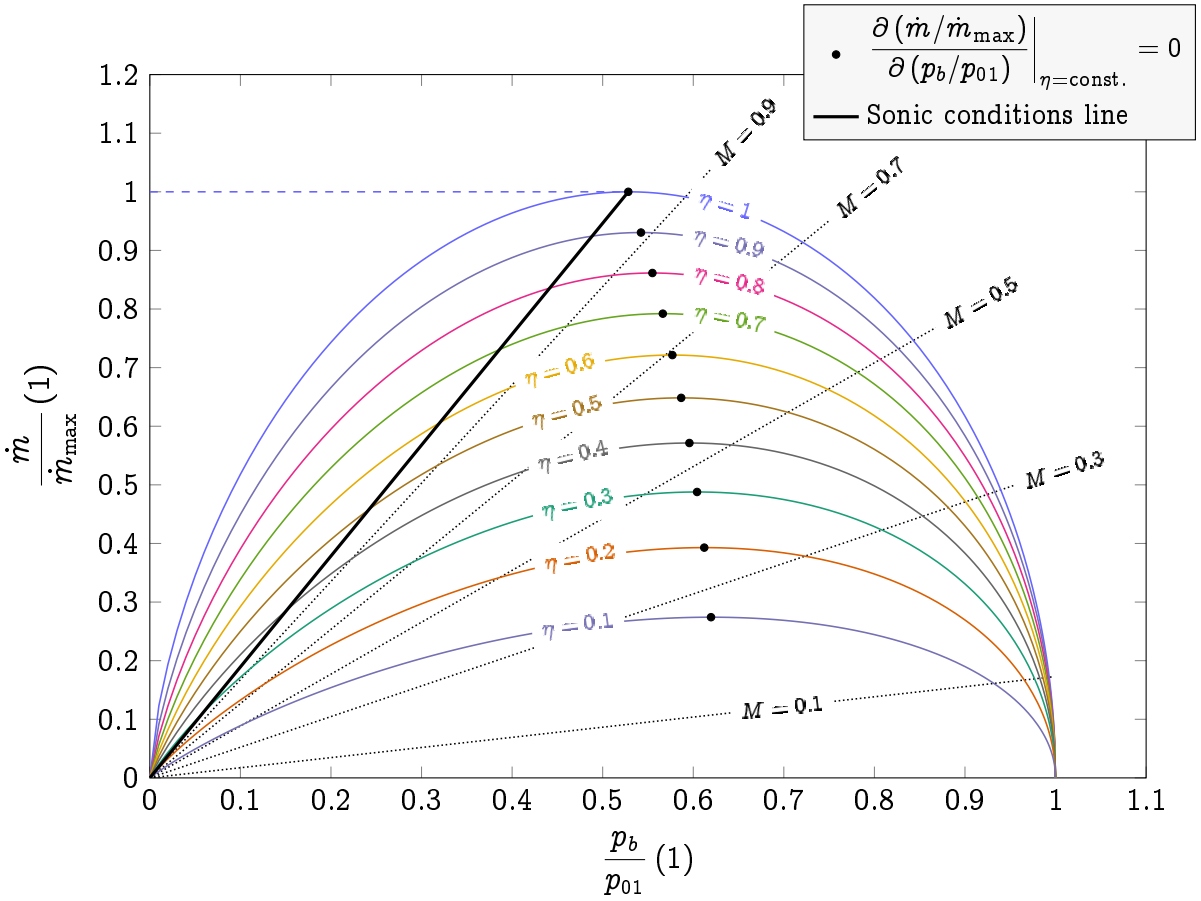

Figure 45: *Discharge diagram showing the relation between the normalized mass flow rate* $\frac{\dot{m}}{\dot{m}_{max}}$ *and back pressure ratio* $\pi = \frac{p_b}{p_{01}}$ *for constant thermodynamic efficiency* η.

vestigation by the authors of study [13], the results of which are illustrated on the graph in Figure 2.

The uppermost curve in so called *discharge diagram* in Figure 45 shows the theoretical dependency of the relative mass flow rate $\frac{\dot{m}}{\dot{m}_{\max}}$, which can be discharged through the channel, on the driving pressure ratio of the back pressure to inlet stagnation pressure $\pi = \frac{p_b}{p_{01}}$ for ideal case of thermodynamic efficiency $\eta = 1$. Since the mass flow rate $\dot{m}$ through the channel or nozzle of the minimal cross-section A is given by equation

$$\dot{m} = \frac{A p_0}{\sqrt{T_0}} \sqrt{\frac{\gamma}{R}} M \left(1 + \frac{\gamma - 1}{2} M^2\right)^{\frac{\gamma + 1}{2(1-\gamma)}}, \tag{48}$$

and the maximal mass flow rate $\dot{m}_{\max}$ is attained for $M = 1$ (sonic conditions), the relative mass flow rate is then for $\eta = 1$, and thus for $p_0 = p_{01} =$ constant, given as

$$\frac{\dot{m}}{\dot{m}_{\max}} = M \left(\frac{1 + \frac{\gamma - 1}{2} M^2}{1 + \frac{\gamma - 1}{2}} \right)^{\frac{\gamma + 1}{2(1-\gamma)}} . \tag{49}$$

It can be derived that the ideal mass flow rate curve reaches its maximum for any stagnation conditions at critical pressure ratio

$$\left(\frac{p_b}{p_{01}} \right)_* = \left(\frac{2}{\gamma + 1} \right)^{\frac{\gamma}{\gamma - 1}} . \tag{50}$$

This critical pressure ratio coincides in the ideal case with the maximum of the theoretical mass flow rate curve. This maximum can be found by differentiating the mass flow rate $\dot{m}$ with respect to pressure ratio $\frac{p_b}{p_0}$ and equating it to zero

$$\frac{\partial \dot{m}}{\partial \left(\frac{p_b}{p_0} \right)} = 0. \tag{51}$$

However, it is proved by experiments that the curve is valid only for pressure ratios greater than critical [10]. Below the critical pressure ratio, which is approximately 0.5283 for a gas with the ratio of specific heats $\gamma = 1.4$, the mass flow rate does not decrease but stays constant at its maximal value (dashed line in Figure 45) - the flow is then said to be aerodynamically choked, which means that any further reduction of the back pressure p_b does not lead to increase of the mass flow rate. This is in contrast with the theoretical curve, which decreases for lower pressure ratios than critical as apparent in Figure 45).

If we consider thermodynamic efficiency η lower than unity, the total pressure p_0 is no longer equal to p_{01}. Therefore, it is necessary to elaborate the equation for the relative mass flow rate with respect to pressure ratio $\frac{p_b}{p_{01}}$ with η as a parameter. Such equation takes the form

$$\frac{\dot{m}}{\dot{m}_{\max}} = \sqrt{\frac{2\pi^2}{\gamma - 1} \frac{1 - k}{k^2} \left(1 + \frac{\gamma - 1}{2} \right)}, \tag{52}$$

where

$$k = 1 - \eta(1 - \pi^{\frac{\gamma - 1}{\gamma}}) \tag{53}$$

and

$$\pi = \frac{p_b}{p_{01}}. \tag{54}$$

If we draw these dependencies for various values of η in the discharge diagram in Figure 45, it can be seen that these lines have a maximum shifted towards the higher pressure ratios as the efficiency η decreases (black points on the lines of constant efficiency in Figure 45). This maximum can be found out for given η using equation (7). It is apparent that this maximum is different from the sonic conditions ($M = 1$) for the same thermodynamic efficiency η given by equation (9), which seems to be in accordance with the findings published in study [13].

The sonic conditions line in discharge diagram connects points $(0; 0)$ and $\left(\left(\frac{p_b}{p_{01}}\right)_*; 1\right)$. Other lines of constant Mach number with the efficiency as a parameter can be found by calculating the total pressure p_0 for given Mach number M and inlet total pressure p_{01} using equation

$$p_0 = p_{01}\left\{\frac{1}{\eta}\left[1 + \frac{\gamma - 1}{2}M^2\right]\left[\left(1 + \frac{\gamma - 1}{2}M^2\right) - 1 + \eta\right]\right\}^{\frac{\gamma}{\gamma - 1}} \tag{55}$$

and substituting it to equation (48). These lines are drawn in discharge diagram in Figure 45 as dotted lines for several values of Mach number.

To answer the second research question, the CFD results were analysed to determine the relative mass flow rate with respect to pressure ratio. The mass flow rate $\dot{m}$ was acquired by integration throughout the exit plane of the channel while the maximum mass flow rate was calculated using the equation (48) for each channel height and given boundary conditions, provided that $M = 1$, $p_0 = p_{01}$ and A is equal to channel cross section. Then, the resulting data points for each channel height were plotted in discharge diagram in Figure 46. As can be seen there, the relative mass flow rate increases with decreasing pressure ratio well beyond the ratio given by equation (7) and in fact reaches the maximum for sonic conditions given by equation (9). This can be observed for all cases except the case of $h = 0.5\,\mathrm{mm}$, which does not yet cross the sonic conditions line even for the lowest examined pressure ratio. From this diagram it is obvious that the contradiction presented in study [13] stems from the fact that for non-ideal flow, the process of decreasing back pressure does not follow the curve of constant efficiency, which happens solely for ideal case of $\eta = 1$. It can be deduced from the plot in Figure 46 that the only way to follow the curve of constant efficiency while reducing the back pressure at the same time is by simultaneously reducing the channel height or by increasing channel length. As a

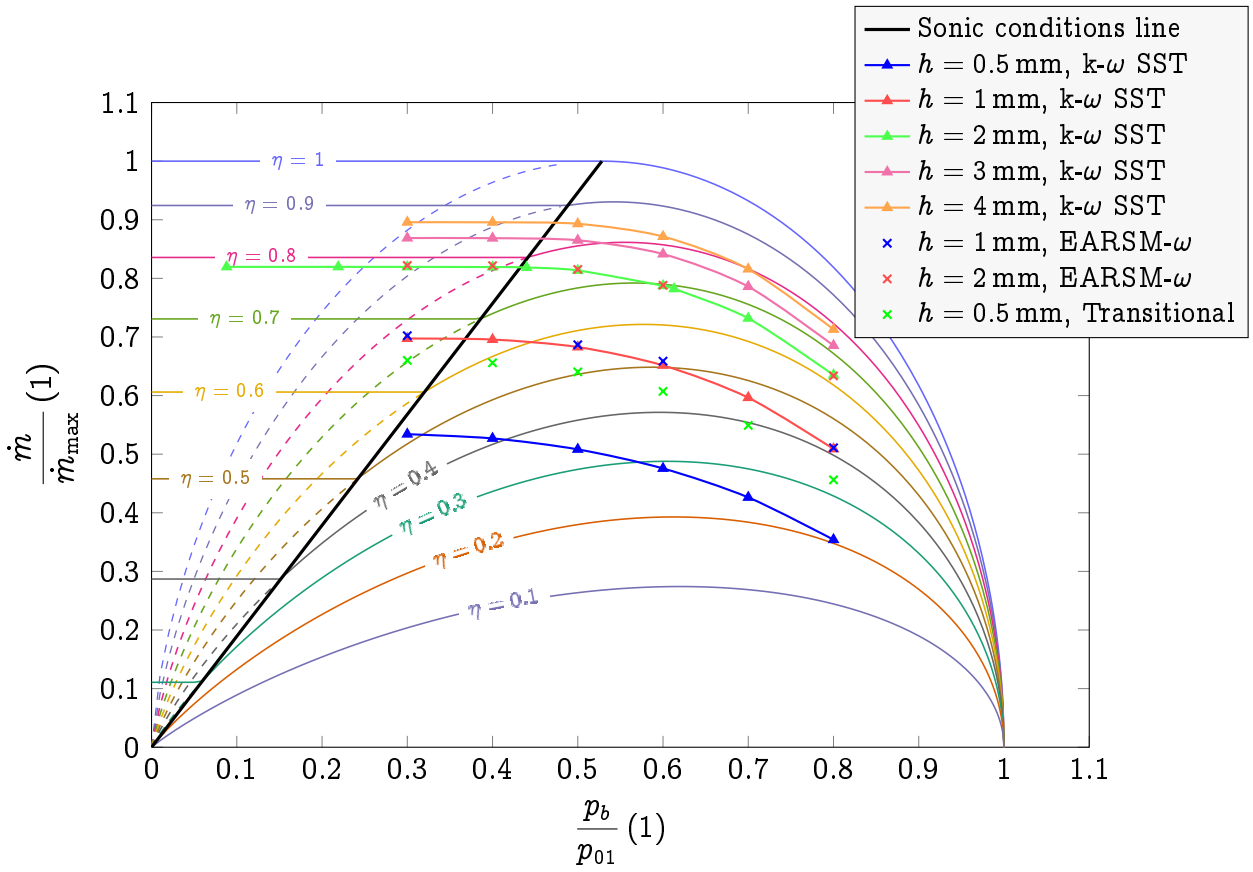

Figure 46: *Discharge diagram with the computed expansion curves for various channel heights using different turbulence models.*

result, it can be concluded that the critical condition acquired by differentiating the equation (51) has very little practical importance for non-ideal flow.

To further analyse the flow choking and provide better insight in the choking process for non-ideal conditions, the relation for efficiency as a function of mass flow ratio was worked out. First, it was necessary to split the diagram to two regions. One for choked flow - left from the sonic conditions line, and the second for non-choked flow - right from the sonic conditions line. To distinguish between these two regions, it was advantageous to work out relation for sonic pressure ratio with respect to relative mass flow rate. This relation is

$$\pi_{\text{sonic}} = \frac{\dot{m}}{\dot{m}_{\max}} \left(1 + \frac{\gamma - 1}{2}\right)^{\frac{\gamma}{1-\gamma}}. \tag{56}$$

Then, if the actual pressure ratio π is higher than obtained π_{sonic}, the flow is not choked and the thermodynamic efficiency can be found by solving quadratic equation

$$b^2\eta^2 - b\left[2 + \left(\frac{\dot{m}_{\max}}{\dot{m}}\right)^2 \frac{2\pi^2}{j^2(\gamma-1)}\right]\eta + 1 = 0, \tag{57}$$

where

$$b = 1 - \pi^{\frac{\gamma-1}{\gamma}} \tag{58}$$

and

$$j = \left(1 + \frac{\gamma-1}{2}\right)^{\frac{\gamma+1}{2(1-\gamma)}}. \tag{59}$$

Solving this equation gives two values of efficiency η, one of which is higher than unity. Since the solution higher than unity violates the second law of thermodynamics, only the root within the interval $\eta \in [0;1]$ is physically possible.

If the pressure ratio π is lower than π_{sonic}, the flow is aerodynamically choked and the thermodynamic efficiency can be calculated using equation

$$\eta = \frac{\gamma-1}{\gamma+1}\frac{1}{1-\pi_{\text{sonic}}^{\frac{\gamma-1}{\gamma}}}, \tag{60}$$

which yields a constant value regardless the decreasing back pressure as illustrated by solid lines of constant efficiency left of the sonic conditions line in diagram in Figure 46.

The same process plotted in $T - \Delta s$ diagram is shown in Figure 47. To plot the points there, the relation for Mach number as a function of relative mass flow rate and exit pressure ratio φ of exit plane pressure p_e to inlet total pressure p_{01}

$$\varphi = \frac{p_e}{p_{01}}, \tag{61}$$

was derived in the form of biquadratic equation

$$\left(\frac{\pi}{j}\right)^2 \frac{\gamma-1}{2} M^4 + \left(\frac{\varphi}{j}\right)^2 M^2 - \left(\frac{\dot{m}}{\dot{m}_{\max}}\right)^2 = 0, \tag{62}$$

where j is given by equation (59). The solution of equation (62) gives two roots, from which only one is positive. Using the positive root we can obtain Mach number and subsequently the static temperature from equation

$$T = T_0\left(1 + \frac{\gamma-1}{2}M^2\right)^{-1}. \tag{63}$$

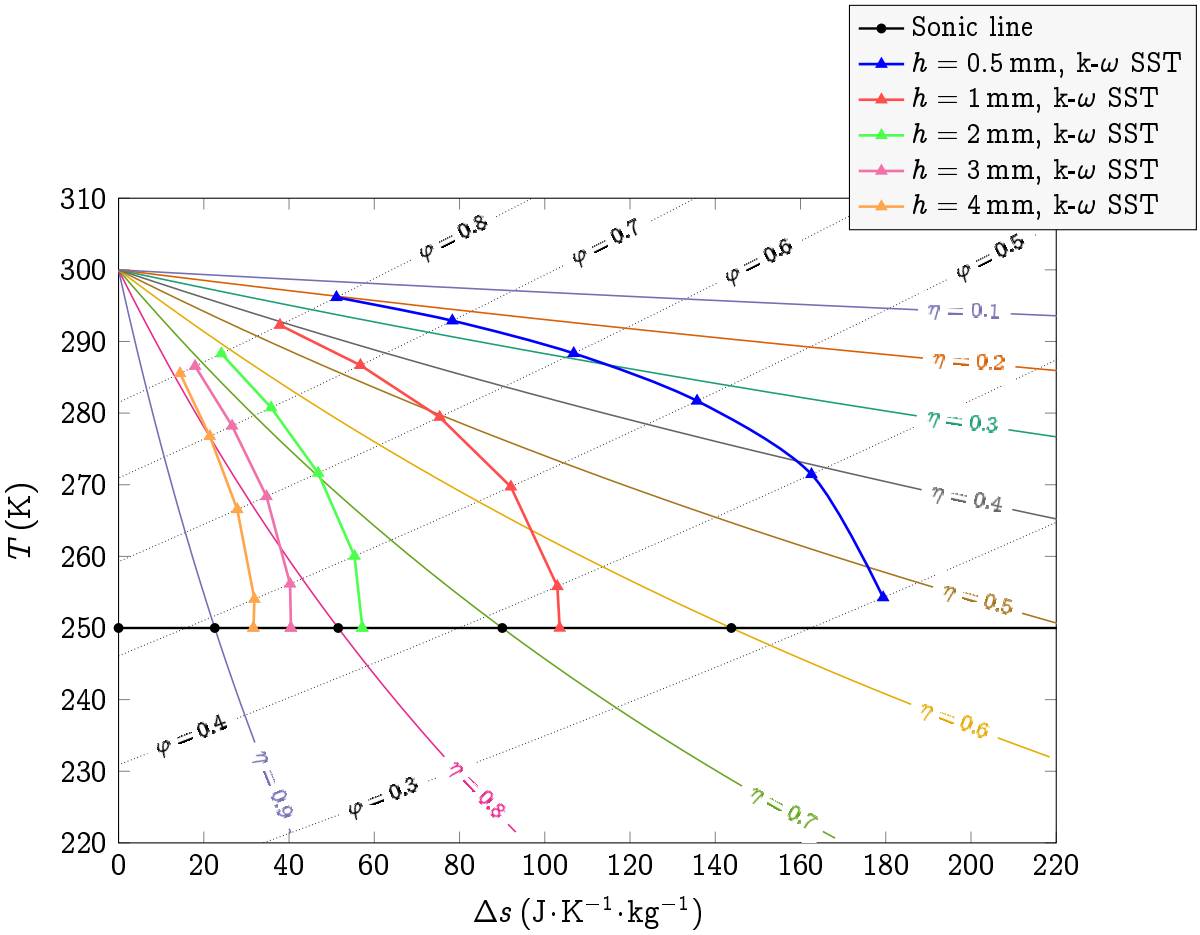

Figure 47: *Narrow channel expansion curves for various channel heights drawn in $T - \Delta s$ diagram together with lines of constant efficiency η and lines of constant exit pressure ratio φ (61).*

As in the case of discharge diagram, the special care must be taken with the points for aerodynamically choked regimes. For these points the Mach number was set to unity and the pressure ratio was taken as the sonic one for given relative mass flow rate determined by equation (56). This step, however, is not as certain as might seem because the exit Mach number might actually exceed Mach one. This phenomenon is the subject of the last research question of this thesis and will be discussed in more detail in Section 9.3.

The last thing necessary for plotting the process in $T - \Delta s$ diagram is the change of specific entropy Δs that can be calculated using relation

$$\Delta s = c_p \ln\left(\frac{T}{T_0}\right) - R \ln\left(\frac{p}{p_{01}}\right) = c_p \ln\left(\frac{T}{T_0}\right) - R \ln\left(\varphi\right), \tag{64}$$

where φ stands for the exit pressure ratio defined by equation (61).

As the $T - \Delta s$ diagram in Figure 47 shows also lines of constant thermodynamic efficiency, it can be seen again that the process of decreasing back pressure p_b does not take place at a constant efficiency. Besides that, the diagram shows also the lines of constant exit pressure ratio φ.

To conclude this part, the computational results and the analysis of the flow discharge (Figure 46) show that the actual aerodynamic choking in narrow channels occurs for pressure ratios significantly lower than for ideal case. However, the actual choking ratio can be easily predicted using equation (56) even from only one measurement or computation performed for choked regime. Nevertheless, if only one measurement is available, it is necessary to make sure that the regime was actually choked. This might be a considerable problem since with the increasing channel length or decreasing channel height, and thus with decreasing η, the actual choked pressure ratio might become unintuitively low compared with the value in the case of ideal flow as can be seen in Figure 46. For this reason, another measurement for slightly higher pressure ratio might serve as a control one. Then, if the relative mass flow rate stays constant, the flow is most likely choked and equation 46 might be used for estimation of actual choking pressure ratio. The analysis also revealed that the critical condition based on the differentiating of the discharge curve given by equation (7) is not applicable for non-ideal flow. Since in this case, the condition results in apparent separation of critical and sonic condition, which, however, proved to be only fictional and the governing criterion for aerodynamic choking is given by sonic condition even for non-ideal flow expressed by equation (9), provided the total pressure p_0 in this equation stands for inlet total pressure p_{01} and p for the back pressure p_b. Here it is important to note that the expression for the critical pressure ratio $\left(\frac{p}{p_0}\right)_*$ derived from the sonic condition remains valid even for non-ideal flow yielding the common formula

$$\left(\frac{p}{p_0}\right)_* = \left(\frac{2}{\gamma+1}\right)^{\frac{\gamma}{\gamma-1}}. \tag{65}$$

9.3 Flow in the Channel Exit Region

The authors of the study [14] present a hypothesis that the flow field inside the relatively long channels upstream the exit plane is affected even for the back pressure ratios significantly below the theoretical choking value represented by the sonic conditions line in Figure 45. Since this might be in contrary with the findings presented in the preceding section, which shows that the flow is indeed aerodynamically choked in terms of maximum mass flow rate for pressure ratios lower than theoretical chok-

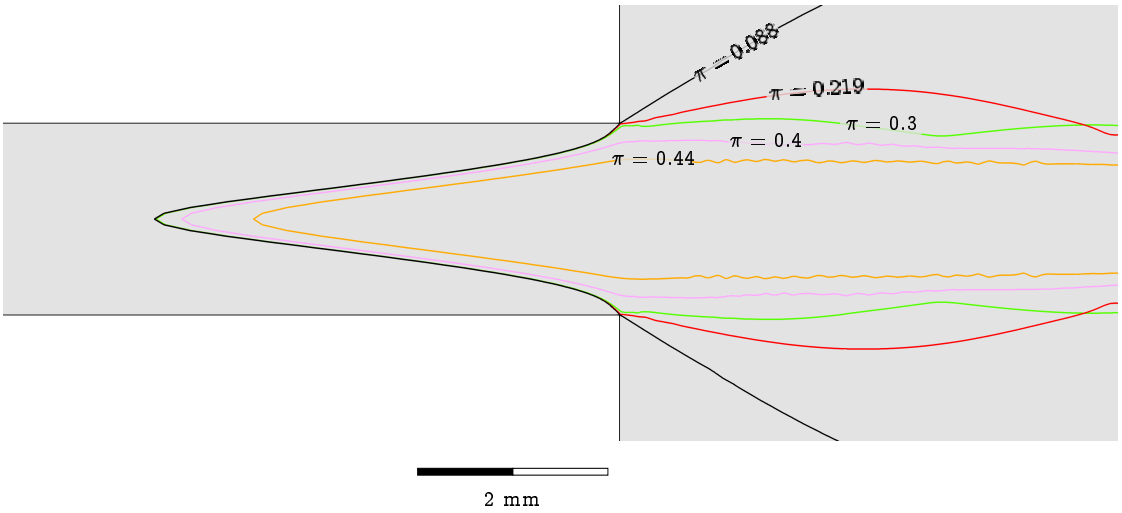

Figure 48: *Sonic lines computed using* $k-\omega$ *SST turbulence model in the exit part of the narrow channel of the height of* 2 mm *for various pressure ratios* π*.*

ing value, a further analysis of the flow field focusing in particular on the channel exit region are provided in the following paragraphs.

Figure 48 shows the sonic lines (lines of Mach number $M = 1$) computed using $k-\omega$ SST turbulence model in the exit part of the narrow channel of the height of 2 mm for various pressure ratios π. The channel height of 2 mm was chosen since most of the computations and measurements were performed for this particular case. It can be seen that as the pressure ratio decreases the flow starts first to be supersonic in small region near the exit (yellow line in Figure 48). Even in this case the supersonic region extends upstream the exit plane most notably in the channel axis. Then, with further decrease of the back pressure, the supersonic region grows up until it fills the whole exit cross-section. From the regimes that have been examined, this first happen for the case with $\pi = 0.3$. For any lower π, the supersonic region inside the channel remains the same and only the flow downstream the exit plane changes as the flow must expand to reach the low pressure in the exit plenum.

Based on this examination we can say that the flow in the exit cross-section is not yet fully supersonic even for pressure ratios below approximately 0.41, for which the flow is effectively choked in terms of maximum achievable mass flow rate as can be read from diagram in Figure 46. Though, the difference is quite small. For the examined case, the difference in the length of the supersonic region is only a few tenths of a millimetre.

Another question is the course of displacement thickness along the channel. Lio et al. claim that the boundary layer might narrow in the very vicinity of the exit plane forming divergent nozzle-like shape, which causes the acceleration of the flow

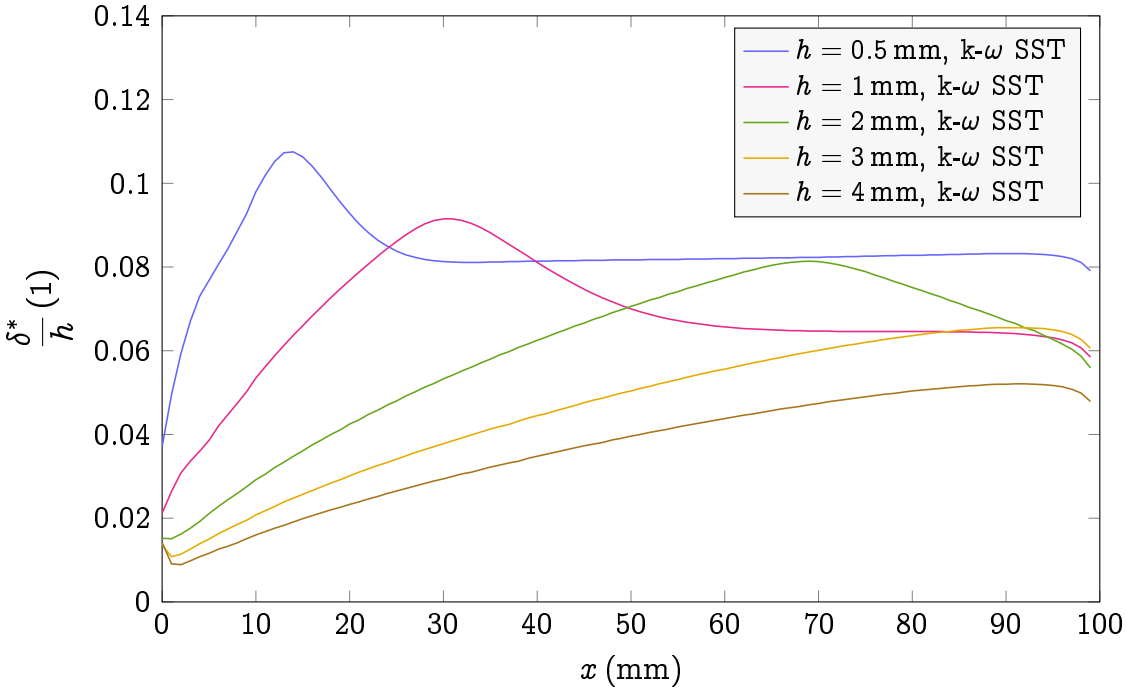

Figure 49: *Normalised displacement thickness* $\frac{\delta^*}{h}$ *along the channel for various channel heights and pressure ratio* $\pi = 0.3$ *as computed using k-ω SST turbulence model.*

beyond $M = 1$. Therefore, the displacement thickness defined as

$$\delta^*(x) = \int_0^{\frac{h}{2}} \left(1 - \frac{\rho(x,y)u(x,y)}{\rho_e u_e(x)}\right) \mathrm{d}y, \tag{66}$$

was calculated for some regimes. The h in the equation above stands for channel height and ρ_e and u_e are mid channel density and velocity respectively. The results of this analysis showing the course of displacement thickness for pressure ratio $\pi = 0.3$ and various channel heights can be seen in Figure 49. It can be best observed on the case of $h = 0.5$ mm that the displacement thickness initially grows up than reduces and keeps at approximately constant value up to very vicinity of the channel exit where another drop occurs. The first drop most likely corresponds to vanishing of the inviscid core in the flow and thus is related to flow development. Based on this, we can say that the flow in this CFD study is probably fully developed only in the case of $h = 0.5$ and $h = 1$ mm, which exhibits the plateau after initial growth and subsequent drop. Nevertheless, in all cases another drop in displacement thickness is apparent near the exit, which might cause the flow to accelerate beyond $M = 1$ as was predicted in study by Lio et al. Even though, the raw hot-film probe data discussed in qualitative analysis show some sort of signal flattening probably due to high favourable pressure gradient causing rapid flow acceleration in the location of

the last measuring plug as seen in Figure E.8, neither quantitative measurements nor computations confirmed reduction of the wall shear stress close to the channel exit, which was discussed in [8]. It is indeed necessary to mention that it was not possible to conduct the quantitative measurements for pressure ratio π lower than approximately 0.5, therefore, to fully address this issue additional measurements should be performed.

10 Conclusions

This section summarizes the conclusions drawn from the research conducted during the entire doctoral project. The main objective of this project was to explore the nature of the flow in narrow channels and investigate the influence of two different types of surface roughness particularly on the flow development and the wall shear stress distribution along the channel. This part was preceded by an extensive set of tests on the calibration facility followed by the numerical investigations, which together led to calibration of the hot-film probe representing one of the few promising methods to measure the wall shear stress in such a confined geometries. Yet, not easy to use due to many shortcomings, which had to be overcome before actual measurements. The second objective was to find out whether the flow in narrow channels experiences the separation of sonic conditions from critical conditions due to friction as theoretically predicted in study [13]. This was accomplished mostly using theoretical analyses and numerical simulations, which also provided further insight into the narrow channel flow and helped to answer the third research question that was whether the flow in the exit region of the narrow channels might experience reduction in the wall shear stress and the thinning of the boundary layer.

To answer the first research question, the results of the RANS numerical simulations using both fully turbulent and transitional turbulence models were compared to the results of a number of experimental methods. These included pneumatic measurements, optical measurements (interferometry) and hot-film anemometry. The most valuable results were obtained using the hot-film probe, which proved to be an effective method to identify the state of the flow. Further, after the calibration, the hot-film probe was also successfully used to measure the wall shear stress. The analysis of the results revealed that the flow in the examined channels was for most of the investigated channel heights transitional and not fully developed. As a result, the wall shear stress distribution was not captured satisfactorily with none of the used numerical models with the exception of the channel height $h = 0.5\,\mathrm{mm}$ with cross-flow roughness, in which case the fully turbulent model provided satisfying results. Another important finding was that the total pressure measurements in the mid channel close to channel exit provided well comparable results to the fully turbulent numerical simulations for all examined cases yielding a good estimate of the total pressure loss. However, as apparent from the qualitative hot-film probe measurements a good estimate of the total pressure loss does not guarantee reliable prediction of the distribution of the wall shear stress. It also proved that one-dimensional approach to determine the friction factor in the case of relatively short channels is barely usable and provides the friction factor values by more than

order of magnitude lower than what should correspond to actually measured wall shear stress [A6], which is in agreement with the observations referenced in [38]. Overall, the analyses of the raw hot-film probe signal and subsequent analysis of the signal skewness together with the quantitative measurements proved to be capable to provide substantial information about the nature of the flow, which is important for validation of numerical models [A3][A2][A7]. Such analyses revealed that both examined types of surface roughness shorten the transition and increase the absolute values of the wall shear stress. At the same time, the streamwise roughness apparently increases the effective channel cross-section, which is more pronounced with decreasing channel height. At this point it is important to note that the quantitative analysis itself provides only mean value of the wall shear stress at the measuring location and thus the further analyses of the raw signal should always follow to obtain an information whether the flow is developed or transitional and, in the later case, in which stage of transition it is.

The second objective was accomplished by theoretical analysis and accompanying numerical study. The analysis revealed that the actual choking occurs for non-ideal flow for lower values of the driving pressure ratio π. However, the choking takes place when the sonic pressure ratio is reached in the critical cross-section. Therefore, equation (9) can be used for determination of the actual back pressure ratio π necessary for given thermodynamic efficiency η to obtain aerodynamically choked flow. Additionally, the working formulas for mass flow rate ratio with respect to back pressure ratio and thermodynamic efficiency as a parameter were derived (52) and the resulting relations were drawn together with the results of the numerical simulations in more comprehensive form in charts in Figures 45 and 46 and in the $T - \Delta s$ diagram in Figure 47.

The numerical simulations were also used to explore the flow close to the channel exit revealing that the sonic line actually moves inwards the channel even for pressure ratios, below which the flow is aerodynamically choked. Nevertheless, this change was quite small and seems to have negligible influence on the resulting mass flow rate through the channel, therefore, the choking condition expressed by the maximum of the mass flow rate remains satisfied. The numerical computations also proved that the boundary layer is thinning close to the channel exit most likely due to large favourable pressure gradient as also referenced in study [14]. However, despite the observable influence on the hot-film probe signal, which apparently flattened indicating diminishing of the turbulent fluctuations, both quantitative measurements and computations yield increasing wall shear stress towards the channel exit. Yet, the quantitative measurements were not conducted for choked flow regime, which would require back pressure ratio lower than approximately $\pi = 0.3$ in the case of

channel height $h = 0.5\,\mathrm{mm}$, therefore, additional measurements can be recommended to explore the influence of even larger pressure gradients, which will be a subject of following research.

As a final conclusion it can be said that all three main objectives of this thesis were successfully achieved as well as a number of additional tasks which emerged during the course of this project. Furthermore, despite the complicated calibration, the hot-film anemometry turned out to be powerful method, which together with other methods already well established in our laboratory, has potential to substantially enhance the capability in investigation of the compressible viscous flow and demonstrated its potential not only for the investigation of confined geometries such as narrow channels but also for compressor and turbine blade cascades as already demonstrated during the measurements on the transonic blade profile [A4]. This is of particular importance since compressor and turbine blades still represent the most common test articles in Nový Knín laboratory.

Nomenclature

Non-dimensional Numbers

Kn	Knudsen number	1
M	Mach number	1
Re	Reynolds number	1
Re_{u_*}	Reynolds number based on the shear velocity u_*	1

Greek Symbols

α	coefficient of thermal expansion	K^{-1}
α^{eff}	effective thermal diffusivity	$\mathrm{m}^2\cdot\mathrm{s}^{-1}$
δ	boundary layer thickness	m
δ^*	displacement thickness	m
δ_{eff}	displacement of the effective centre of the pitot probe	m
ϵ	equivalent sand-grain roughness	m
ϵ	relative error of the solution (in Section 6.5)	%
γ	ratio of specific heats; intermittency	1
λ	molecular mean free path; wavelength (in Section 5.5)	m
μ	dynamic viscosity	$\mathrm{Pa}\cdot\mathrm{s}$
ν	kinematic viscosity	$\mathrm{m}^2\cdot s^{-1}$
ω	specific turbulence dissipation	s^{-1}
π	pressure ratio (ratio of the back pressure (settling chamber pressure) to inlet total pressure)	1
ρ	density	$\mathrm{kg}\cdot\mathrm{m}^{-3}$
σ	particle hard shell diameter	m
τ_w	wall shear stress	$\mathrm{N}\cdot\mathrm{m}^{-2}$
$\tau_{ij}^{\mathrm{eff.}}$	effective stress tensor including the viscous and Reynolds stress tensors	$\mathrm{N}\cdot\mathrm{m}^{-2}$
θ	momentum thickness	m
φ	exit pressure ratio (exit plane pressure to inlet total pressure)	1

General Symbols

a	fence probe calibration constant	$\mathrm{N}\cdot\mathrm{m}\cdot\mathrm{s}\cdot\mathrm{kg}^{-1}$
b	fence probe calibration constant	1
C_1	hot-film sensor calibration constant	$\mathrm{V}^2\cdot\mathrm{K}^{-1}$
C_2	hot-film sensor calibration constant	m
c_p	specific heat capacity at constant pressure	$\mathrm{J}\cdot\mathrm{kg}^{-1}\cdot\mathrm{K}^{-1}$
D	characteristic dimension	m

E	Richardson error estimator (36) and (37)	1
e	specific internal energy	$\mathrm{J \cdot kg^{-1}}$
f	friction factor	1
F_s	safety factor	1
GCI	grid convergence index (35)	%
h	channel height	m
h	specific enthalpy (in equation (32))	$\mathrm{J \cdot kg^{-1}}$
h_f	fence probe height	m
i	interference fringe number	1
K	Gladston-Dale constant	$\mathrm{m^3 \cdot kg^{-1}}$
k	thermal conductivity	$\mathrm{W \cdot m^{-1} \cdot K^{-1}}$
k	turbulent kinetic energy	$\mathrm{m^2 \cdot s^{-2}}$
k_B	Boltzmann constant	$\mathrm{J \cdot K^{-1}}$
k_L	laminar kinetic energy	$\mathrm{m^2 \cdot s^{-2}}$
L_e	entrance length	m
L_{ts}	width of the test section	m
$\dot{m}$	mass flow rate	$\mathrm{kg \cdot s^{-1}}$
N	number of grid cells	–
n	refractive index (in Section 5.5)	1
p	order of accuracy of the used method (in Section 6.5)	–
p	pressure	$\mathrm{N \cdot m^{-2}}$
R	specific gas constant	$\mathrm{J \cdot K^{-1} \cdot kg^{-1}}$
r	refinement factor (in Section 6.5)	–
r	specific refraction (in Section 5.5)	$\mathrm{m^3 \cdot kg^{-1}}$
Ra	arithmetic average roughness	μm
Rz	average maximum height of profile	μm
s	specific entropy	$\mathrm{J \cdot K^{-1} \cdot kg^{-1}}$
T	thermodynamic temperature	K
t	temperature	°C
Tu	turbulence intensity	%
u	mean flow velocity	$\mathrm{m \cdot s^{-1}}$
u_*	shear velocity, defined as $u_* = \sqrt{\frac{\tau_w}{\rho}}$	$\mathrm{m \cdot s^{-1}}$
u^+	dimensionless velocity $u^+ = \frac{u}{u_*}$	1
V	electrical voltage	V
x	length coordinate	m
y	wall distance	m
y^+	dimensionless wall-normal distance $y^+ = \frac{y u_*}{\nu}$	1

Subscripts

$*$	critical conditions
0	stagnation conditions, zero flow conditions
e	related to channel exit plane
is	isentropic
j	index of summation
N	normal conditions (as referred to in Section 5.5)
ref.	reference conditions
son.	sonic conditions ($M = 1$)

References

Author's Publications Related with the Present Thesis

A1. HÁLA, J. *Compressible Fluid Flow through Minichannel*. Prague: Master Thesis, CTU in Prague, Faculty of Mechanical Engineering, 2014.

A2. PRAUSOVÁ, H.; BUBLÍK, O.; VIMMR, J.; LUXA, M.; HÁLA, J. Clearance gap flow: Simulations by Discontinuous Galerkin Method and Experiments. *EPJ Web of Conferences*. 2015, vol. 92. Available from DOI: 10.1051/epjconf/20159202073.

A3. HÁLA, J.; LUXA, M.; PRAUSOVÁ, H.; BUBLÍK, O.; VIMMR, J. Clearance Gap Flow: Extended Pneumatic Measurements and Simulations by Discontinuous Galerkin Finite Element Method. *EPJ web of conferences*. 2016, vol. 114. Available from DOI: 10.1051/epjconf/201611402034.

A4. LUXA, M.; HÁLA, J. *Measurements on NACA 0010-64 profile*. Prague, 2018. Research report, Z-1596/18. Institute of Thermomechanics of the Czech Academy of Sciences.

A5. HÁLA, J.; LUXA, M. Numerical and Experimental Studies of the Flow Through Narrow Gap. In: *Colloquium Fluid Dynamics 2014 Proceedings*. Prague, 2014, pp. 15–16.

A6. HÁLA, J.; LUXA, M.; BUBLÍK, O.; PRAUSOVÁ, H.; VIMMR, J. Compressible Viscous Flow in Minichannel - Experiment and Numerical Studies. In: *Computational Mechanics 2014 - Book of extended abstracts*. Pilsen, 2014, pp. 39–40.

A7. PRAUSOVÁ, H.; BUBLÍK, O.; VIMMR, J.; HÁLA, J.; LUXA, M. Numerical and Experimental Investigation of Compressible Viscous Fluid Flow in Minichannels. In: *Proceedings of Computational mechanics 2019*. Pilsen, 2019, pp. 160–163.

Other References

1. REYNOLDS, O. An experimental investigation of the circumstances which determine whether the motion of water shall be direct or sinuous, and of the law of resistance in parallel channels. *Proceedings of the Royal Society of London*. 1883, vol. 35, no. 224-226, pp. 84–99. Available from DOI: 10.1098/rspl.1883.0018.

2. JONES O. C., Jr. An Improvement in the Calculation of Turbulent Friction in Rectangular Ducts. *Journal of Fluids Engineering*. 1976, vol. 98, no. 2, pp. 173–180. Available from DOI: 10.1115/1.3448250.

3. ECKHARDT, B.; SCHNEIDER., T. M.; HOF, B.; WESTERWEEL, J. Turbulence Transition in Pipe Flow. *Annual Review of Fluid Mechanics*. 2007, vol. 39, no. 1, pp. 447–468. Available from DOI: 10.1146/annurev.fluid.39.050905.110308.

4. TAYLOR, J B.; CARRANO, A L.; KANDLIKAR, S G. Characterization of the effect of surface roughness and texture on fluid flow—past, present, and future. *International Journal of Thermal Sciences*. 2006, vol. 45, no. 10, pp. 962–968. Available from DOI: https://doi.org/10.1016/j.ijthermalsci.2006.01.004.

5. AVILA, K.; MOXEY, D.; LOZAR, A. de; AVILA, M.; BARKLEY, D.; HOF, B. The Onset of Turbulence in Pipe Flow. *Science*. 2011, vol. 333, no. 6039, pp. 192–196. Available from DOI: 10.1126/science.1203223.

6. DIXIT, T.; GHOSH, I. Review of micro- and mini-channel heat sinks and heat exchangers for single phase fluids. *Renewable and Sustainable Energy Reviews*. 2015, vol. 41, pp. 1298–1311. Available from DOI: https://doi.org/10.1016/j.rser.2014.09.024.

7. KANDLIKAR, S. G.; GARIMELLA, S.; LI, D.; COLIN, S.; KING, M. R. *Heat Transfer and Fluid Flow in Minichannels and Microchannels*. Elsevier Ltd, 2006.

8. LUXA, M.; DVOŘÁK, R.; ŠIMURDA, D.; VIMMR, J. Gas Flow in Constant Area Minichannels. In: *10th International Symposium on Experimental and Computational Aerothermodynamics of Internal Flows - ISAIF 10*. Vrije Universiteit Brussel, 2011, pp. 52–58.

9. VIMMR, J.; KLÁŠTERKA, H.; HAJŽMAN, M.; LUXA, M.; DVOŘÁK, R. Mathematical modelling and experimental investigation of gas flow in minichannels and microchannels. *Journal of Thermal Science*. 2010, vol. 19, pp. 289–294. Available from DOI: 10.1007/s11630-010-0385-x.

10. SHAPIRO, A. H. *The Dynamics and Thermodynamics of Compressible Fluid Flow. Vol. I*. The Ronald Press Company, 1953.

11. MLYNAŘÍKOVÁ, H. *Mathematical modeling of turbulent flows*. Pilsen: Master Thesis, University of West Bohemia, Faculty of Applied Sciences, 2012. (in Czech).

12. PRAUSOVÁ, H. *Modelling of turbulent flows using RANS and implicit LES with application of discontinuous Galerkin method*. Pilsen: Ph.D. Thesis, University of West Bohemia, Faculty of Applied Sciences, 2019. (in Czech).

13. HYHLÍK, T.; J.MACEK; P.ŠAFAŘÍK. A Contribution to Solution of Aerodynamic Choking in Flow Parts of Machines at Consideration of Thermodynamic Efficiency. In: *Colloquium FLUID DYNAMICS 2001*. Prague, 2001, pp. 23–26. (in Czech).

14. LIJO, V.; KIM, H. D.; SETOGUCHI, T. Analyses of Choked Viscous Flows Through a Constant Area Ducts. In: *Proceedings of the Institution of Mechanical Engineers*. 2010, vol. 224, G11.

15. MACMILLAN, F. A. *Experiments on Pitot-tubes in Shear Flow*. London, 1957. Technical Report, No. 3028. Aeronautical Research Council, Reports and Memoranda.

16. *NetScanner™System 9116*. Hampton, VA, 2012. Available from `http://www.meas-spec.com/register.aspx?id=9235#`.

17. KREHL, P. O. *History of Shock Waves, Explosions and Impact: A Chronological and Biographical Reference*. Berlin: Springer, 2008.

18. MOKRÝ, M. *Aerodynamic Measurements Using Mach-Zehnder Interferometer*. Prague, 1967. Research Report, Z-239/67. Institute of Thermomechnics AS CR, v.v.i. (in Czech).

19. KOHLRAUSH, F. *Praktische Physik. Bd. 1, 2*. Leipzig: Teubner-Verlag, 1955.

20. GLASS, J. J.; GORDON, J. *Handbook of Supersonic Aerodynamics, Shock Tubes*. Washington, D. C.: Navord Rep. 1488, 1959.

21. PŘÍHODA, J. *Methods of Wall-Shear Stress Measurements*. Prague, 1974. Research Report, Z-443/74. Institute of Thermomechnics AS CR, v.v.i. (in Czech).

22. LIEPMNANN, H. W.; SKINNER, G. T. *Shearing Stress Measurements by Use of a Heated Element: Technical note 3268*. 1954. Technical note 3268. California Institute of Technology.

23. TROPEA, C.; YARIN, A.; FOSS, J. F. (eds.). *Handbook of Experimental Fluid Mechanics*. Berlin Heidelberg: Springer-Verlag, 2007.

24. JONÁŠ, P.; PLAČEK, V. *Study on the wall shear stress measuring techniqus*. Prague, 1978. Research Report, T-220/78. Institute of Thermomechnics AS CR, v.v.i. (in Czech).

25. *AN-1003 Hot Wire & Film Anemometry System User's Manual*. Ramat-Gan, Israel, [n.d.].

26. AHARONI, A. *How to Adjust the Frequency Response of a CT Anemometer*. Ramat-Gan, Israel, [n.d.]. Available from `https://www.lab-systems.com/products/flow-mea/Adjusting%20the%20frequency%20response/How%20to%20set%20the%20frequency%20response%20of%20a%20CT%20anemometer.pdf`.

27. HODSON, H. P.; HUNTSMAN, I. I.; STEELE, A. B. An Investigation of Boundary Layer Development in a Multistage LP Turbine. In: *Proceedings of ASME Turbo Expo 1993: Power for Land, Sea and Air*. Cincinatti, Ohio, 1993. No. 93-GT-310.

28. TIEDEMANN, M.; KOST, F. Unsteady Boundary Layer Transition on a High Pressure Turbine Rotor Blade. In: *Proceedings of ASME Turbo Expo 1993: Power for Land, Sea and Air*. Indianapolis, Indiana, 1999. No. 99-GT-194.

29. FITZGERALD, J. E.; NIVEN, A. J.; DAVIES, M. R. D. Turbine Blade Aerodynamic Wall Shear Stress Measurements and Predictions. In: *Proceedings of ASME Turbo Expo 1998: Power for Land, Sea and Air*. Stockholm, Sweden, 1998. No. 98-GT-562. Available from DOI: 10.1115/98-GT-562.

30. GUIDES IN METROLOGY, Joint Committee for. *JCGM 100:2008 Evaluation of Measurement Data - Guide to the Expression of Uncertainty in Measurement*. 2008. Tech. rep. JCGM.

31. GOMES, R.; STOTZ, S.; BLAIM, F.; NIEHUIS, R. Hot-Film Measurements on a Low Pressure Turbine Linear Cascade With Bypass Transition. *Journal of Turbomachinery*. 2015, vol. 137, p. 091007. Available from DOI: 10.1115/1.4029967.

32. MENTER, F. R. Two-Equation Eddy-Viscosity Turbulence Models for Engineering Applications. *AIAA Journal*. 1994, vol. 32, no. 8, pp. 1598–1605.

33. MEHDIZADEH, O.; TEMMERMAN, L.; TARTINVILLE, B.; HIRSCH, Ch. Applications of EARSM Turbulence Models to Internal Flows. In: *Proceedings of ASME Turbo Expo 2012*. Copenhagen, Denmark, 2012, vol. 8. No. GT2012-68886. Available from DOI: 10.1115/GT2012-68886.

34. ROACHE, P. J. Quantification of uncertainty in computational fluid dynamics. *Annual Review of Fluid Mechanics*. 1997, vol. 29, no. 1, pp. 123–160. Available from DOI: 10.1146/annurev.fluid.29.1.123.

35. ROACHE, P. J. Perspective: A Method for Uniform Reporting of Grid Refinement Studies. *Journal of Fluids Engineering*. 1994, vol. 116, no. 3, pp. 405–413. Available from DOI: 10.1115/1.2910291.

36. THÜNKER, R.; NITSCHE, W.; SWOBODA, M. Hot-wire, hot-film and surface hot-film applications in strongly temperature loaded flows. In: *Proceedings of ICIASF 89*. Göttingen, Germany, 1989, pp. 434–442. Available from DOI: 10.1109/ICIASF.1989.77698.

37. SCHETZ, J. A.; FUCHS, A. E. *Handbook of Fluid Dynamics and Fluid Machinery*. New York: John Willey & Sons, Inc., 1996.

38. SHAPIRO, A. H. *The Dynamics and Thermodynamics of Compressible Fluid Flow. Vol. II*. The Ronald Press Company, 1954.

Appendices

A Drawing of the Narrow Channel Walls

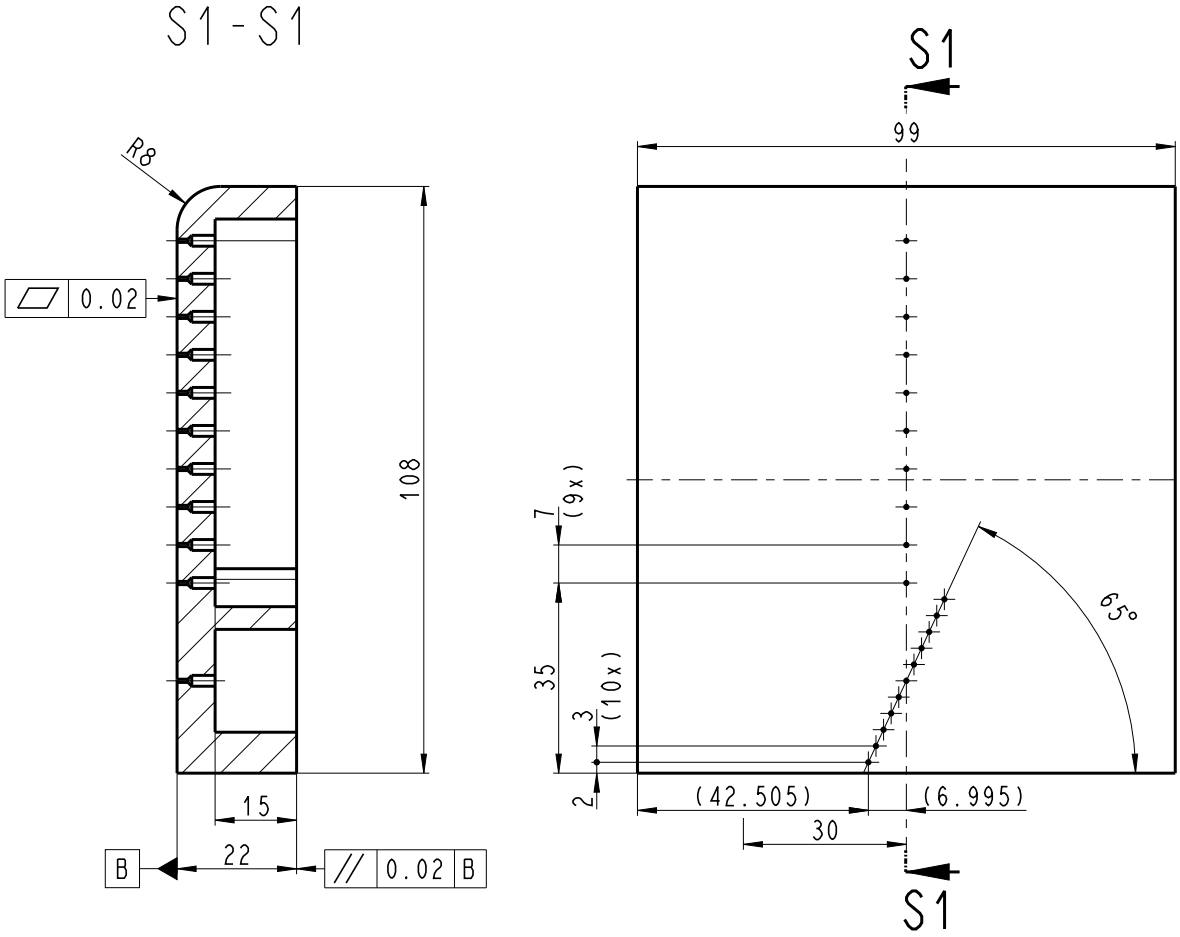

Figure A.50: *Drawing of the narrow channel wall with the layout of the static pressure tapping.*

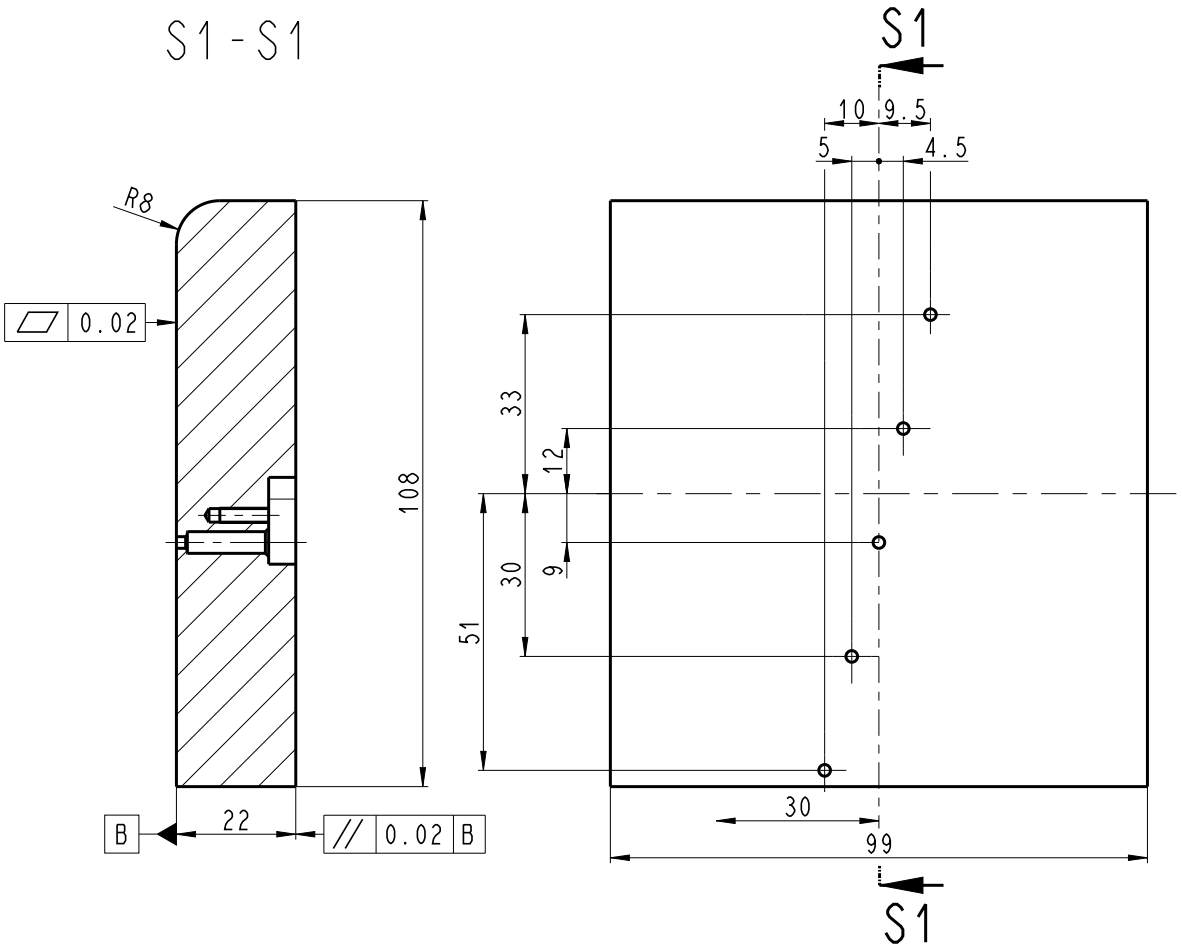

Figure A.51: *Drawing of the narrow channel wall with the layout of the measuring bores for the hot-film probe.*

B Drawing of the Calibration Channel Assembly

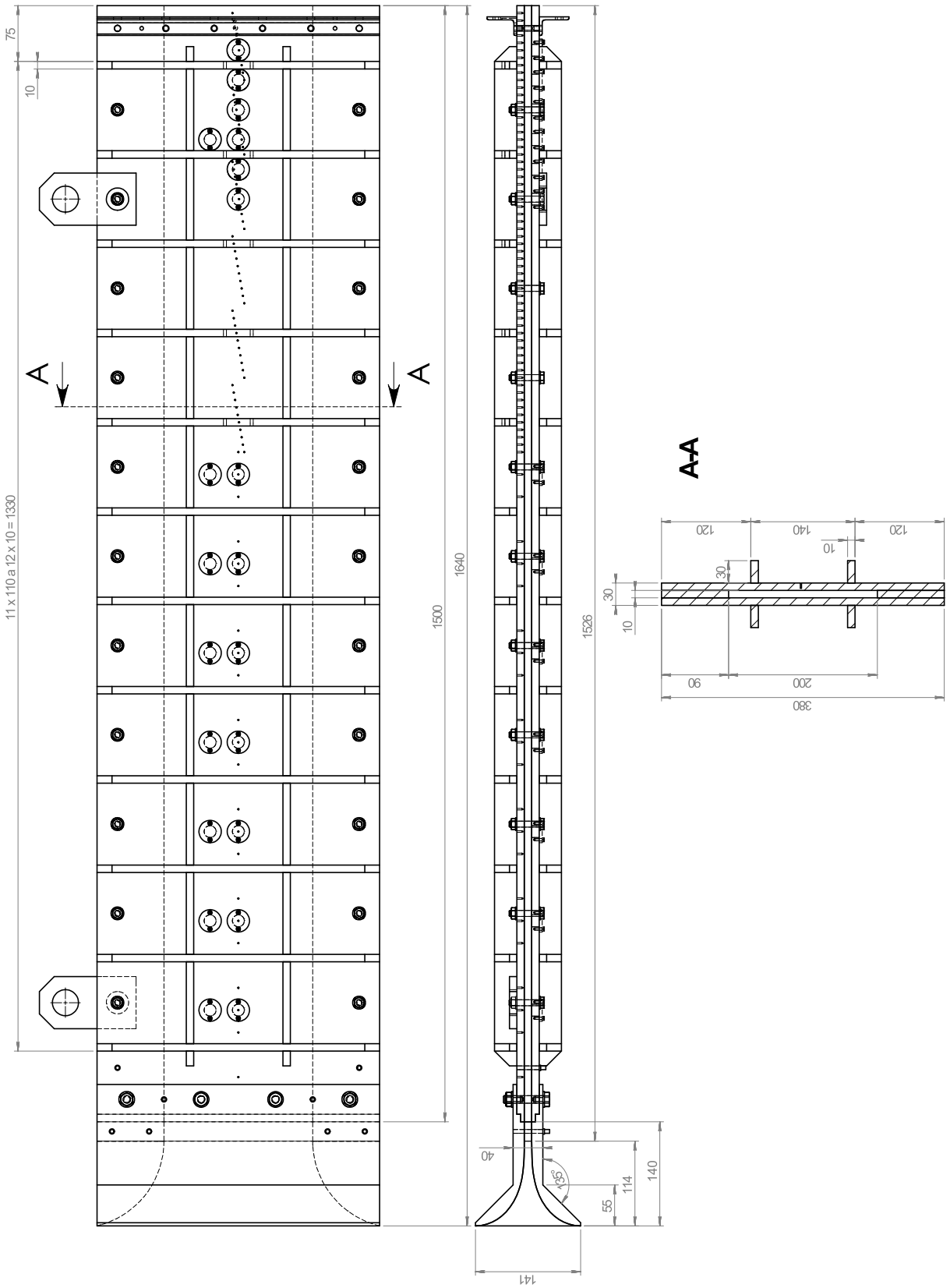

Figure B.52: Drawing of the calibration channel assembly with its main dimensions.

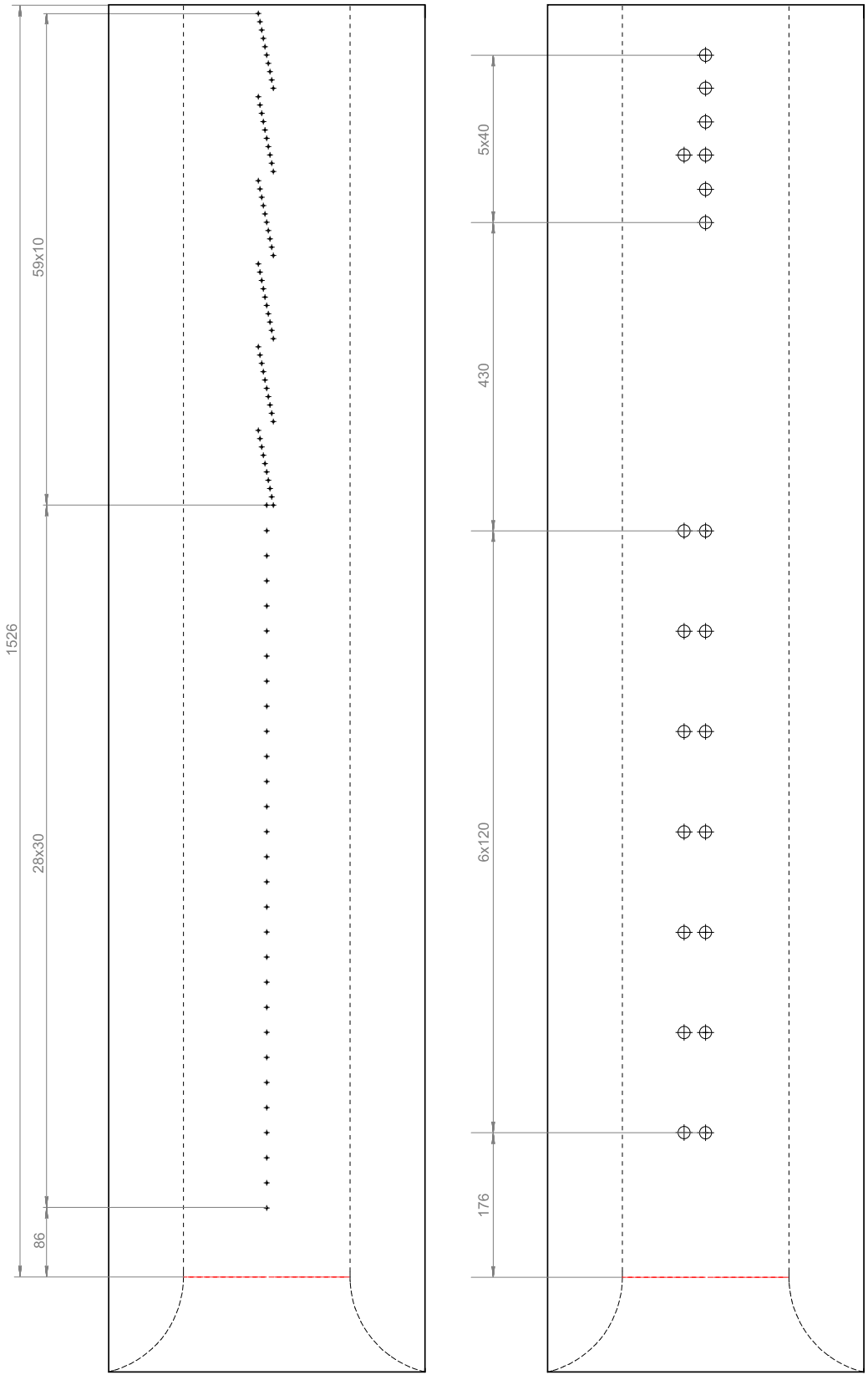

Figure B.53: Scheme of the calibration channel with the locations of the static pressure tapping (upper) and measuring plugs (bottom).

C Measured Static Pressure Distributions

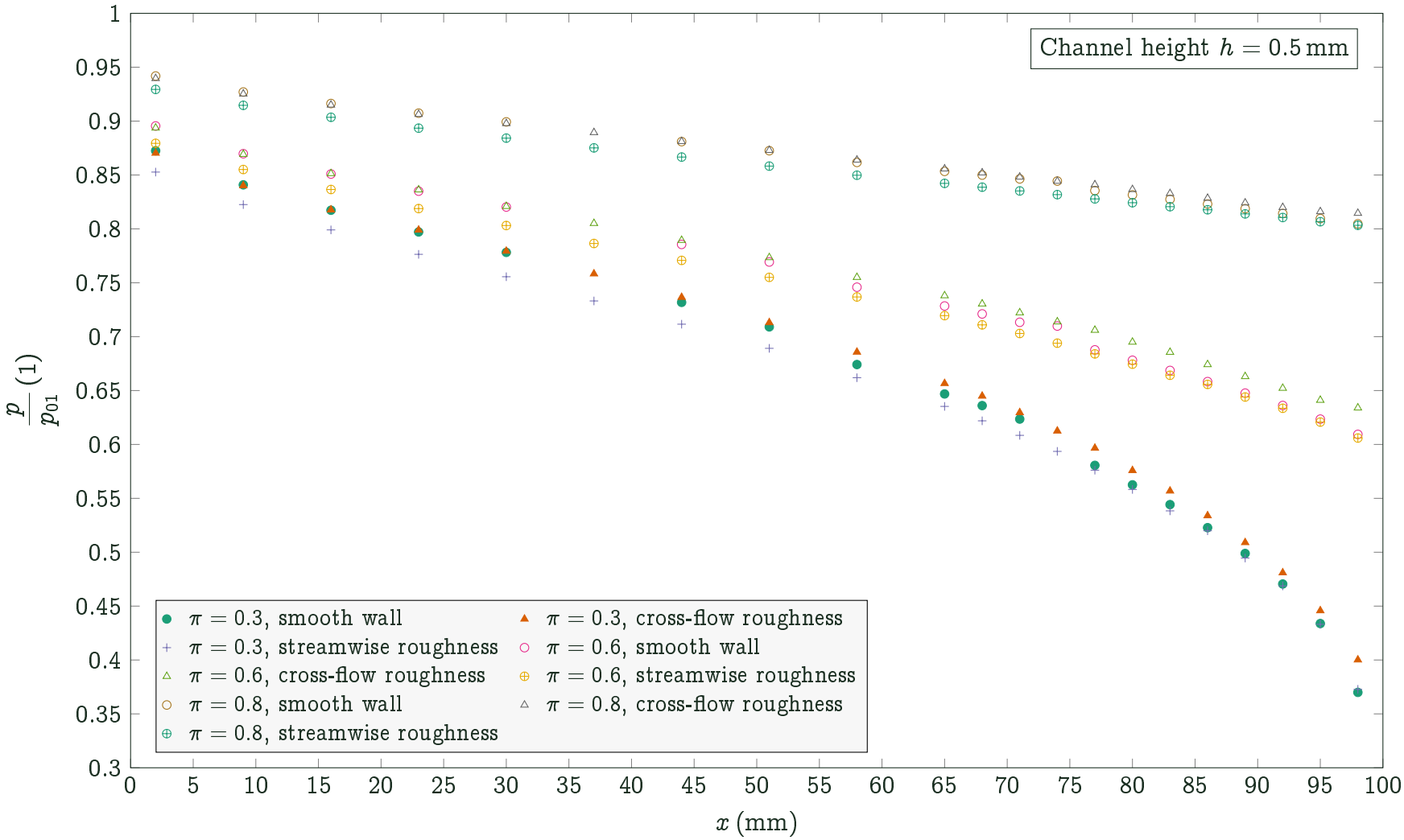

Figure C.54: *Distributions of the normalized static pressure* $\frac{p}{p_{01}}$ *along the channel length* x *for the channel of the height* $h = 0.5\,\mathrm{mm}$*, pressure ratios* $\pi = 0.3$*,* 0.6 *and* 0.8*. Comparison of measurements for different wall roughness.*

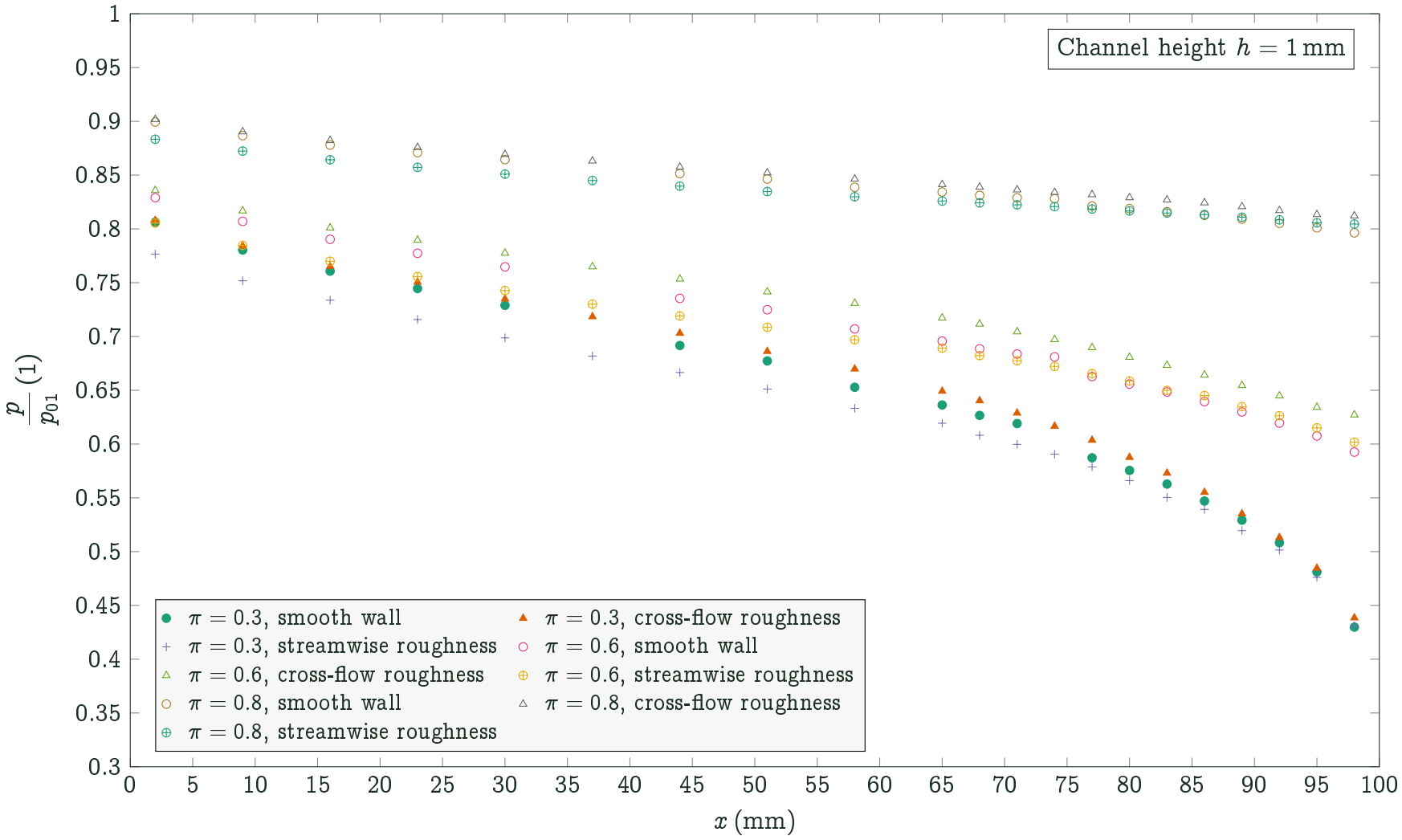

Figure C.55: *Distributions of the normalized static pressure* $\frac{p}{p_{01}}$ *along the channel length* x *for the channel of the height* $h = 1\,\text{mm}$*, pressure ratios* $\pi = 0.3,\ 0.6$ *and* 0.8*. Comparison of measurements for different wall roughness.*

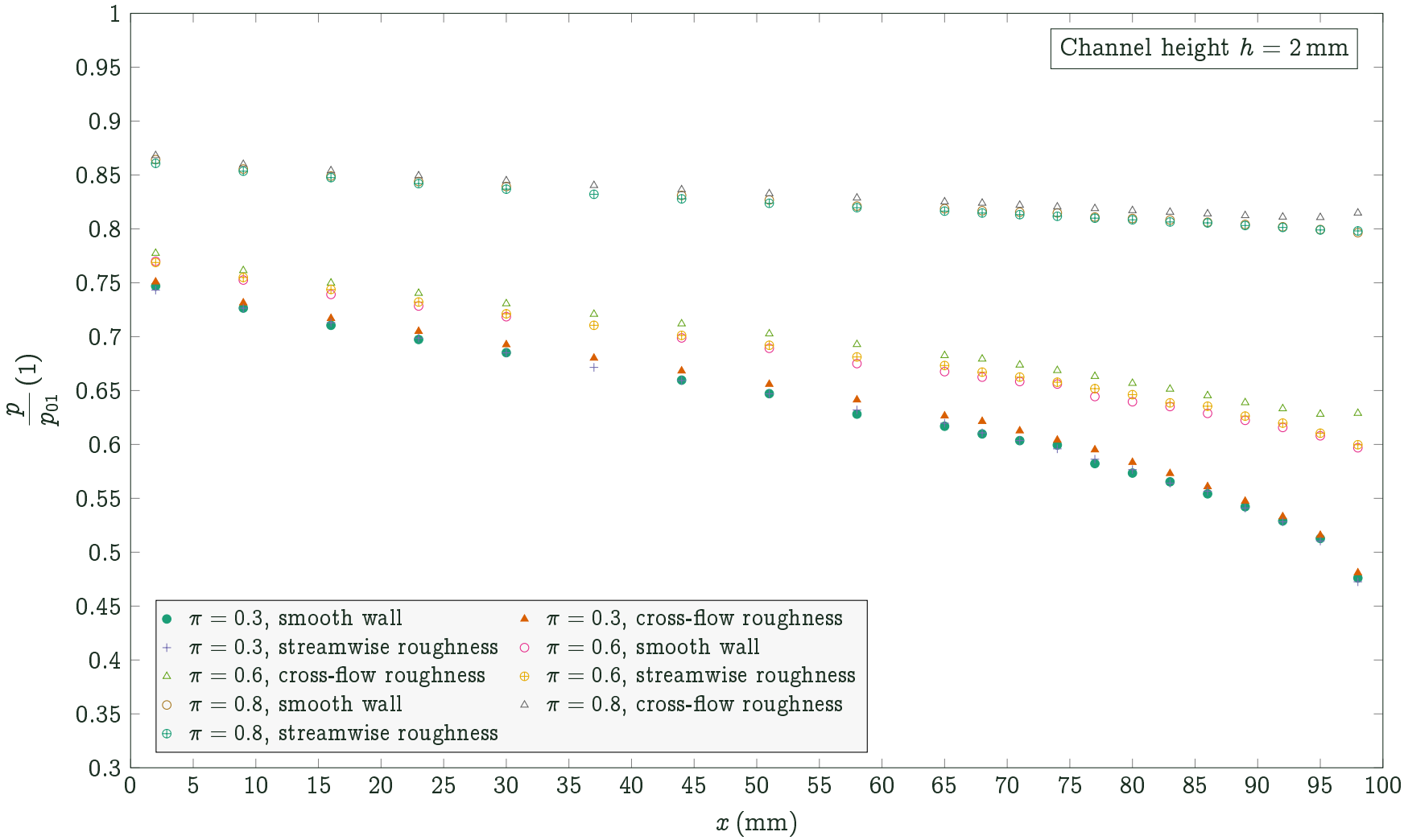

Figure C.56: *Distributions of the normalized static pressure* $\frac{p}{p_{01}}$ *along the channel length* x *for the channel of the height* $h = 2\,\text{mm}$*, pressure ratios* $\pi = 0.3,\ 0.6$ *and* 0.8*. Comparison of measurements for different wall roughness.*

D Interferograms

(a) $\pi = 1$ *(without flow), smooth walls*

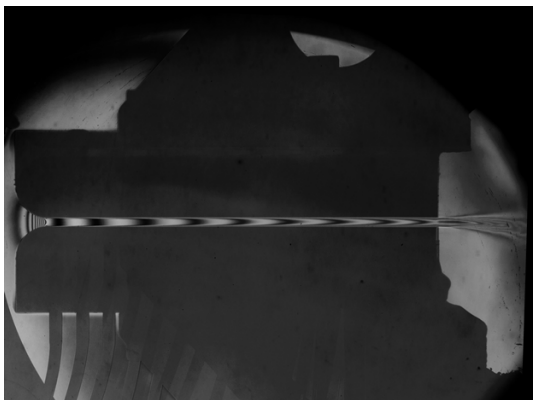

(b) $\pi = 0.61$, *smooth walls*

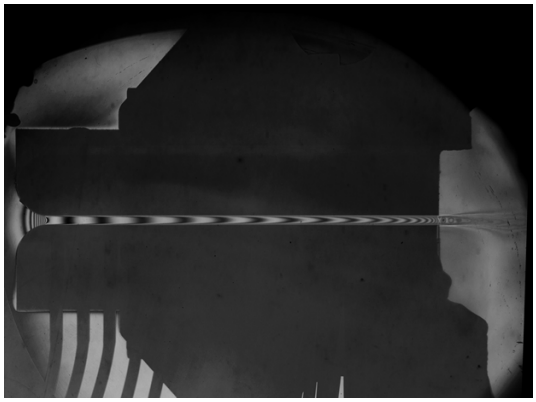

(c) $\pi = 0.44$, *smooth walls*

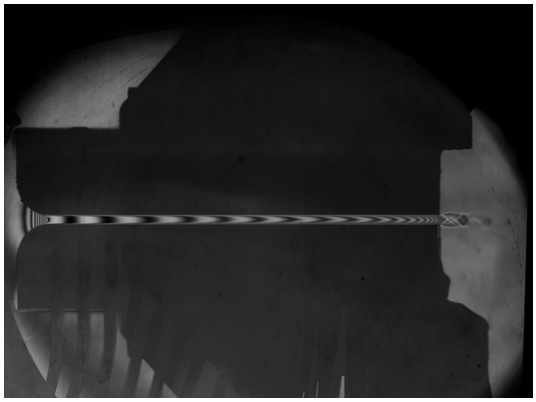

(d) $\pi = 0.22$, *smooth walls*

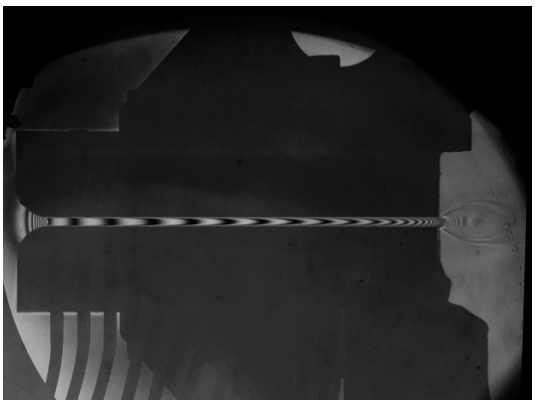

(e) $\pi = 0.088$, *smooth walls*

Figure D.1: *Interferograms of the flow field in narrow channel for smooth channel walls and various pressure ratios* π.

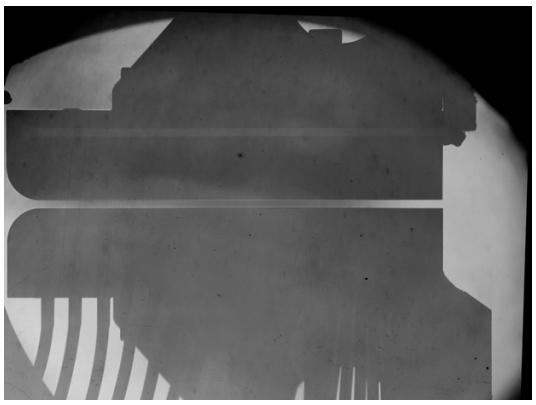

(a) $\pi = 1$ *(without flow), cross-flow roughness*

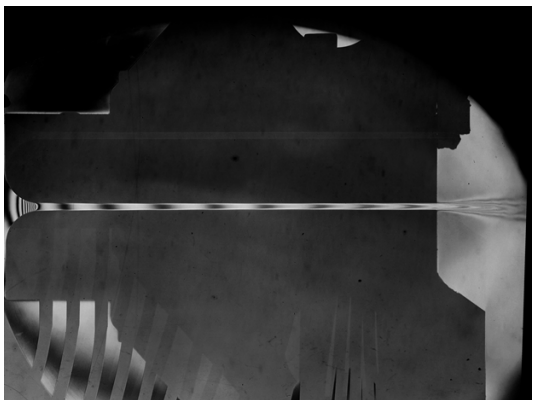

(b) $\pi = 0.61$, *cross-flow roughness*

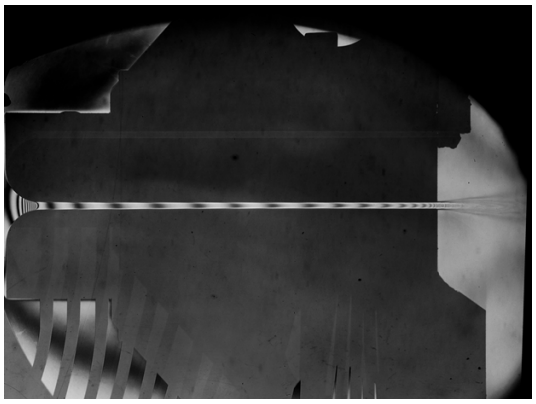

(c) $\pi = 0.44$, *cross-flow roughness*

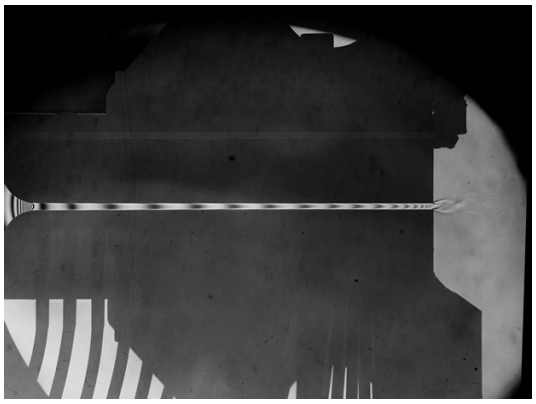

(d) $\pi = 0.22$, *cross-flow roughness*

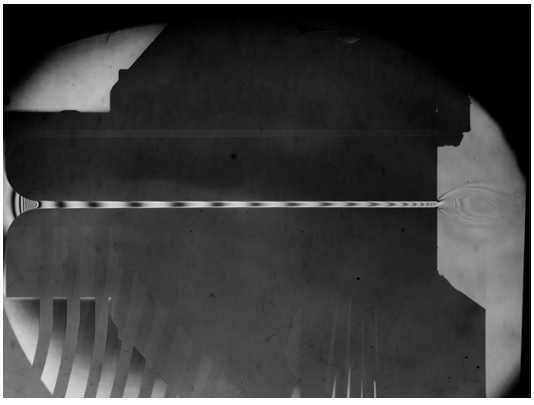

(e) $\pi = 0.088$, *cross-flow roughness*

Figure D.2: *Interferograms of the flow field in narrow channel for channel walls with the cross-flow grooves and various pressure ratios* π.

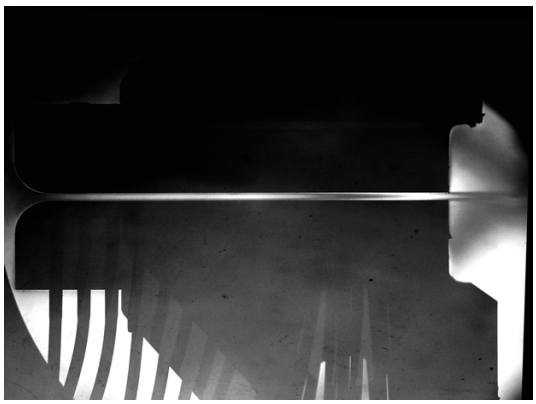

(a) $\pi = 1$ *(without flow), streamwise roughness*

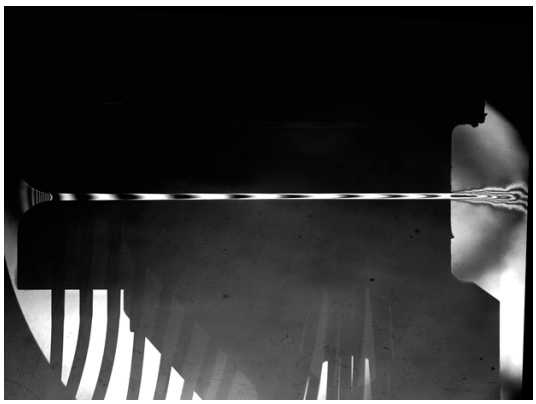

(b) $\pi = 0.61$, *streamwise roughness*

(c) $\pi = 0.44$, *streamwise roughness*

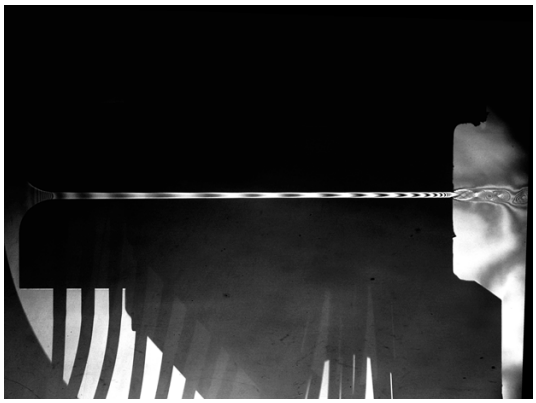

(d) $\pi = 0.22$, *streamwise roughness*

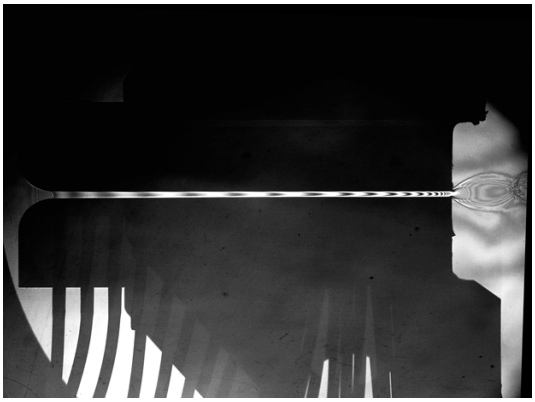

(e) $\pi = 0.088$, *streamwise roughness*

Figure D.3: *Interferograms of the flow field in narrow channel for channel walls with the streamwise grooves and various pressure ratios* π.

E Hot Film Probe Signal Data

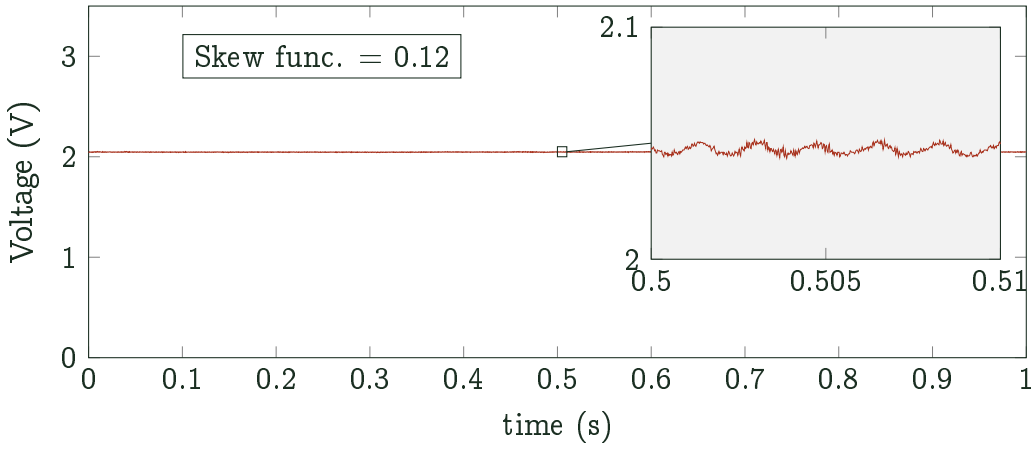

(a)

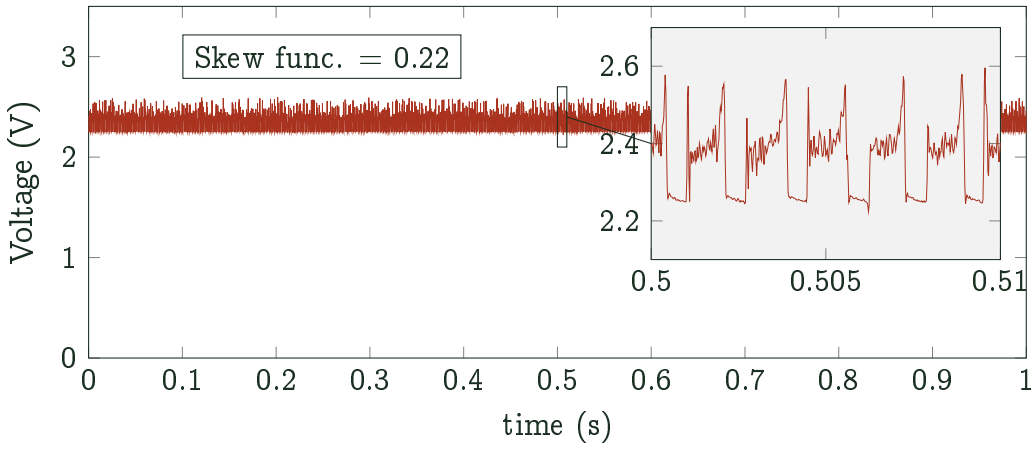

(b)

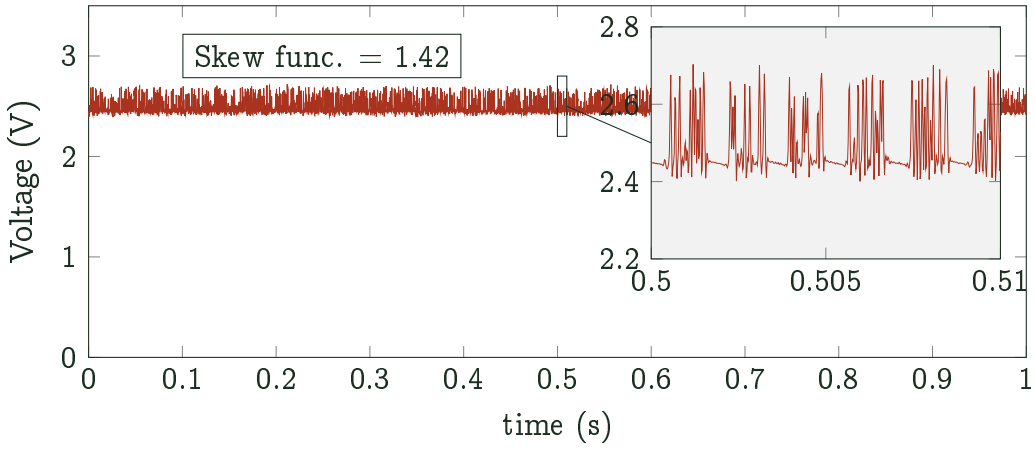

(c)

Figure E.4: *Hot-film probe signal measured in plug 1 (a), 3 (b) and 5 (c) in the channel of the height* $h = 0.5\,\mathrm{mm}$*, cross-flow roughness and* $\pi = 0.3$*.*

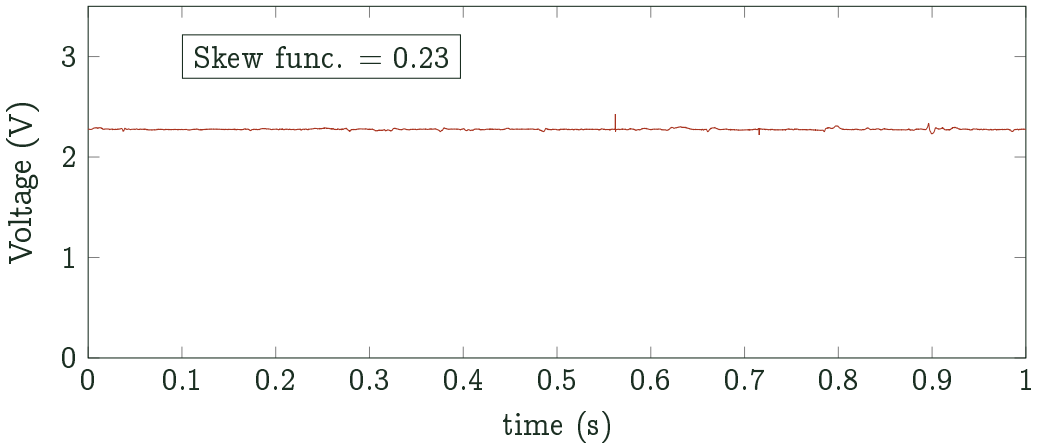

(a)

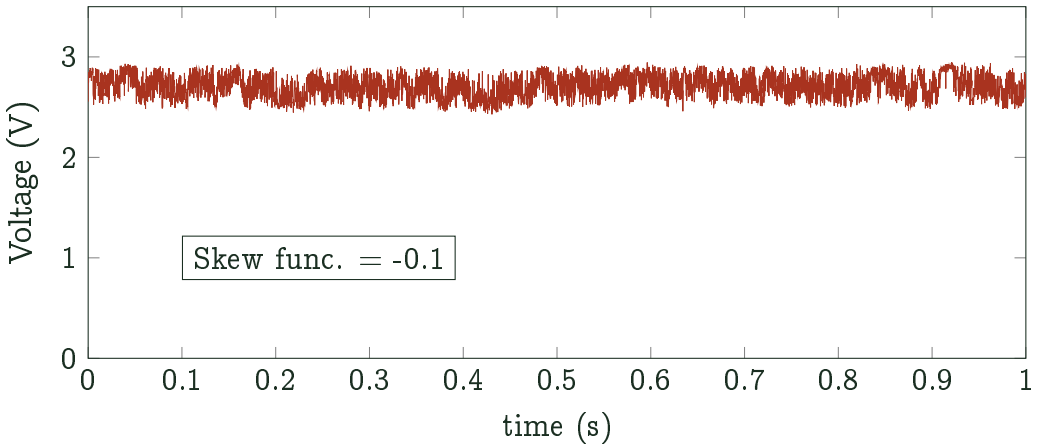

(b)

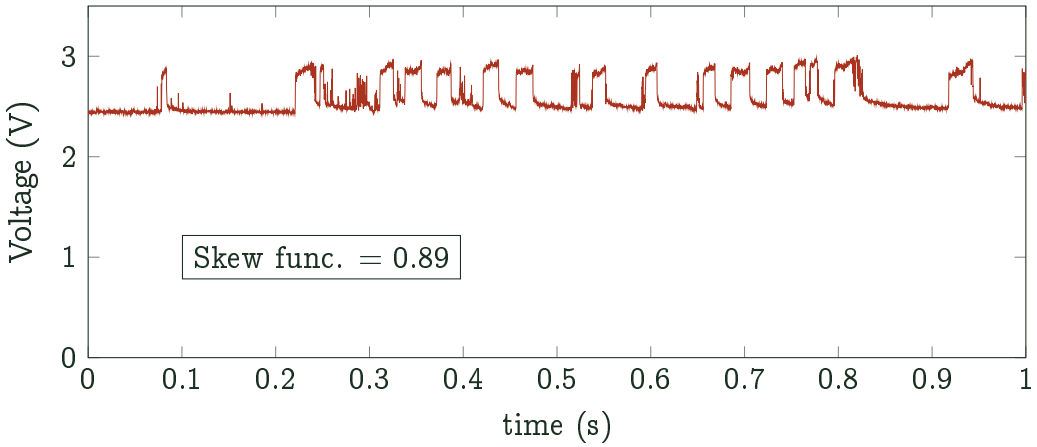

(c)

Figure E.5: *Hot-film probe signal measured in plug 1 (a), 3 (b) and 5 (c) in the channel of the height* $h = 1\,\mathrm{mm}$*, cross-flow roughness and* $\pi = 0.3$*.*

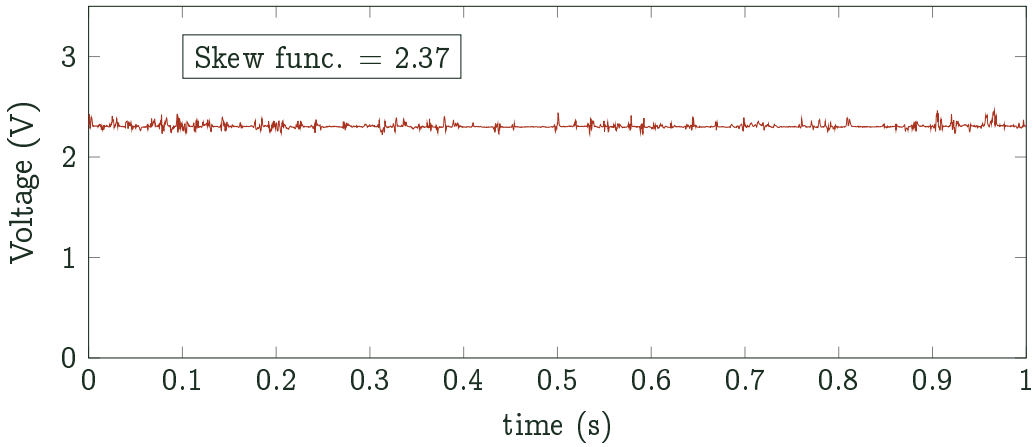

(a)

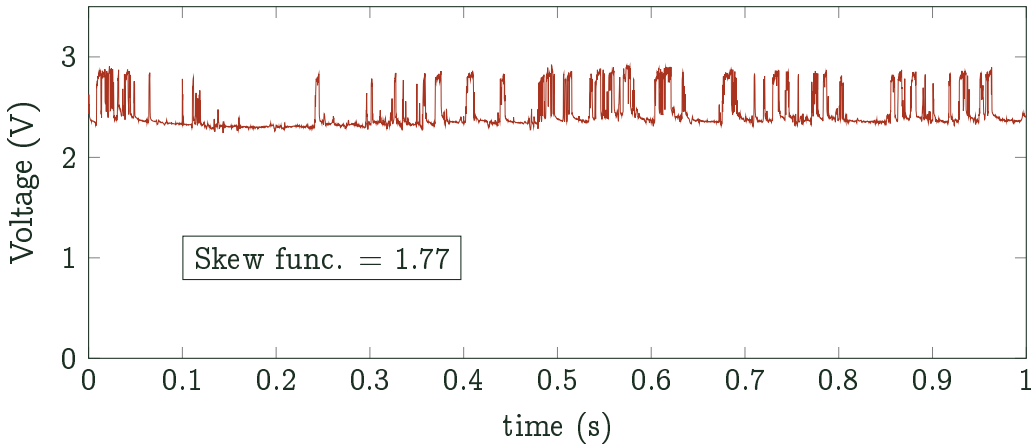

(b)

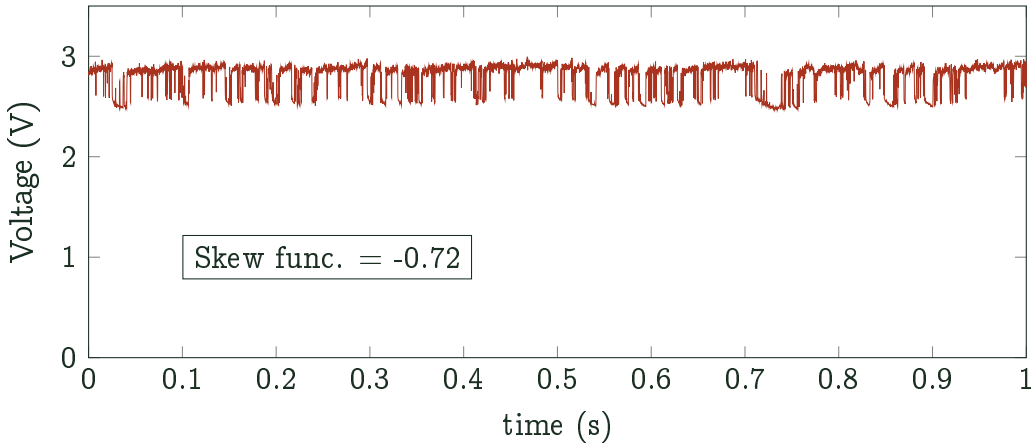

(c)

Figure E.6: *Hot-film probe signal measured in plug 1 (a), 3 (b) and 5 (c) in the channel of the height* $h = 2\,\mathrm{mm}$*, cross-flow roughness and* $\pi = 0.3$*.*

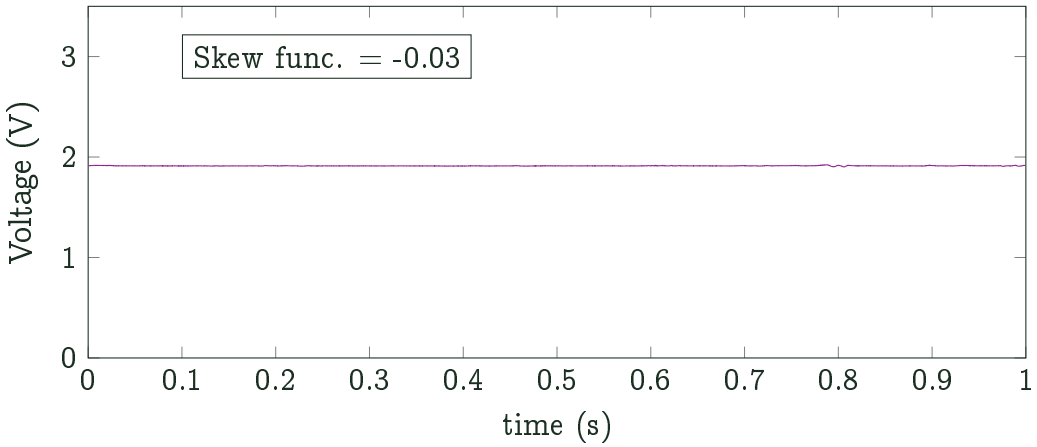

(a)

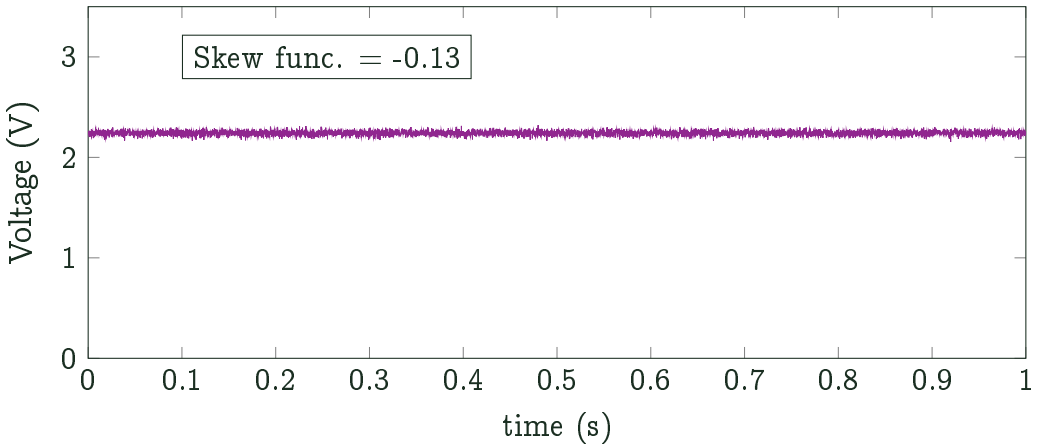

(b)

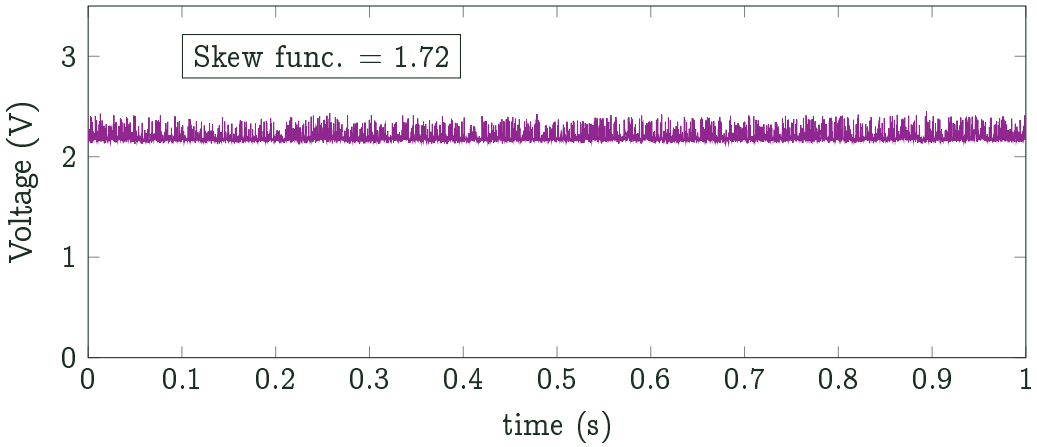

(c)

Figure E.7: *Hot-film probe signal measured in plug 1 (a), 3 (b) and 5 (c) in the channel of the height* $h = 0.5\,\mathrm{mm}$, *streamwise roughness and* $\pi = 0.3$.

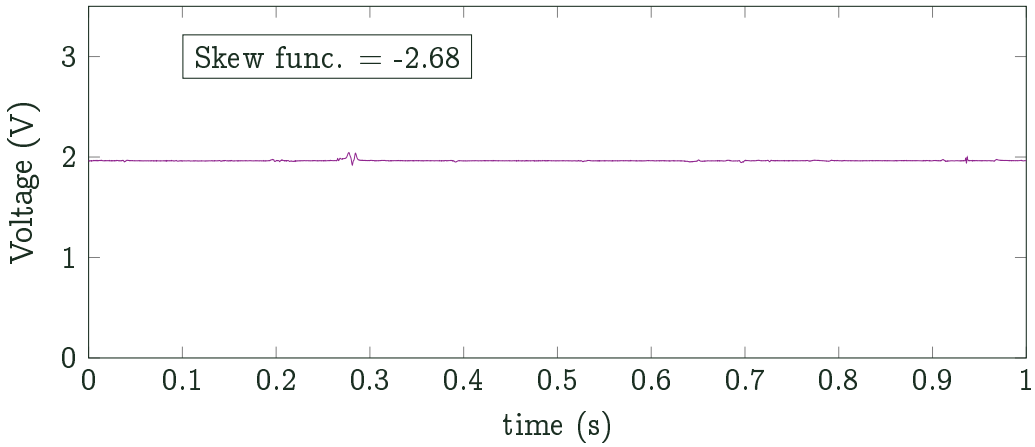

(a)

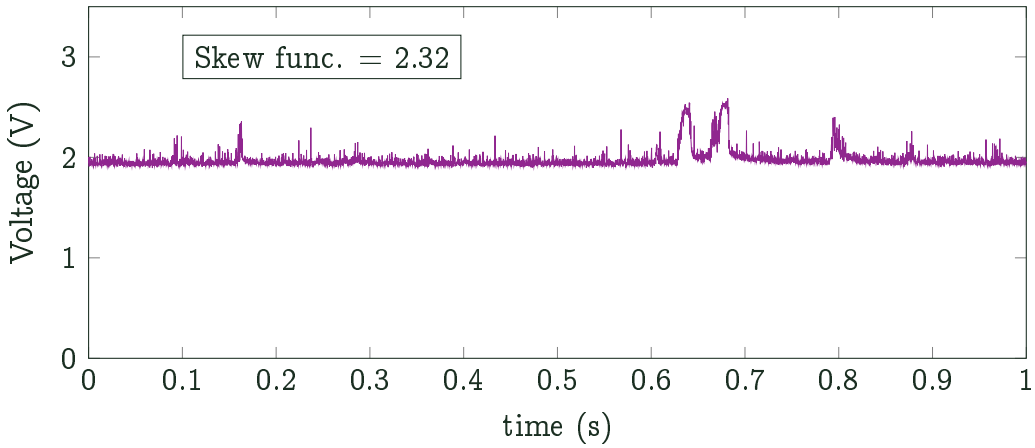

(b)

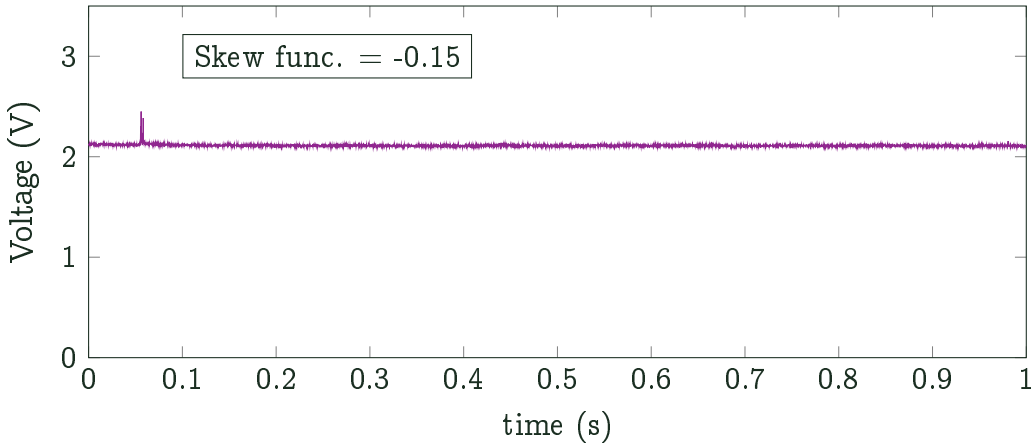

(c)

Figure E.8: *Hot-film probe signal measured in plug 1 (a), 3 (b) and 5 (c) in the channel of the height* $h = 1\,\mathrm{mm}$*, streamwise roughness and* $\pi = 0.3$*.*

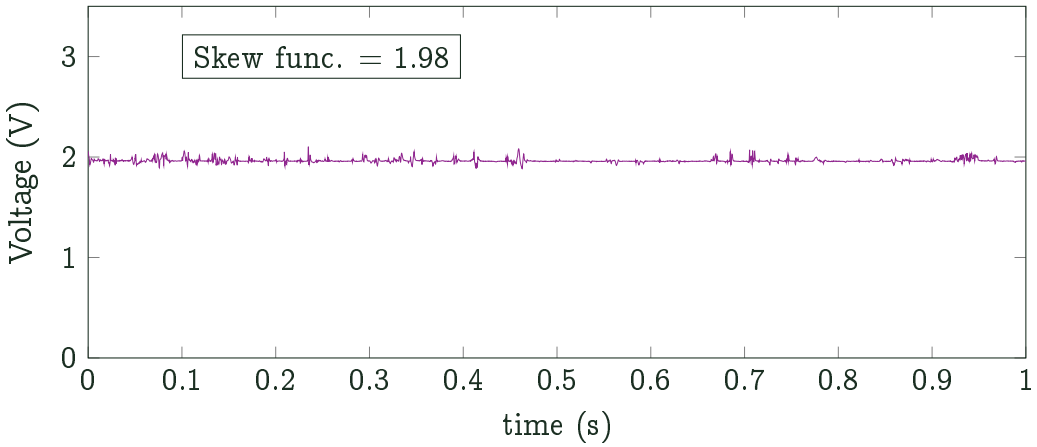

(a)

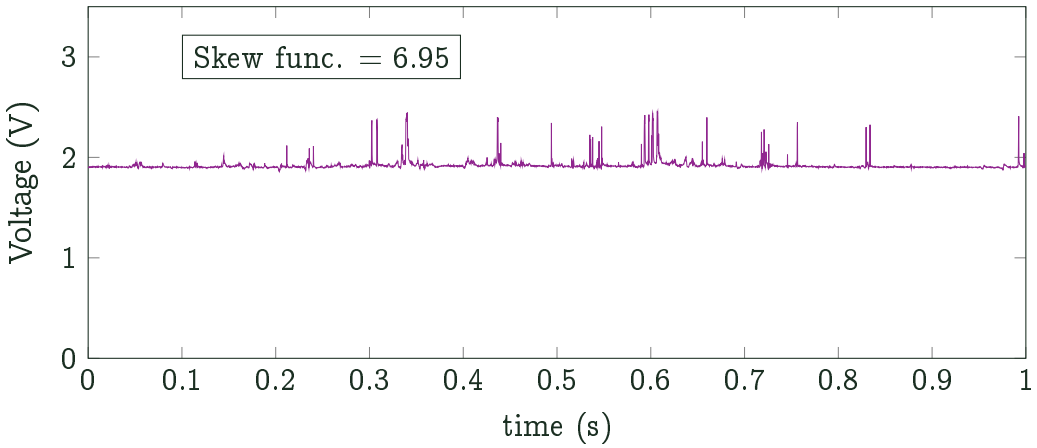

(b)

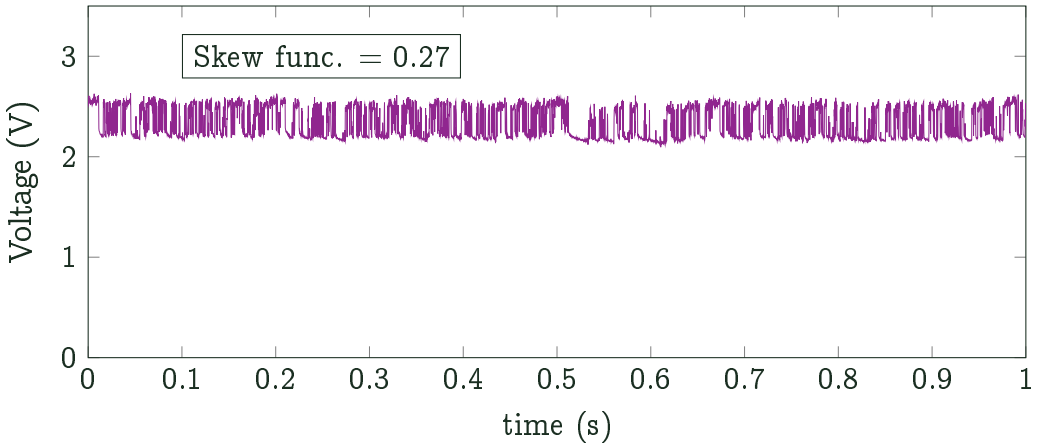

(c)

Figure E.9: *Hot-film probe signal measured in plug 1 (a), 3 (b) and 5 (c) in the channel of the height* $h = 2\,\mathrm{mm}$*, streamwise roughness and* $\pi = 0.3$*.*

F Complete List of the Author's Publications

In Impact Journals

- ŠIMURDA, D.; FÜRST, J.; HÁLA, J.; LUXA, M.; BOBČÍK, M.; NOVÁK, O.; SYNÁČ, J. Near-Wall Flow in the Blade Cascades Representing Last Rotor Root Sections of Large Output Steam Turbines. *Journal of Thermal Science*. 2020. Available from DOI: 10.1007/s11630-020-1246-x.
- HÁLA, J.; LUXA, M.; ŠIMURDA, D.; BOBČÍK, M.; NOVÁK, O.; RUDAS, B.; SYNÁČ, J. Optimization of Root Section for Ultra-long Steam Turbine Rotor Blade. *Journal of Thermal Science*. 2018, vol. 27, no. 2, pp. 95–102. Available from DOI: 10.1007/s11630-018-0989-0.
- RADNIC, T.; HÁLA, J.; LUXA, M.; ŠIMURDA, D.; FÜRST, J.; HASNEDL, D.; KELLNER, J. Aerodynamic Effects of Tie-Boss in Extremely Long Turbine Blades. *Journal of Engineering for Gas Turbines and Power*. 2018, vol. 140, no. 11, p. 112604. Available from DOI: 10.1115/1.4040093.

In Indexed Journals

- VIMMR, J.; BUBLÍK, O.; PRAUSOVÁ, H.; HÁLA, J.; PEŠEK, L. Numerical Simulation of Fluid Flow Through Simplified Blade Cascade with Prescribed Harmonic Motion Using Discontinuous Galerkin Method. *EPJ Web of Conferences*. 2018, vol. 180, p. 2117. Available from DOI: https://doi.org/10.1051/epjconf/201818002117.
- HÁLA, J.; LUXA, M.; PRAUSOVÁ, H.; BUBLÍK, O.; VIMMR, J. Clearance Gap Flow: Extended Pneumatic Measurements and Simulations by Discontinuous Galerkin Finite Element Method. *EPJ web of conferences*. 2016, vol. 114. Available from DOI: 10.1051/epjconf/201611402034.
- PRAUSOVÁ, H.; BUBLÍK, O.; VIMMR, J.; LUXA, M.; HÁLA, J. Clearance gap flow: Simulations by Discontinuous Galerkin Method and Experiments. *EPJ Web of Conferences*. 2015, vol. 92. Available from DOI: 10.1051/epjconf/20159202073.

Other Journals & Conference Proceedings

- PRAUSOVÁ, H.; BUBLÍK, O.; VIMMR, J.; HÁLA, J.; LUXA, M. Numerical and Experimental Investigation of Compressible Viscous Fluid Flow in Minichannels. In: *Proceedings of Computational mechanics 2019*. Pilsen, 2019, pp. 160–163.

- HÁLA, J.; LUXA, M.; ŠIMURDA, D.; BOBČÍK, M.; NOVÁK, O.; RUDAS, B.; SYNÁČ, J. Optimization of Root Section for Ultra-long Steam Turbine Rotor Blade. In: *Proceedings of the 13th International Symposium on Experimental Computational Aerothermodynamics of Internal Flows*. Okinawa, 2017. No. ISAIF13-S-0049.
- PEŠEK, L.; HÁLA, J.; ŠULC, P.; CHLÁDEK, Š.; BULA, V.; URUBA, V.; CIBULKA, J. Design of Low-Subsonic Blade Cascade Model for Aero-Structural Dynamic Testing. In: KOZIEŇ, M.; PEŠEK, L.; ZOLOTAREV, I. (eds.). *DYMAMESI 2017*. Prague: Institute of Thermomechanics of the Czech Academy of Sciences, 2017, pp. 87–94.
- RADNIC, T.; FÜRST, J.; HASNEDL, D.; HÁLA, J.; KELLNER, J.; LUXA, M.; ŠIMURDA, D. Aerodynamic Effects of Tie-boss in Extremely Long Turbine Blades. In: *Proceedings of the 13th International Symposium on Experimental Computational Aerothermodynamics of Internal Flows*. Okinawa, 2017. No. ISAIF13-S-0092.
- RADNIC, T.; HÁLA, J.; LUXA, M.; ŠIMURDA, D.; HASNEDL, D.; KELLNER, J. Preliminary Experiments on Transonic Cascade with Damping Device Tie-boss. In: *Proceedings of the Application of Experimental and Numerical Methods in Fluid Mechanics and Energy 2016*. Žilina: University of Žilina, 2016, pp. 197–200.
- HÁLA, J.; LUXA, M. Numerical and Experimental Studies of the Flow Through Narrow Gap. In: *Colloquium Fluid Dynamics 2014 Proceedings*. Prague, 2014, pp. 15–16.
- HÁLA, J.; LUXA, M.; BUBLÍK, O.; PRAUSOVÁ, H.; VIMMR, J. Compressible Viscous Flow in Minichannel - Experiment and Numerical Studies. In: *Computational Mechanics 2014 - Book of extended abstracts*. Pilsen, 2014, pp. 39–40.
- HÁLA, J.; ŠAFAŘÍK, P.; LUXA, M. řešení parametrů proudu při průtoku vazké stlačitelné tekutiny minikanálem. In: *Fluid mechanics and thermodynamics - Proceedings of Students' Work in the Year 2013/2014*. Praha: Gradient, 2014, pp. 37–50.
- HÁLA, J.; ŠAFAŘÍK, P.; LUXA, M. Solution of Parameters of Compressible Viscous Fluid Flow through Minichannel. In: *Fluid mechanics and thermodynamics - Proceedings of Students' Work in the Year 2013/2014*. Prague, 2014, pp. 19–34. (in Czech).
- PRAUSOVÁ, H.; BUBLÍK, O.; VIMMR, J.; LUXA, M.; HÁLA, J. Clearance Gap Flow: Simulations by Discontinuous Galerkin Method and Experiments. In: *Experimental Fluid Mechanics 2014*. Liberec, 2014.

- HÁLA, J.; ŠAFAŘÍK, P.; HYHLÍK, T.; LUXA, M.; ŠIMURDA, D. Řešení průtoku vazké stlačitelné tekutiny minikanálem. In: *Fluid mechanics and thermodynamics - Proceedings of Students' Work in the Year 2011/2012*. Praha: Gradient, 2012, pp. 37–50.

Research Reports

- LUXA, M.; ŠIMURDA, D.; HÁLA, J. *Measurements on TR-U-9 Cascade*. Prague, 2020. Research report, Z-1610/20. Institute of Thermomechanics of the Czech Academy of Sciences.
- ŠIMURDA, D.; LUXA, M.; RADNIC, T.; HÁLA, J. *Measurements on KR-D-2 Blade Cascade*. Prague, 2019. Research report, Z-1597/19. Institute of Thermomechanics of the Czech Academy of Sciences.
- LUXA, M.; HÁLA, J. *Measurements on NACA 0010-64 profile*. Prague, 2018. Research report, Z-1596/18. Institute of Thermomechanics of the Czech Academy of Sciences.
- ŠIMURDA, D.; LUXA, M.; RADNIC, T.; HÁLA, J. *Measurements on KR-D-1 Blade Cascade*. Prague, 2018. Research report, Z-1590/18. Institute of Thermomechanics of the Czech Academy of Sciences.
- ŠIMURDA, D.; HÁLA, J.; LUXA, M. *Measurement on Valve II - Appendix*. Prague, 2017. Research report, Z-1570/17. Doosan Škoda Power Ltd.
- ŠIMURDA, D.; HÁLA, J.; LUXA, M. *Measurement on Valve IV*. Prague, 2016. Research report, Z-1550/16. Doosan Škoda Power Ltd.
- ŠIMURDA, D.; HÁLA, J.; LUXA, M. *Pneumatic Measurements on TR-P-4 Cascade*. Prague, 2016. Research report, Z-1559/16. Institute of Thermomechanics of the Czech Academy of Sciences.
- ŠIMURDA, D.; HÁLA, J.; LUXA, M. *Pneumatic Measurements on TR-U-7 Cascade*. Prague, 2016. Research report, Z-1557/16. Doosan Škoda Power Ltd.
- ŠIMURDA, D.; HÁLA, J.; LUXA, M.; RADNIC, T. *Measurement on Valve V*. Prague, 2016. Research report, Z-1562/16. Doosan Škoda Power Ltd.
- HÁLA, J.; LUXA, M.; ŠIMURDA, D. *Measurement on Valve III*. Praha, 2015. Research report, Z-1539/15. Doosan Škoda Power s.r.o.
- RADNIC, T.; LUXA, M.; ŠIMURDA, D.; HÁLA, J. *Optimization of Tie-Boss*. Prague, 2015. Research report, Z-1541/15. Institute of Thermomechanics of the Czech Academy of Sciences.